INTERACTIONS BETWEEN LIKE-CHARGE PARTICLES IN COLLOIDAL SYSTEM UNDER ELECTRIC FIELD AND A MECHANOSENSING MECHANISM CENTERED ON A-CATENIN IN CELL-CELL ADHESIONS

QIU WU

(B.Sc., UNIVERSITY OF SCIENCE AND TECHNOLOGY OF CHINA)

A THESIS SUBMITTED

FOR THE DEGREE OF DOCTOR OF PHILOSOPHY

DEPARTMENT OF PHYSICS

NATIONAL UNIVERSITY OF SINGAPORE

(2015)

DECLARATION

I hereby declare that this thesis is my original work and

it has been written by me in its entirety.

I have duly acknowledged all the sources of information

which have been used in the thesis.

This thesis has also not been submitted

for any degree in any university previously.

_____

QIU WU

21 AUG 2015

ACKNOLEDGEMENTS

Foremost, I would like to express my deepest and sincere gratitude to my supervisor, Professor Liu Xiangyang and former supervisor Dr. Liu Ruchuan, for their constant support, invaluable advices and encouragement throughout my PhD candidature. Prof. Liu Xiangyang provided me a global insight and I kept being amazed by his work altitude and passion for science. Dr. Liu Ruchuan offered me details advices and suggestions on the research works. My research work would not have been possible without both of their valuable experience and persistent guidance.

I also want to thank my collaborators- Professor Yan Jie, Professor Rene-Macr Mege, Professor Benoit Ladoux and their group members for their guidance and help. Especially I want to thank Dr. Yao Mingxi. I learned and was enjoyed during the discussion with him.

Meanwhile, I learned a lot from my colleagues and friends. Here, I would like to thank Dr. Manoj Kumar Manna, who guided me about the magnetic tweezer setup; Dr. Wu Fei and Mr. Lu Chen, who helped me a lot in the beginning of my research; Thuan Beng Saw, a talented young undergraduate student who also helped me in many aspects of the experiments. I am also grateful to Chen Zhengwei, Mr. Teo Hoon Hwee, Sin Yin, Viet and Tuan for their help.

Last and the most important, thank my parents who gave me unconditional love and support. Their encouragement helped me when I faced the challenges. I love them.

TABLE OF CONTENTS

SUMMARY

This thesis is mainly divided into two parts, first is the study of the interactions between like-charge colloidal particles under alternating electric field, the other is to prove a mechanosensing mechanism centered on α-catenin in cell-cell adhesions.

Colloidal systems have attracted considerable attention in recent years for their potential in serving as alternative approaches for atoms system to study the mechanisms of crystallization, glass transition, melting, *etc.* Different with atoms, colloidal particles are large enough for direct observations by normal light microscope, and their relatively slow movement can be followed in single-particle level. Considering that the colloidal particles in our experiments carry some residual negative charges on their surface, in this work, electric field will be used to control the colloidal self-assembly. Meanwhile, since the properties of colloidal systems, such as the structure, the stability and their phases, are strongly dependent on the inter-particle interactions, understanding the interactions between charged colloids is of great importance. According to classical DLVO theory, the interactions between isolated pairwise like-charged colloidal particles in ionic solutions should be purely repulsive Coulomb interaction. However, our measurements, with external field and confinement on concentrated colloidal system, suggest that the inter-particle potential exhibit a long-range attractive component.

In chapter 1, I reviewed the background on colloidal system and the interactions between colloidal particles. In chapter 2, I presented the experimental methods and analysis processes used for my thesis. In chapter 3, we demonstrated two novel and steady approaches for patterned 2D colloidal self-assembly and immobilization. One is based on de-wetting method along a copper grid, the other is by

utilizing an AEF controlled colloidal assembly on the lithographically template electrodes. Both of these two methods can be used as a general method for different colloidal systems.

In chapter 4, we measured the radial distribution function around fixed colloidal spheres and then obtained the effective interaction potential by inversion following the Boltzmann distribution. From the effective interaction potential we observed the anomalous long-range attraction between like-charge colloidal spheres under influence of AEF. We studied the magnitude and the effective force range of this attraction and ruled out the possibility of several potential forces such as the EHD induced Stokes force, van der Waals force and dipole-dipole interaction. We further confirmed several parameters determine this attractive potential, they are sphere diameter, electric field strength and electric field frequency. The many-body effect was taken into consideration and we found that in our particular system it was not significant until the sphere density reached a critical value. Based on the qualitative comparison and literature review we proposed a mechanism explaining the origin of this attraction to be the redistribution of the counter-ions around the spheres. The results predicted by this mechanism agreed well with the experimental data. Further research will be needed for complete understanding of this mechanism.

In chapter 5, single molecule technologies are used to study the mechanosensing mechanism centered on α-catenin in cell-cell adhesion. We studied the mechanical stability of α-catenin and found that this protein undergo well-defined characteristic unfolding steps with a minimal stepsize of nearly 10 nm. In addition, we also measured the binding affinity between α-catenin and vinculin, in the presence and absence of external force. The results are consistent with our proposed mechanism

that the α-catenin conformation change due to the external force stretching would unfurl the cryptic binding sites for vinculin and then activate the binding to vinculin, which in turn recruit other binding partners to strengthen the link. In this way, the cells can sense the mechanical load and then transduce it into biochemical signals that direct the cellular response. Though similar hypothesis has been put forward for years, our results is the first direct experimental evidence in single molecule levels. Considering the force-induced talin binding to vinculin which enriched at the cell-matrix adhesion, we believed such mechanism could be a general mechanosensing mechanism.

LIST OF TABLES

LIST OF FIGURES

LIST OF ABBREVIATIONS

DVM	Digital Video Microscope
2D	Two-dimensional
3D	Three-dimensional
DEF	Direct electrical field
AEF	Alternating electrical field
DLS	Dynamic Light Scattering
EP	Electrophoresis
TIRFm	Total Internal Reflection Fluorescence microscopy
MCT	Magnetic Chaining Technique
OT	Optical Tweezers
AFM	Atomic Force Microscope
RDF	Radial Distribution Function
DEP	Dielectrophoresis
EHD	Electrohydrodynamics
PS	Polystyrene
ITO	Indium Tin Oxide
ROI	Region of interest
AJs	Adhesion junctions
EC	Extracellular domain
ECM	Extra-cellular matrix
WLC	Worm-Like-Chain
PFP	Position of First Peak
MSA	Mean Spherical Approximation

LIST OF PUBLICATIONS

1.Yao M, **Qiu W***, Liu R, Efremov AK, Cong P, Seddiki R, *et al*. *Force-dependent conformational switch of α-catenin controls vinculin binding*. **Nature Communications**. 2014; 5

* Co-first author

2. Lu C, Wu F*, **Qiu W**, Liu R. *P130Cas substrate domain is intrinsically disordered as characterized by single-molecule force measurements*. **Biophysical Chemistry**. 2013;180:37-43.

3. Wu F, Lu C, Kumar P, Marjouf AE, **Qiu W**, Zhong SP, Lim CT, Thiery JP, Liu R. *Homophilic interaction and deformation of E-cadherin and Cadherin 7 probed by single molecule force spectroscopy*. **Archives of Biochemistry and Biophysics.** 2015 Dec 1;587:38-47

4. **Qiu W** & Liu X. *Anomalous long-range attractive potential between like-charge colloids under electric field*. Manuscript in preparation

CHAPTER 1

Introduction

1.1 Colloidal system

1.1.1 Brief introduction of colloidal system

Colloids are ubiquitous in nature and can be found in natural occurring materials such as blood, mud, sea or tap water, butter, milk or everyday consumer products such as toothpaste, paint and ink. In general, colloidal systems are multiple-phase systems in which one phase is highly dispersed in the other. Colloidal system is unlike solution, whose solute and solvents constitute only one phase. In colloids, the dispersed phase (suspended particles) usually has a size ranging from nanometers to micrometers. Based on the properties of the dispersion medium and the dispersed phase, colloids are classified as colloidal aerosols, colloidal emulsions, colloidal foams and colloidal suspensions. A more detailed colloids classification is as follows:

Medium/Phase		Dispersed phase		
		Gas	Liquid	Solid
	Gas	**None:** (all gases are soluble)	**Liquid Aerosol** Examples: Fog, hair sprays	**Solid Aerosol** Examples: Smoke, dust

Dispersion medium	Liquid	**Foam** Examples: whipped cream	**Emulsion** Examples: Milk, mayon-naise, hand cream	**Sol** Examples: Paint, pigmented ink, blood
	Solid	**Solid Foam** Examples: Aerogel, Styrofoam, pumice	**Gel** Examples: Jelly, cheese, opal, gelatin	**Solid sol** Examples: Cranberry glass, ruby glass

Table 1.1: Classification of colloids

Colloids can also be classified into hydrophilic colloids and hydrophobic colloids, based on the nature of the interaction between the colloidal particles and the dispersion medium (usually the dispersion medium is water). Hydrophilic colloids are those water-loving colloids in which the particles are attracted by water. Hydrophilic colloids are also known as reversible sols because they are thermodynamically stable. In the contrast, hydrophobic colloids are repelled by the dispersion medium (water). Hydrophobic colloids are called irreversible sols as this colloid is thermodynamically unstable.

Apart from the colloidal particle's own property, the dispersity also plays a key role in the colloidal system. The dispersity can be evaluated by the surface area per unit volume (or unit mass). For a system with smaller disperse particles, it usually has a larger dispersity and such system is less stable.

1.1.2 Colloidal system stability

Colloidal particles in some colloidal suspensions may remain monodispersed in solutions for a relatively long period of time. This phenomenon is referred

to as colloidal suspension stability and such stable colloidal suspensions are often obtained when ionic concentration of solution is low or stabilizers have been added into it.

In the contrast, if a colloidal system is not stable, within a relatively short period of time the dispersed particles would stick to each other and spontaneously form irregular particles clusters. This phenomenon, which is also referred to as coagulation or flocculation, is normally an irreversible process; once the particle clusters had formed, they will not be easily disrupted. However, under stirring or shearing, clusters disruption and re-dispersion as individual particles (this phenomenon is also referred to as peptization) can still happen.

All of these phenomena, such as flocculating, clouding and ordering, can be interpreted in terms of the interaction forces acting between the particles in colloidal systems. It has been confirmed that in colloidal systems, the inter-particle interactions can adopt diversity of forms, ranging from attractive to repulsive, from short-range to long-range, and from symmetric to asymmetric. Generally speaking in most of the physical systems, the inter-particle interactions are sums of attractions and repulsions. In details, diversity of forces can be involved in:

Attractions:

Depletion force: Depletion force is often regarded as an entropic force, and it arises when small particles are added into a mixture with large colloidal

suspended in it (1). The depletion force results from the excluded-volume interaction between the large and small particles. As figure 1.1 indicates, when large particles approached close, the small particles are then expelled from the overlap gap, leading to an osmotic pressure difference between the gap and the solution, resulting in an effective attraction. This attraction is referred to as depletion force.

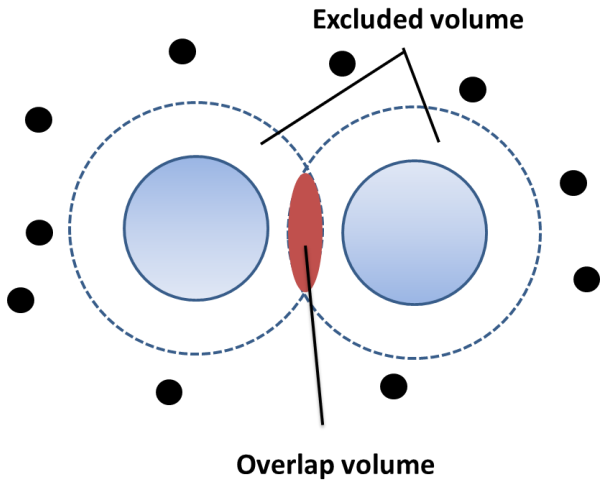

Figure 1.1: Mechanism of depletion force: Excluded volumes of large particles overlap resulted in an increase in the total volume available for smaller particles. The result is an increase of the entropy of the system and lowers the Helmholtz free energy.

Dipole-dipole interactions: Dipole-dipole interactions are electrostatic interactions between permanent molecules dipoles. Colloidal particles can usually be regarded as large dipolar molecules. Molecule dipoles are developed by inhomogeneous distribution of the electrons between different atoms, in a manner of that more negative atom would attract more electrons. This induced electron density gradient adjacent to atoms would result in the molecule dipole in which one end of the molecule dipole possesses a partially negative charge while the other end a partially positive charge. When such

molecules associate with each other, the negative end of one molecule dipole will be attracted to the positive end of the other molecule dipole.

van der Waals forces: It is widely accepted that van der Waals force is an interaction between two temporary and induced dipoles. Even though some particles do not have a permanent dipole, fluctuations of the electron density give rise to a temporary dipole. This temporary dipole will induce other dipoles in nearby particles. The temporary dipole and the induced dipole can associate with each other. This attraction is the so-called van der Waals attraction (VDW).

Repulsions:

Steric forces: Steric force is a strong repulsive force which arises from a fact that hard sphere occupies a certain amount of space. When hard core particles were brought closer to a very small distance, there is an associated cost in energy due to overlapping excluded volume.

Electrostatic repulsions and Zeta potential: Colloidal particles in electrolyte solution often carry a net charge either by absorption or ionization. In colloidal suspensions, charged particles are surrounded by an electrical double layer. Fig 1.2 illustrates a spherical electrical double layer. As illustrated, a boundary between the two layers can be found. The first layer is inside the boundary, where the surrounding counterions and the particle form a stable entity. The counterions are so firmly anchored that they will move with the particles. Beyond this boundary the co-ions are loosely attracted by the particles so that

they will not move with the particles. This boundary is also known as slipping plane. The potential on this plane is Zeta potential, which serves as a very important indicator for the system stability.

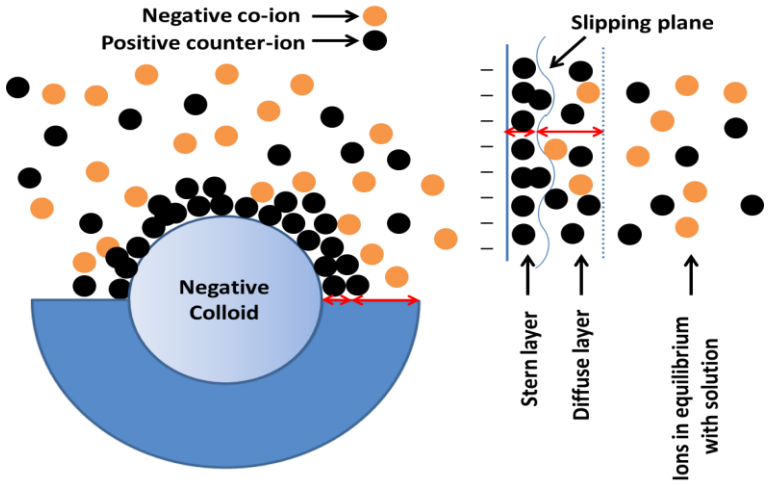

Figure 1.2: Left panel: Schematic illustration of the electrical double layer around a negative charged colloidal particle. The counterions (positively charged ions) and co-ions (negatively charged ions) are shown by black and brown dots, respectively. Right panel: Stern's model for electrical double layer. The potential at slipping plane is zeta potential.

Within the outer layer there is a balance between the electrical forces and thermal motion, leading to a counter charge and thus screening the electric particle surface charge (2). This layer is called the "diffuse layer". Beyond this layer the ions will be in equilibrium with solutions. The particle surface and diffuse layer are equally in total but opposite in charge, as a result, the complete structure is electrically neutral. The thickness of this diffuse layer is of colloidal diameter dimensions. An increase of the electrolyte concentration or an increase in the valance of counter-ions will magnify the screening effect and compact the thickness of the double layer. When colloidal particles

approach closer, overlapping of the double layer will cause a repulsive force which can prevent the particles aggregation.

1.1.3 DLVO theory

The most widely accepted model describing the overall interactions between isolated pairs of colloidal particles is the well-known DLVO theory, named after Deryagin, Landau, Verwey and Overbeek, which is developed in the 1940s (3-5). Fig 1.3 and 1.4 shows an illustration of the various components and the overall potential of the DLVO theory, respectively. According to the theory, the stability of colloidal systems is simply determined by the competition between short-range van der Waals attractions and long-range electrostatic repulsions. This theory proposes that an energy barrier resulting from the repulsive force would prevent two particles from approaching closer and finally adhering together. However, if the particles acquire sufficient energy (most likely from external force) to overcome this barrier, the attractive force will pull particles into closer contact and finally the particles can form strong and irreversible aggregation. On one hand, if the particles have a sufficiently large repulsion, the dispersion will beat flocculation and thus colloidal system will be stable. On the other hand, if the repulsion is weak, then the flocculation or coagulation will eventually take place.

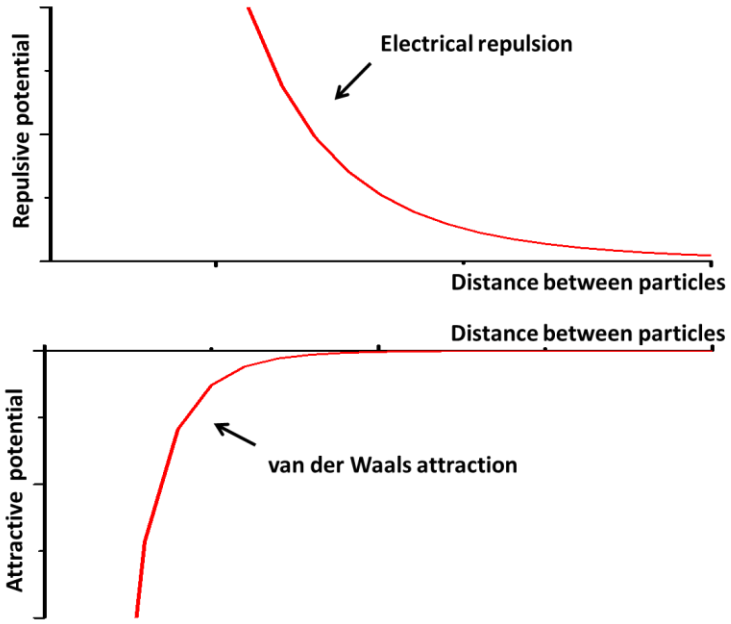

Figure 1.3: Schematic diagram of distribution of interaction potential with particle separation distance between pairwise colloidal particles. Top panel: the electrostatic repulsive potential; Bottom panel: the van der Waals attractive potential.

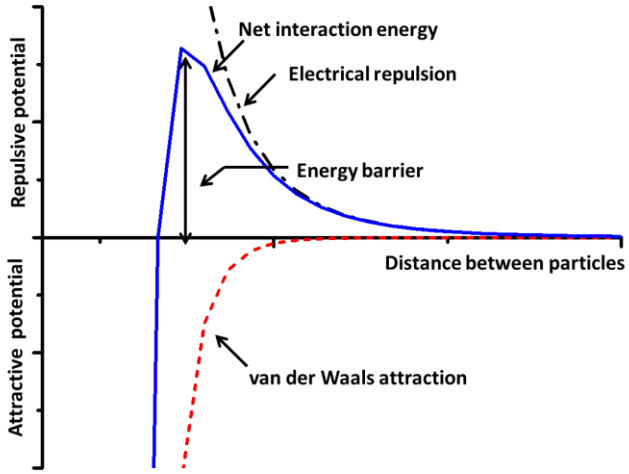

Figure 1.4: Schematic representation of DLVO theory. The net interaction potential is the sum of electrostatic repulsive and van der Waals attractive potential.

According to DLVO theory, the overall interparticle potential is simplified to the combination of attractive potential and repulsive potential.

$$V_{DLVO}(r) = V_R(r) + V_A(r) \tag{1.1}$$

The interaction curves can be used to judge the stability of the system at rest and under external forces.

So far, the interactions and interaction potentials between charged colloidal particles have been measured with a variety of techniques (6-8). In most situations, good agreements between DLVO theory and experiment data have been obtained. However, some anomalies, including large stable voids in otherwise homogeneous suspensions (9, 10) and equilibrium phase separation between colloidal fluids of different densities (11), are of great controversy to this established theory.

Previously, DLVO theory made a prediction that an isolated pair of like-charge colloidal spheres in an ionic solution should experience a purely electrostatic repulsions (4, 12), which has already been verified both by direct measurements and simulations (13-15). However, later experiments, studying the particles interactions in a concentrated colloidal suspension which are confined by charged glass walls (15, 18-21) or external field, conflict this prediction because a long-range attractive component was clearly observed in the effective inter-particle potentials (16, 17). This amazing observation suggests that such long-range attractive interactions may be responsible for those series of unexplained phenomena mentioned in last paragraph which were observed over the past decade in bulk colloidal suspensions. Therefore, understanding the mechanism of long-range attraction arouse great interests in colloidal science and the DLVO theory requires substantial supplements.

1.2 Applications and implications of colloidal

High quality crystals free of defects are required quantitatively in many fields. Therefore, control on crystallization process is critical. The full understanding of crystallization mechanism is far from being complete although physical and chemical scientist had devoted for more than one century. The main challenge for studying the atoms systems is the fact that crystal atoms are not only too small but also moving too fast for direct observation. Colloidal models are developed as an alternative approach to study the physical behavior of atoms during crystallization. This is because firstly the colloidal particles are large enough for direct observation with Digital Video Microscope (DVM). Nevertheless, the relatively slow movement of colloidal particles also makes the tracking in real time at single-particle level possible. Secondly, a variety of forces are associating with the structures and the behaviors of colloidal suspensions, which is similar to those among atoms and molecules. Thirdly, colloidal particles in solutions can exhibit equilibrium phases, such as gas, liquid and solid, and undergo phase transitions, being analogous to that of atomic systems. Based upon these features, the colloidal particles can be regarded as big "atoms". So far, the colloidal system has been employed in studying fields such as phase transitions, crystallization (22-26), glass transition (27-29), melting (30, 31), *etc.*

Apart from above, patterned colloidal systems with lattice spacing ranging from nanometers to micrometers can diffract ultraviolet, visible, and near-infrared light. Thus, by precisely controlling the self-assembly of colloidal particles, colloidal systems can realize a variety of applications, such as

sensors (32, 33), narrow-band optical filters (34), optical switches, photonic band gap materials, waveguides (35), and other types of optical and electro-optical devices (36).

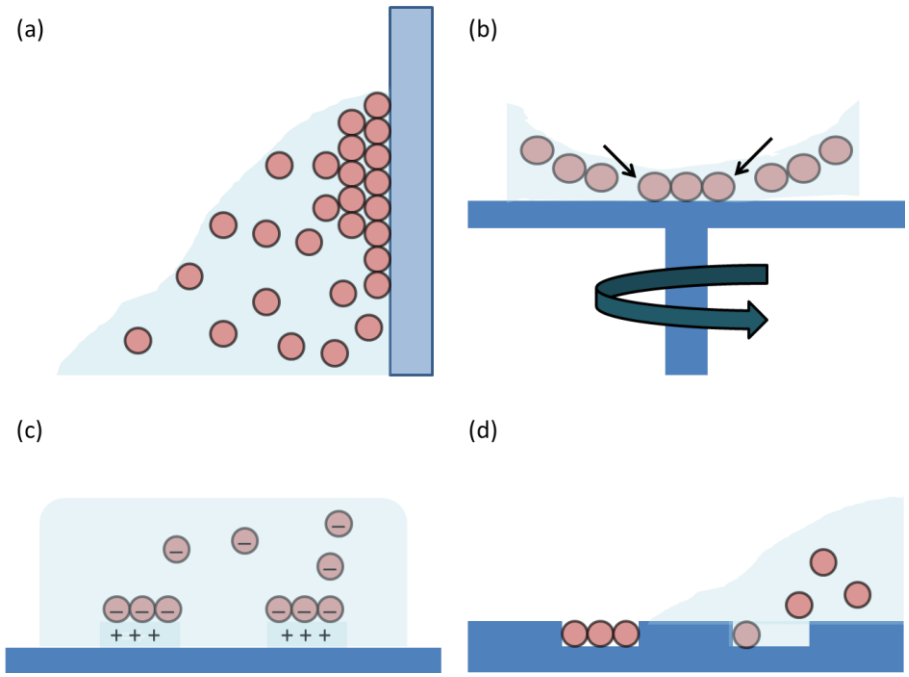

Figure 1.5: Self-assembly strategies to create patterned colloidal particles structures: (a) Dip-coating. Capillary forces and controlled evaporation control colloidal self-organization (37). (b) Spin-coating. Capillary forces and shear forces drive colloidal self-organization (38). (c) Selectively deposition of colloids on substrate modified with patterned chemicals or charges (39-43). (d) Selective deposition of colloids on physically patterned substrate in assistance of solution evaporation (44).

There is great interest in utilizing the colloidal self-assembly to create templates for three-dimensional (3D)/two-dimensional (2D) periodic structures. Fig 1.5 illustrates several processes for controlled colloidal self-assembly. These traditional methods, such as flow induced or evaporation induced colloidal assembly, display disadvantages that the fine-tuning of the structures and geometries is nearly impossible. Moreover, these methods are involved in slow but complicated procedures and usually left some intrinsic defects. Consequently, a novel and simpler method for patterned colloidal particles

self-assembly into crystals with well controlled phases and structures is needed.

External field, such as gravity, confining walls, temperature gradient, electric and magnetic fields, can be used to direct the assembly of colloids into desired patterns. Among these external fields, alternating current electric field (AEF) stands out due to several advantages, which would be introduced in the following section.

1.3 Controlled colloidal assembly under an Alternating Electric Field

Generally speaking, colloidal particles in ionic solutions always acquire some residual charges on their surface, either by adsorption or ionization. Therefore, playing with the charge is a natural and widely used strategy in controlling the behavior of colloidal particles and the colloidal phase transitions (45-52). In fact, electric field is one of the most effective ways for controlling the colloidal particles self-assembly. For example, when a direct electrical field (DEF) is applied to charged PMMA beads, dipole-dipole interactions will induce a chain-like structure (53). Numerous efforts have been dedicated to study the behavior of colloidal assembly under alternating electric field (AEF) by Liu *et al.* It is interesting that AEF have been found to organize colloid particles into complex configurations, such as circulating chevron bands (54, 55), vortex rings (56), binary super-lattice structures (57), and 2D crystals (48, 58).

AEF has the ability to micro-tune the forces exerted on colloids. Considering that all parameters, which characterizing AEF properties including field strength, frequency, wave symmetry and phase, can be electronic controlled instantly without disturbing the original solutions, and these parameters will influence the interactions following different mechanisms without distorting each other. This allows fine adjustment of the applied force to an extent which is nearly impossible by other techniques like liquid flow, evaporation, sedimentation or mechanical manipulation.

By combination of the AEF and the application of confocal microscopes technique, the precisely controlled colloidal 3D structures formation and observation at single-particle level can be achieved. Due to the limit of spatial resolution and the scanning speed, 3D process is difficult to be recorded in real-time. In contrast, 2D colloidal model systems can be tracked in real-time using normal light microscope equipped with high speed CCD cameras. In principle, 3D and 2D colloidal model are not exactly the same. However, 2D is the basis for 3D because both share varieties of common features in most aspects. Thus a sufficient understanding of 2D model is necessary before further development of 3D colloidal assembly.

1.4 Review on colloidal particles interaction

1.4.1 Techniques measuring interactions

Colloidal systems are thermodynamic systems consisting of a large quantity of particles in solutions and their macroscopic properties are mainly determined

by the inter-particle interactions. In last decades, due to the limitation of direct measurement techniques on nanometer and micrometer particles interactions, the colloidal system investigation mainly focused on the macroscopic properties, such as measuring the Brownian motion and particle size with assistance of Dynamic Light Scattering (DLS), measuring the sphere charge using electrophoresis (EP) and evaluating the stability of the systems by measuring the turbidity. All of above techniques can look into the bulk properties. However, the bulk properties are quite insensitive to the form and nature of the local interaction potential between particles, and such measurements always reflect many-body contributions. Not to mention the light scattering data is notoriously sensitive to noise. Until since nearly 20 years ago, single molecule techniques have emerged as powerful tools to directly measure the forces exerting on charged particles from a few femto-Newtons to sub-pico-Newtons. For example, Total Internal Reflection Fluorescence microscopy (TIRFm) is used to measure the interaction between a sphere and a flat surface (59). Magnetic Chaining Technique (MCT) has been used to directly probe the force-distance profile between magnetic colloidal particles (60, 61). Optical Tweezers (OT) and Atomic Force Microscopy (AFM) can also manipulate colloidal systems and have been used in recent years to directly investigate the interactions (62-66). Although these techniques are powerful to a certain extent, high requirement on the sample preparation greatly limits their wide application. For example, TIRFm and MCT can only manipulate fluorescent and magnetic beads, respectively. As for AFM, Ducker *et al. (67)* successfully fixed a particle on the tip of an AFM cantilever while other particles attached on a mica substrate, in this way, the interactions can be measured by ap-

proaching them close. Although AFM can measure the inter-particles interactions, but this technique requires the beads to be large enough to be trapped, and the binding between substrate and the particles would have influence on the real pairwise interactions.

It is also possible to measure interaction forces by inverting the pair correlation function g(r) (also known as Radial Distribution Function, RDF) in the case of weakly interaction systems using the Boltzmann distribution,

$$g(r) = \exp[-U(r) / k_B T] \tag{1.2}$$

This relationship has been proved to be accurate for sufficiently diluted dispersions. At higher concentrations, the calculated U(r) will not be the real pair potential but larger effective potential which includes the true pair potential and the effect of many-body correlations. The details of this inverting method will be introduced in chapter 2, Method & Materials.

1.4.2 Review on colloidal assembly and interactions under electrical field

Electrical field can manipulate colloidal assembly in a convenient and steady way. Besides, the mechanism is quite complex. In general, electric field will drive motions of both particles and the surrounding liquid. Based on the mobility of the particles and of the liquid, electric field effect can be classified into four broad categories.

1, Electrophoresis: Fig 1.6(a) shows a schematic of the electrophoresis process. Charged particles are attracted to the oppositely charged electrode in DC field.

Although the entirety of particle and its surrounding electric double layer is electro-neutral, the co-ions in diffuse layer are loosely trapped by the particle surface charge and thus can be sheared away by external electric field, resulting in those ions moving toward the electrode carrying opposite charges.

2, Electroosmosis: Fig 1.6(b) shows a schematic of the electroosmosis process, liquid flows (together with the particles) are driven by the moving counterionic layer near the substrate between the electrodes. When particles dispersed in ionic medium, the container substrate in contact with ionic media always develop a surface charge, with the induced counterionic double layer adjacent to the interface of substrate and the medium. These ions will move toward the oppositely charged electrode, dragging the liquid, and resulting in electroosmotic water motion.

3, Dielectrophoresis (DEP): Fig 1.6(c) shows a schematic of the DEP process, AC field applied on colloidal suspensions will emerge DEP forces. As signs of electrode polarization keep switching at a constant frequency, the particles will not be attracted directly to electrodes by the electrostatic interactions. The induced dipoles of the particles disrupt the heterogeneous electric field near the surface, result in the dielectrophoresis force. The DEP effects are very complex when the particles are close enough.

4, AC Electrohydrodynamics flow (EHD): Fig 1.6(D) shows a schematic of the EHD flow process, the origin of EHD flow can be explained in a simplified way as follows, the dissolved electrolyte ionic species will build up an

electric double layer adjacent to the electrode/specimen interface, which can be disrupted by the presence of charged colloidal particles (usually other confinements will also disrupt this double layer). The disruption of the double layer will develop spatially varying free charges. In addition, the presence of charged colloidal particles can also associate with the external alternating electric field, leading to a lateral electric field. The interactions between the free charges and the lateral electric field will establish the EHD flow (71, 120, 121).

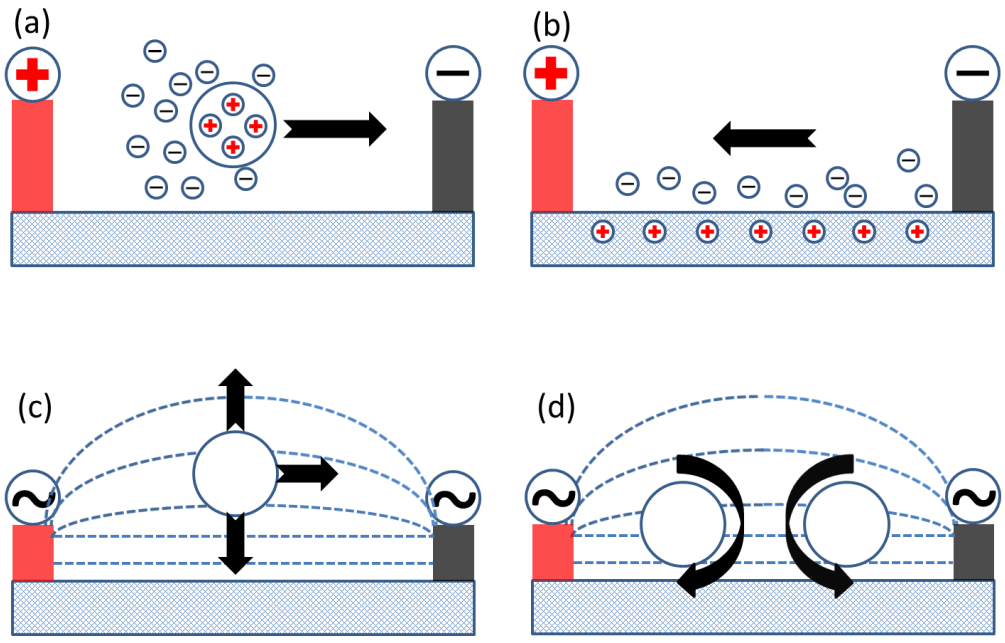

Figure 1.6: Schematic of electric field driven effects on movement of colloidal particles and of liquid. (a) Electrophoresis. (b) Electroosmotic. (c) Dielectrophoresis. (d) Electrohydrodynamic flow.

EHD flows have been reported to be an effective method to assemble latex particles by Trau *et al.* (48, 68) and Bohmer (47). In their study, the EHD flows in effect pull the particles together to form 2D crystals at the electrode surface (69, 70). Since my project will apply AEF on the colloidal suspension which is confined by two electrode glasses, the electrohydrodynamic flow

would have great influence on the colloidal suspension. Thus, a better understanding for the EHD flow would be essential.

According to Ristenpart *et al.* (71, 72), the EHD tangential velocity is a function of the electrolyte concentration, field strength and frequency,

$$u \sim \frac{3\varepsilon\varepsilon_0}{\mu\kappa} E_\infty^2 \{C_0^{'} + \frac{D\kappa^2}{\omega} C_0^{''}\} \tag{1.3}$$

ε_0 and ε is the permittivity of free space and medium, respectively. μ is the fluid's shear viscosity. E_∞ is the strength of the electric field, κ is the reciprocal Debye length, D is the ionic diffusion coefficient and ω is the angular frequency of the AEF with $\omega=2\pi f$. $C_0^{'}$ and $C_0^{''}$ are parameters associated with the dipole coefficient.

1.5 Objectives

In this thesis, inter-particle interactions under AEF will be studied. To obtain a comprehensive understanding, the objectives of this thesis are summarized as:

(1) To propose novel but steady methods for patterned colloidal assembly and immobilization.

(2) To study the inter-particle interaction potential under AEF by inversion of the RDF with distance between particles.

(3) To identify the inter-particle interaction potential with change of parameters such as field strength, frequency, particle size, cluster shape, particles concentration etc.

(4) To develop a mechanism explaining the long-range attraction observed in the experiments

(4) To verify the mechanism by comparing theoretical and experimental data.

1.6 Significance

The novel patterned colloidal self-assembly and immobilization method should have great potential in further creating 2D structures with desired patterns. The inverting method from RDF to potential should contribute to future study due to its simple experiment design. Discovery of the long-range attraction and the proposed mechanism help us to have a better and deeper understanding about the intrinsic interactions among colloidal particles.

1.7 Scope and limitation

All experiments were carried out in 2D because there are several technical limitations for visualization and quantitative treatment in 3D. As 3D and 2D share many features in common in nearly all aspects, thus, the analysis on 2D can be applied to 3D, and *vice versa*. In addition, by combination of fluorescence beads with the utilization of confocal microscopy techniques, the 3D colloidal interactions experiments should also be available.

So far we only measured the interaction potential between the polystyrene (PS) beads with different diameters. The reason why we only choose PS is that it is one of the most typical kinds of colloidal particles which had been intensively studied. In future, we can apply the study on other kinds of colloidal particles, such as particles made of other materials (PMMA, latex *etc.*), particles carrying positive charges and particles with functional groups on their surfaces. The

results would be interesting and meaningful as supplements for full understanding of colloidal sphere interaction.

CHAPTER 2

Materials, Method and Data analysis

2.1 Materials and Experimental Techniques

2.1.1 Preparation of the colloidal suspension

The colloidal suspension in the experiment was consisted of negative charge stabilized polystyrene (PS) spheres (diameter of 1 um, 1.3 um and 2 um, Duke Scientific). The PS beads suspension was washed in de-ionized water (DI water with resistivity~18.2 MΩ cm^{-1}) and centrifuged several times to remove the surfactants. Then this washed suspension was re-dispersed uniformly either in DI water or 0.05 mM sodium chloride (NaCl) solution. The zeta potential of the colloidal particles at pH=10 (Thermo scientific, Orion^{TM} star A215 pH meter) was measured to be $\zeta = -50 \pm 1.4$ mV by Zetasizer (Marven, Zetasizer 2000).

2.1.2 Experimental setup

The experimental setup was similar to that described in ref. (52) with some minor improvements. Figure 2.1 shows a schematic diagram of the traditional experimental setup. The freshly prepared colloidal suspension of PS spheres was sandwiched in a glass cell composed of two pieces of conductive indium

tin oxide (ITO) glasses (glass substrate was 1 cm in diameter; thickness of coating was 15-30 nm; sheet resistance was ~100 Ω/cm^2) separated by a spacer. Figure 2.2 shows pictures of the experimental cells with different spacers used in this work, either by previously a glass spacer or nowadays a double side tape spacer (H=120±5 um and H=100±10 um, respectively). The opening end of the cell was sealed to prevent leaking by UV adhesive (Norland Industry, Norland Optical Adhesive 68) after the suspension was added.

During the experiments, with an alternating electric field applied on the electrodes and the colloidal suspension, a series of experiments would be carried out on condition of varying parameters such as frequency f and field strength $E_{0.}$ The capturing rate (2 frames s^{-1}) and size of the region of interest (1280 x 960 pixels, corresponding to 200 x 150 um under the 63X and long working distance objective) is fixed with as long as 5 minutes of continuous *in situ* videos were recorded by a digital imaging camera (Leica, DFC495) which is mounted on a Leica DM600B microscope to determine the position of each particles or clusters during the experiments.

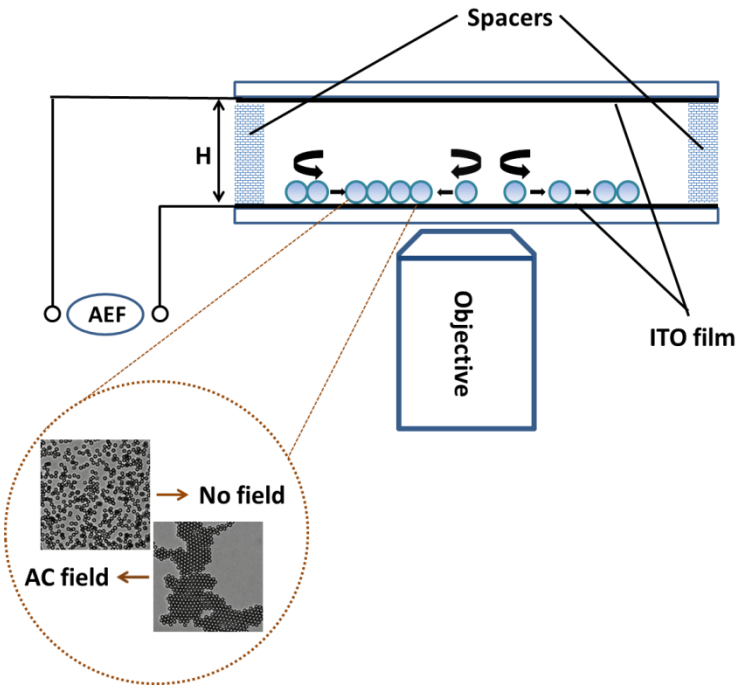

Figure 2.1: Schematic of experiment cell setup. The colloidal suspension is added and sealed between two ITO-coated glass plates separated by spacers (glass or double side tape).

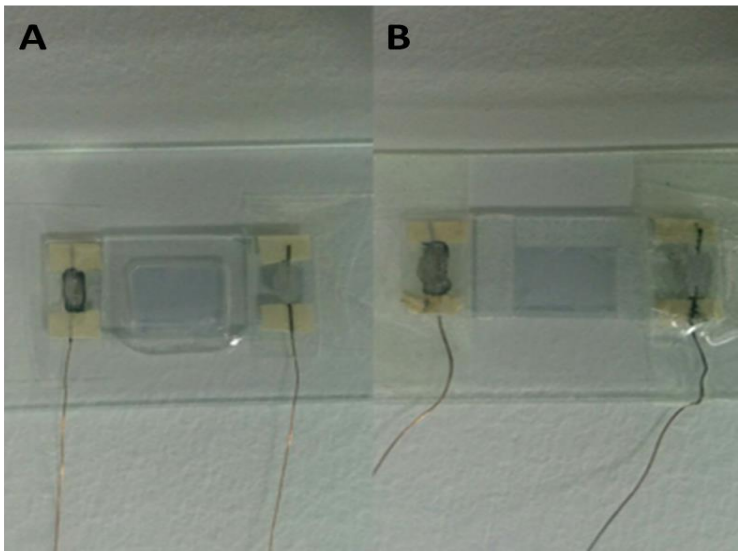

Figure 2.2: (A). Experimental cell with glass spacer (Thickness $H=120\pm5$ *um*) (B). Experimental cell with double side tape spacer (Thickness $H=110\pm10$ *um*). The opening end was used for the adding sample and afterwards would be sealed with UV adhesive. Copper wire linked the ITO glass to AC signal generator.

2.1.3 Zetasizer

As mentioned in the electrical double layer theory, the potential on the boundary between stern layer and diffusion layer is known as Zeta potential (ζ potential). The value of ζ potential reveals the colloidal system stability. In experience, if particles have a large negative or positive ζ potential (>25 mV or <-25 mV), then such particle would tend to repel each other and there is low probability for such particle flocculation. In this situation, we regard this particle suspension thermodynamically stable. On the contrary, if particles have relatively small ζ potential values, then the repulsion would not be sufficient to prevent particles aggregation.

Zeta potential (mV)	Stability behavior of the colloidal suspensions
From 0 to ±5,	Rapidly coagulate or flocculate
From ±10 to ± 30	Incipient instability
From ±30 to ±40	Moderate stability
From ±40 to ±60	Good stability
More than ±61	Excellent stability

Table 2.1: Effect of zeta potential on colloidal suspensions stability (73, 74).

As ζ potential serves as an indicator of the stability of colloidal suspensions, ζ potential should be measured in advance. The measurement of ζ potential is realized through Zetasizer. As pH value of the solution greatly affects ζ potential, so ζ potential and pH values measurement are always conducted together. Moreover, for accuracy, the ζ potential measurement requires the samples to be as diluted as possible.

2.2 Data Analysis

2.2.1 Determining beads center position

During the experiments, the particles movement under AEF was recorded and saved in a video. Images were captured from the video with a rate of 2 frames per second. In order to obtain statistically convincing data, more than 500 frames were analyzed one by one in each procedure. The first step of image processing is to identify the location of each colloidal particle. The basic idea is to group all the pixels in ROI with brightness within a certain range of value, so the beads can be distinguished from the blank. Then the center of the individual beads or clusters can be determined using standard procedure (14, 75, 76). Figure 2.3 illustrates the process of determining the beads center positions. Fig 2.3(A) is an example of images taken from the video recording 1.3μm beads movements. Fig 2.3(B) shows the same image in (A) which has been applied a threshold on it. Proper threshold can greatly improve the spatial accuracy in the determination of the center of the beads. Fig 2.3(C) is the image recording the location of every bead in each frame. Every small blue spot represents a bead center's position while the large red circle is chosen to be the region of interest for determining the radial distribution function around our reference beads. This process would be repeated for each frame to acquire the g(r) curves respectively. Subsequently the average g(r) results can be calculated.

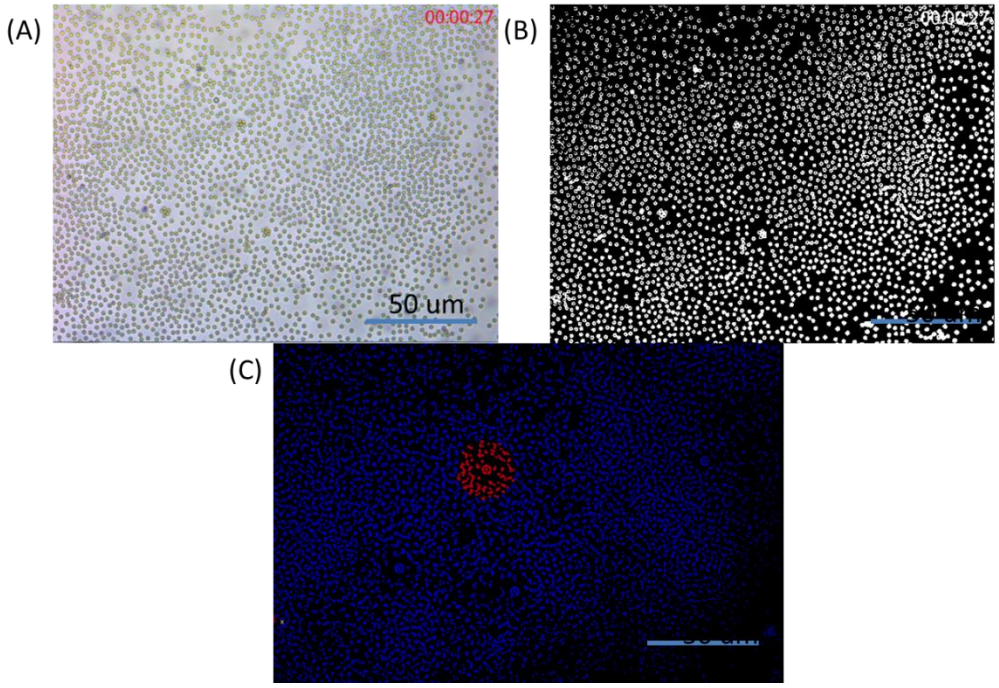

Figure 2.3: (A): Image taken from video without any treatment; (B): Apply threshold on the image of (A) using ImageJ software under standard procedure. Afterwards beads center's location can be obtained; (C): Every small blue spot represents a bead center's position, the red large circle is the region for determination of the radial distribution function.

2.2.2 Radial Distribution Function g(r)

The radial distribution function (also known as pair correlation function) g(r) describes the probability of finding a particle varies as a function of distance r away from the reference particle. From beads center position distribution, g(r) can be directly calculated following function described by Bongers *et al.*(76):

$$g^{2D}(r) = \frac{n_d}{2\pi r \rho \Delta r} \tag{2.1}$$

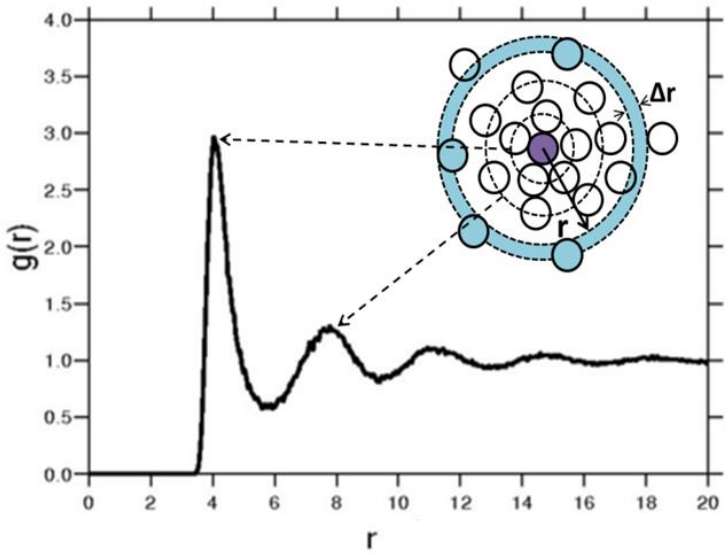

Figure 2.4: Illustration of Radial Distribution Function. The purple particle serves as the reference particle, the peak location of g(r) corresponding to the center-center equilibrium distance.

Where n_d is the number of particles found in a ring with an inner radius of r-$0.5\Delta r$ and an outer radius of $r+0.5\Delta r$, Δr is the width of the ring, and ρ is the average density of spheres. Fig 2.4 illustrates an example of radial distribution function g(r).

In our data analysis process, several previously fixed beads were chosen as the reference beads, Δr was set to be 0.2a, where "a" is the radius of the bead (for even smaller Δr value, the g(r) curves were not continuous, as for larger Δr value, many detailed information would not be revealed). Theoretically to calculate the most accurate g(r), the counting areas should be as large as possible. However, due to the fact that the fixed beads on the substrate are not far away separated and such fixed beads would have impact on the real g(r). The region of interest was chosen to be a large round circle with its radius equal to 5 times of the beads diameter (the large red circle as shown in

Fig.2.3c), which had proven to be large enough because within this boundary the g(r) curve already started to oscillate around g(r)=1 (g(r)=1 means the beads at that separation are non-relevant to the reference bead).

2.2.3 Inter-particle interaction Potential u(r)

Colloidal particles behavior in suspension under AEF is controlled by the net force they sensed, including the interactions between particles and the liquid dragging force such as the EHD flow.

When colloidal suspension is in thermodynamic equilibrium state, assuming the inter-particle interaction potential as the only factor that determines the beads position distribution, then g(r), in first approximation, would follow the Boltzmann Distribution law:

$$\frac{N_i}{Nall} = \frac{\exp(-\frac{u_i}{k_b T})}{\sum \exp(-\frac{u_i}{k_b T})}, \rho_i = \frac{N_i}{Nall}, \rho_j = \frac{N_j}{Nall} \tag{2.2}$$

$$\frac{\rho_i}{\rho_j} = \frac{\exp(-\frac{u_i}{k_b T})}{\exp(-\frac{u_j}{k_b T})} = \exp[-\frac{(u_i - u_j)}{k_b T}] = \exp(-\frac{\Delta u}{k_b T}) \tag{2.3}$$

$$g(r) = \exp(-\frac{u}{k_b T}),\ u = -k_b T \ln[g(r)] \tag{2.4}$$

In this way, the pair potentials u(r) can be directly inverted from g(r). This inversion method has been proved accurate for extremely diluted systems, especially ideal for pairwise of colloidal particles. As for our colloidal systems, where the experiments were conducted in a much concentrated regimes of the

particle density, the influence of the nearby particles can't be neglected. Thus, the many body effect correlation should be taken into consideration. In this study we also investigated an alternative general method that allowed for the determination of the "effective inter-particle pair potential u(r)", based on the two-dimensional version of the Ornstein-Zernike (OZ) equation together with its following closure relation. The details would be presented in the results chapter.

CHAPTER 3

Patterning and Immobilization of Colloidal Assembly

3.1 Introduction

Orderly spaced colloidal systems are greatly in demand in many fields such as sensors, optical filters, photonic band gap crystals *etc.* The primary requirement for the success of these applications is to pattern and immobilize the colloidal assembly. As a consequence, precisely controlling the colloidal self-assembly to create a template for 3D/2D periodic structure aroused our great interest. Another reason why the patterning and immobilization is so important is that they are the basis for my further research. i) The immobilization pattern can serve as a template for further research. Xie *et al.* studied the colloidal epitaxial crystallization by introducing a line template (77), which is created by a designed patterned self-assembly. ii) One of my studies focused on the interaction among colloidal particles by recording the positions of reference beads and the other beads around that reference bead. Due to Brownian motion, the thermal drift of beads would not be neglected if the reference beads are not fixed, especially when the measurement takes a relatively long time. iii) Study of the interactions between heterogeneous beads (different diameters, dimensions, surface modification, *etc.*) requires the immobilization of the first series of beads and then adding a second series of beads.

In my study, two novel and steady approaches to pattern and immobilize colloidal self-assembly on substrate had been realized, and these methods should shed light to the future study.

3.2 Results and Discussion

3.2.1 Colloidal Assembly Patterned with a Copper Grid

The first method to assemble the colloidal particles into desired patterns is de-wetting lithography. The de-wetting lithography experiment setup is illustrated in Fig 3.1, which is a simple deposition cell where an aqueous colloidal suspension is placed between a floating copper micro grid serving as the deposition template and the ITO glass substrate.

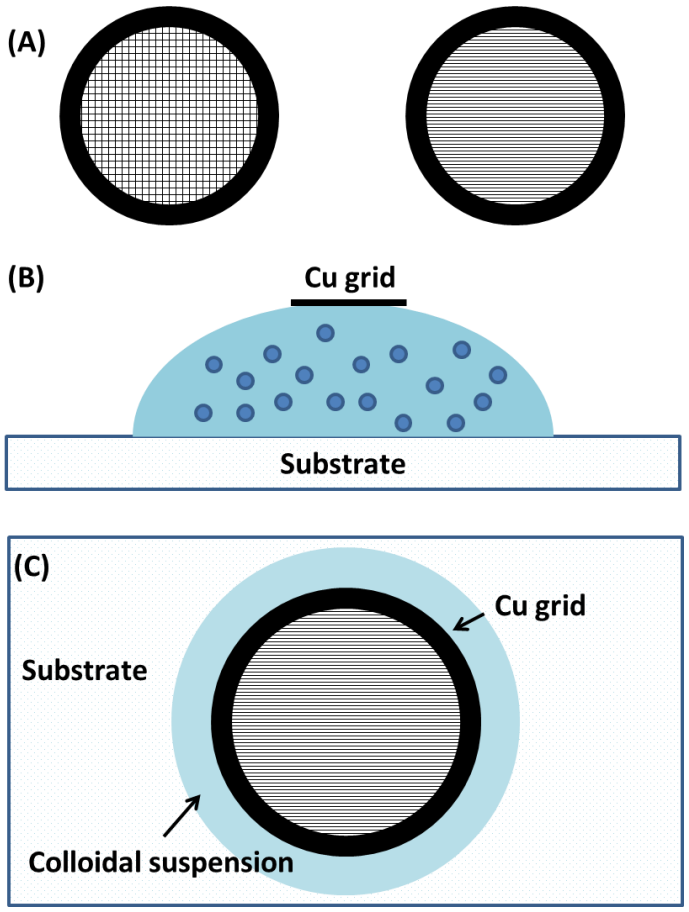

Figure 3.1: Setup of copper grid de-wetting lithography. (A): Copper grid serves as deposition template. Grid geometry determines the pattern of colloidal self-assembly. Left: Mesh grid (Gilder Grids, G200-C3); Right: Line grid (Gilder Grids, G300P); (B) Side view of the Copper grid and the colloidal suspension; (C) Top view of the Copper grid and the colloidal suspension.

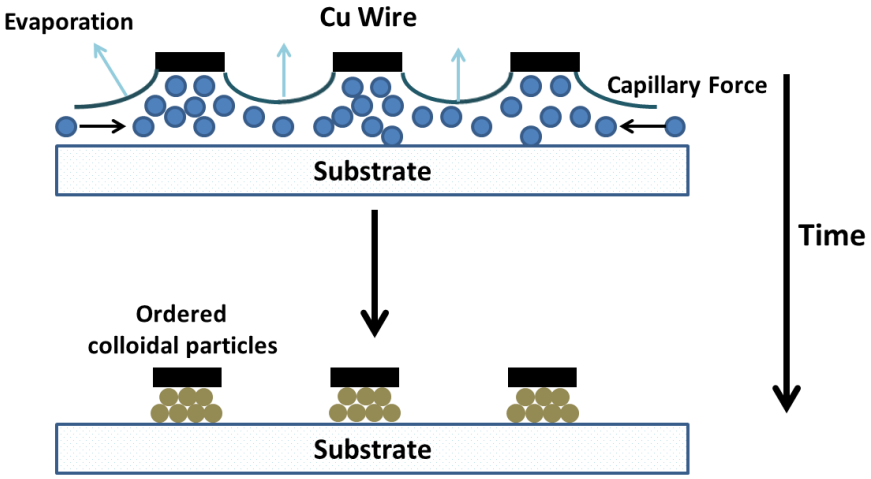

Figure 3.2: Schematic of the de-wetting lithography steps.

To realize the patterned colloidal assembly, a drop of 5 μL colloidal suspension (1.3 um PS beads with volume fraction ranged from 0.1% to 0.01%) was applied on the substrate first. This suspension uniformly wetted the substrate and formed a meniscus while the center of the meniscus is relatively flat. Afterward, the copper gird was quickly and carefully placed over this suspension. The temperature and humidity condition was controlled to be constant during the evaporation process (temperature=25±5 ℃ and humidity=50±10%, respectively), the total drying time was about 30 minutes. During drying, capillary force transported the particles under the template to form the pattern, as shown in Fig 3.2. After a sufficient drying time, the grid was removed via physical lift off and the formed colloidal assembly pattern was left on the substrate. The assembly pattern was determined by the grid template geometry. In addition, the band width can also be controlled by changing the particle suspension concentrations. For example, Figure 3.3 shows the optical microscopy images of the PS particles assembled into desired linear pattern with different band width. Moreover, this de-wetting method is also available for colloidal particles with different diameters.

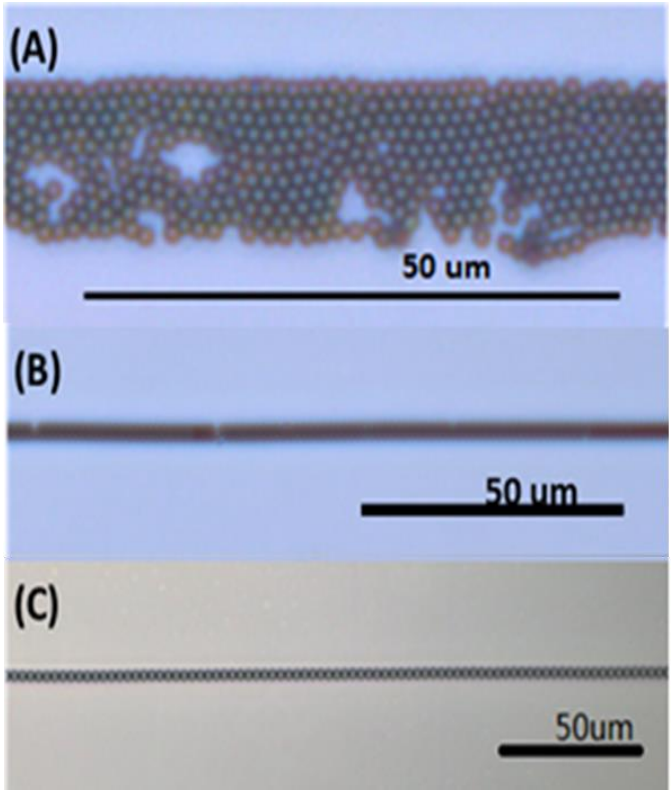

Figure 3.3: Optical microscopy images of copper grid patterned colloidal assembly. Linear colloidal assembly with width of (A), eight-particles (1.3μm), *Φ= 0.1%*. (B), two-particles (1.3μm), *Φ= 0.5%*. (C), one-particle (3μm), Φ= *0.01%*.

3.2.2 Colloidal Assembly Patterned with surface modification

Another method to assemble the colloidal particles into desired pattern is the modification of substrate surface, either by patterned chemical modification or patterned topography. Patterned chemical modification (40) led to a preferential adsorption of particles to the selected areas. Patterned topography of the substrate such as wells (78) or microfluidic channels (79) confined colloids and then controlled the colloidal self-assembly. It is reported that a variety of different lattices can be obtained by altering the ratio of the size of the particle to the size of the pattern's feature.

The patterned modification either by chemical or topography methods so far fail to assemble high quality periodic and well-ordered lattices. In this thesis, surface modification was combined with an alternating electric field to realize fine-tune of the structures of colloidal self-assembly. In particularly, surface modified electrode will attract the colloidal particles from suspension and roughly determine the pattern first, and then the AEF will be applied to finely adjust the assembly structure and to finally permanently immobilize the assembly on the substrate. This novel method has been proved to be a simpler but more efficient way.

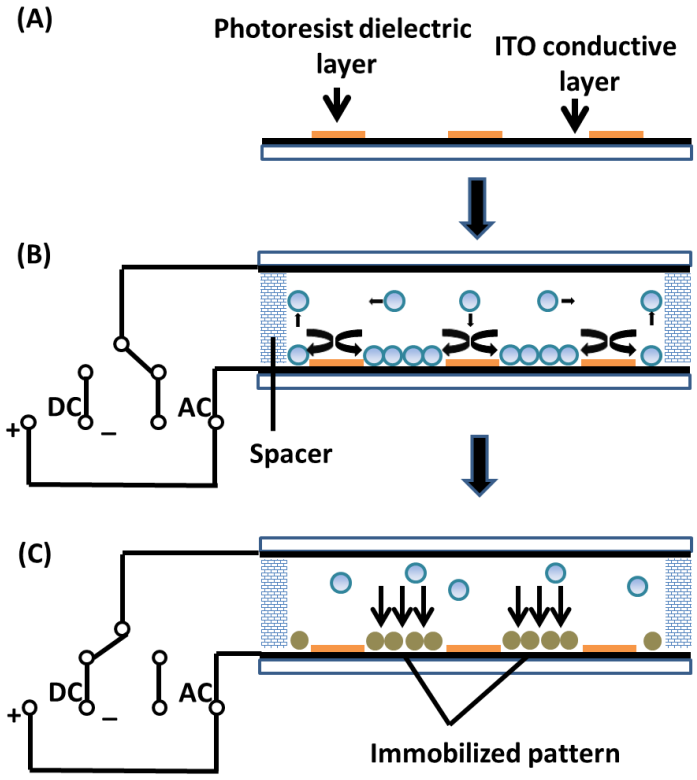

Figure 3.4: Schematic illustration of the processes to combine surface photolithography with AEF to guide and tune the colloidal assembly and then permanently immobilize it by switching to DEF.

The experiment setup is similar as the one mentioned in Chapter 2, the negatively charged polystyrene colloidal suspension was sandwiched and sealed in a cell composed of two glasses which were coated with a thin layer of ITO that serves as conductive electrode. Fig 3.4(A) shows the ITO glass which bottom surface was previously covered with a thin layer of patterned photoresist film following standard photolithography procedures. This photoresist film is not conductive thus can serve as the dielectric layer. Fig 3.4(B) illustrates the procedure when an AEF was applied on the suspension. By changing the AEF frequency and its field strength, the specific patterned self-assembly can be reversibly induced only on the conductive areas. After the desired patterns were obtained, a DC offset (in the experiments, DC was set as 2V) with positive charge on the bottom surface would be applied and lasted for nearly ten seconds, as Fig 3.4(C) shows. The negatively charged colloidal particles self-assembly pattern was then permanently immobilized on the surface.

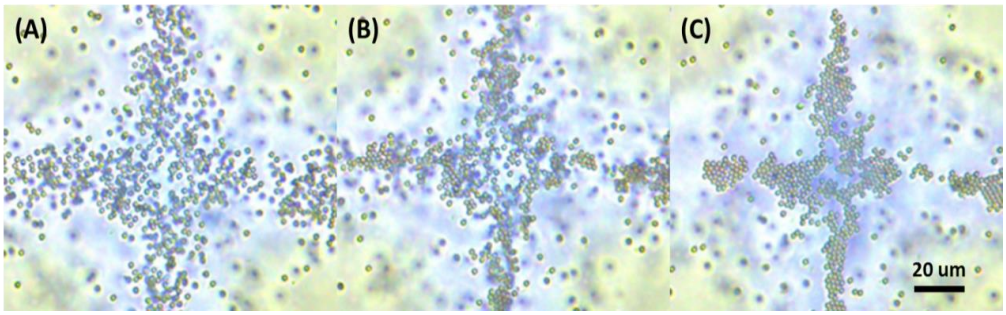

Figure 3.5: The formation of colloidal assembly with a crisscross pattern composed of 1.3 μm particles upon application of AEF with *500 Hz* and *2.5* x 10^4 *V / m*, with a time of *t* = (A) *0s*, (B) *5s*, (C) *10s*, respectively.

Figure 3.5 shows the time snapshots of a typical process of crisscross patterned colloidal assembly by combination of lithography technique with external electric field, with a time interval of five seconds. In the images, the

yellow areas are covered by a layer of photoresist dielectric film (a layer of impure gold with depth of 10~20 nm) while the rest white area is the non-treated ITO layer. The exposed ITO electrode have a cross pattern with a width of ~50 um. Before experiments, without AEF, the PS beads undergo randomly Brownian motion. Upon application of AEF with frequency f=500 Hz and field strength E_0=2.5 x 10^4 V/m, the PS beads were rapidly transported from the dielectric region towards the ITO conductive region. The PS beads aggregated on the exposed ITO surface and started to form clusters (Fig 3.5 B, t=5s). For a longer assembly time (Fig 3.5 C, t=10s), the clusters kept growing until they reached the favorable equilibrium state. The properties of equilibrium state were associated with many parameters, such as the beads concentration, the frequency, the field strength *etc.*

The reason why PS beads were transported to the conductive area upon electrical field could be explained in terms of the EHD flow, especially the EHD flow induced by the presence of the photoresist layer. According to studies of Nadel *et al.* (80), when AEF is applied, the presence of the dielectric regions will lead to the development of a steady long-range EHD flow with direction from the dielectric region towards the conductive region. After the beads aggregated on the ITO conductive area, the situation would be the same as the previous experiments carried out by Zhang *et al.* (25, 31, 52). Based on their experimental data, Liu made a hypothesis that it was the local EHD flow (which was caused by the presence of the colloidal particle) further approached the beads closer and enabled them to laterally assemble. The existence of the EHD flow induced by the presence of photoresist layer can be

verified because we clearly observed a macroscopic loop of the colloidal particles flow near the conductive/dielectric boundaries within the experimental cell. However, as for the hypothesis that it is the local EHD flow which serves as the driven force that overcomes the interparticle electrostatic repulsion and enables 2D colloidal aggregation, it is possible that there exists other long-range attraction between the particles which account for such assembly. This long-range attraction will be further discussed in chapter 4.

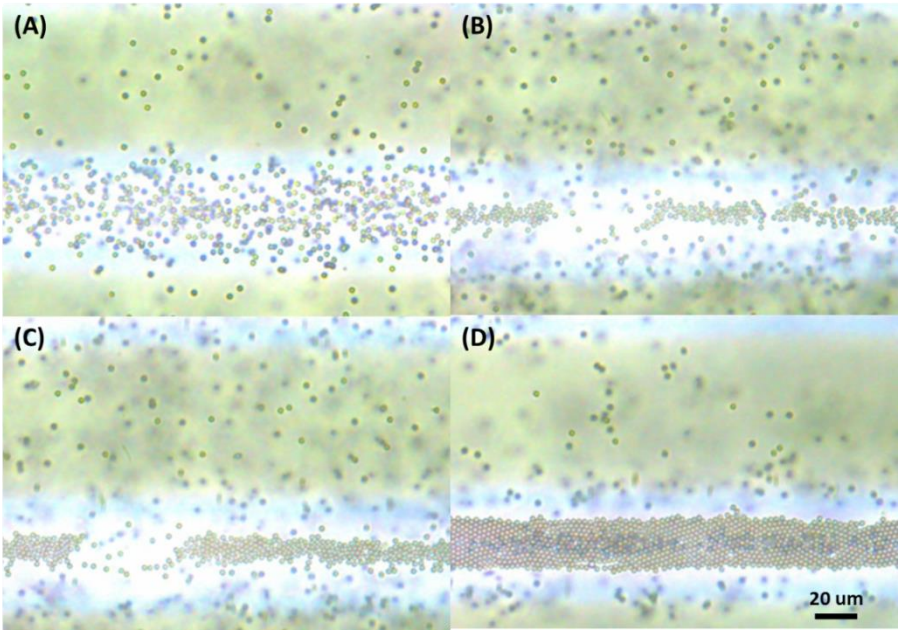

Figure 3.6: Microscopy images of the formation of a linear colloidal pattern composed of 1.3 μm PS particles upon the application of AEF with different field strength. (A) *500 Hz* and *0* x 10^4 *V/m*; (B) *500 Hz* and *1* x 10^4 *V/m*; (C) *500 Hz* and *2.5* x 10^4 *V/m*; (D) *500 Hz* and *4* x 10^4 *V/m*.

Similar as the method in section 3.2.1, the pattern geometries can also be varied in this method, thus colloidal assembly with various potentially useful shapes could be formed on the ITO electrode. Fig. 3.6 shows the microscopy images of the formation of a linear colloidal pattern. Compared with the dewetting method, this surface modification combined with electric field method can control the band width easily and reversibly by alternating the field strength. As figure 3.6 shows, larger field strength would induce larger band

width, when field strength not exceeding 4 x 10^4 V/m. When higher than 4 x 10^4 V/m field strength is applied, a disruptive macroscopic circulation flow would move so fast and prevent the particles from approaching to the conductive area. Even higher field strength will change the electrodes color from transparent to brown, indicating such ITO electrodes are burned out. In this situation, the cells are discarded.

In the experiments mentioned above, the dielectric photoresist film is a thin layer of impure gold, which was in fact still conductive but had a relatively larger resistance than ITO coating. To more precisely control the colloidal assembly pattern, we also applied the photoresist lithography with a layer of non-conductive adhesive, the result was very promising.

Before experiments, we designed mask plates with various geometries such as lines and squares, the light-lithography would be carried out following procedures below. A layer of non-conductive positive adhesive was coated on the ITO glass surface, after that this glass would be exposed to a UV light with the mask plate on its top. The UV light would dissolve the adhesive where they were not protected by the mask plate, the linear channels or crisscross channels of the conductive ITO surface would be unfurled. The width of the channels was mainly determined by the mask plate design, the exposure time and the UV strength would also have impact on it. Fig 3.7(A) and (C) shows the created 3μm channels with a linear and square well pattern, respectively. By applying a proper AEF on relatively diluted colloidal suspensions, perfect

self-assembly into our desired patterns can be realized, as Fig 3.7(B) and (D) shows.

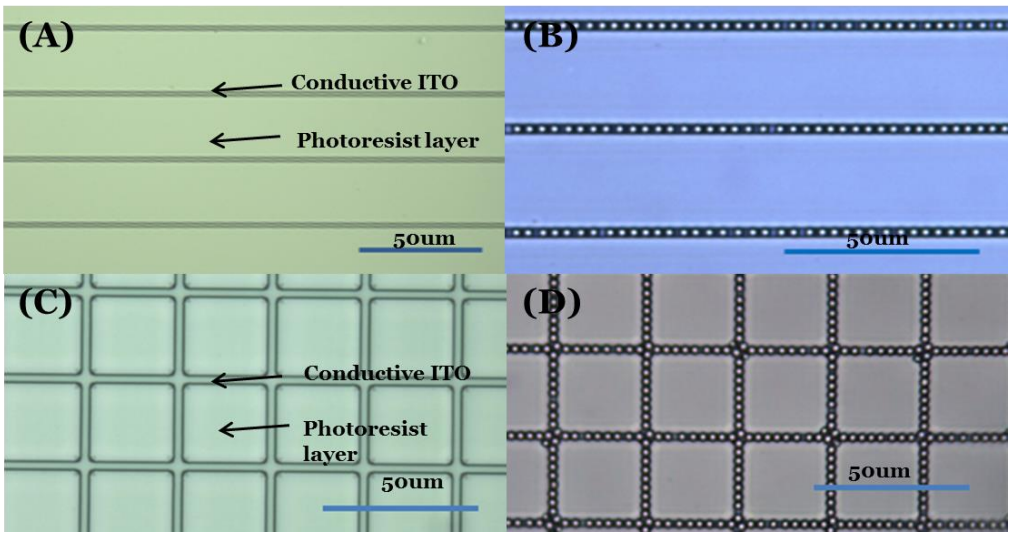

Figure 3.7: Microscopy images of (A) linear patterned dielectric photoresist layer; (B) 3 um beads formed linear pattern on template shown in (A); (C) square well patterned dielectric photoresist layer; (D) 3 um beads formed crisscross pattern on template shown in (C).

3.3 Conclusion

In this chapter we demonstrated two approaches for 2D colloidal patterning. One is based on de-wetting method along a copper grid, the other is by utilizing an AEF controlled colloidal assembly on the lithographically template electrodes. Both methods are simple and steady, especially, the second method displayed distinct advantages than the traditional ways in several aspects. First, it can successfully realize the patterning of colloidal assemblies with band width ranged from individual particle to several particles. Second, this approach is very rapidly, the assembly can be accomplished within seconds if AEF is applied with proper frequency and field strength. Finally, as it is already verified that the EHD flow due to the existence of the photoresist layer

aggregate the particles, and the origin of such EHD flow has nothing to do with the beads we chosen. It is believed that this method should also work for other particles or even polymers, disregard of the material and the diameter.

CHAPTER 4

Interactions between like-charge particles under AEF

4.1 Introduction

High quality crystals free of defects are required in many fields. So far, the understanding of crystallization is still far from being complete although crystallization has been studied intensively for more than one century. The main challenge in typical atomic system to study crystallization is that atoms are not only too small but also they move so fast for direct observations. As alternative approaches, colloidal experimental modelling was developed and attracted considerable attention in recent years. One reason the colloidal model can be substitute of atomic system is that colloidal particles in solutions can exhibit equilibrium phases and undergo phase transitions, being analogous to that of atomic system. Another reason is that both in colloidal and atomic systems, there are a variety of interactions between the atoms, molecules or colloids. Since the structural and other relevant properties of these systems depend strongly on the nature of the interactions between particles, complete understanding in the effective inter-particle interactions would be prerequisite. The interactions between particles and the interaction between particle and boundaries have been investigated intensively for many years, coming with

many theories and hypothesis describing them. Among the theories, one of the fundamental and widely accepted one is the traditional DLVO theory.

DLVO theory describes the overall interactions between pairs of colloidal particles. The overall interactions are the sum of attraction and repulsion, among them, the short-range van der Waals attraction and the long-range electrostatic repulsions occupy the most important position. Ever since the DLVO theory's establishment, lots of experiments have reached a good agreement with it. However, DLVO theory had come under attack in the last two decades. For example, in contrast to experience, like-charge polystyrene colloidal particles, under some particular confinements, can attract each other, and such attraction is confirmed to be long-range (16). This observation can't be predicted or explained by DLVO theory. The van der Waals force, which is also attractive for similar particles, should not be accounted for this unusual attraction because the van der Waals force is a short-range force. Besides, it can only contribute less than 0.01 K_bT to the interaction potential for the polystyrene microspheres immersed in water and separated by more than 100 nm (16). So far, no satisfactory theoretical explanations for this long-range attraction have proven convincing. There are still doubts about its origin. Further experimental and theoretical investigations of this surprising phenomenon could be very rewarding.

4.2 Review of like-charge attractions

Attraction between like-charge particles is one of the anomalistic phenomena in colloidal systems which arouse great interests in recent 20 years. Ito *et al.* used a confocal laser scanning microscope to count the numbers of negatively charged latex particles as a function of the distance from the negative surface of a cover glass, and found that the concentration of particles near the like charge cover (Z=5-40 um) became higher when the dispersion was deionized under density-matching conditions (9, 10). Later Tadashi continued Ito's research and found that the adsorption was promoted with increasing the number of surface charges on the particles or the plate surface ζ potential. However, this adsorption was hindered with increasing the added salt concentration and finally disappeared at 10^{-4} M or higher (17). Nevertheless, they also repeated similar experiments with different particle concentrations and confirmed that the condensation was not density dependent. The charge dependency of the adsorption indicated that the driving force was an electrostatic attractive interaction between the like-charged plates and particles, and such attraction was long range force (0.5-1 um).

Owing to the development of experimental techniques, such as digital video microscopy (DVM), it is possible for us to directly observe and quantify the phenomena occurring in colloidal suspensions with a force resolution of the order of 10^{-15} N. In assistance of DVM technique, precise measurement of colloidal pair potential can be achieved. Grier studied the interaction potential of a pair of colloids under different confinements (15). The potential was measured by capturing a pair of colloids first with optical tweezer, and then

recording the beads trajectories with DVM. They found that a pair of unconfined colloidal beads behaved purely repulsive, which was consistent of the DLVO theory. However, when the beads were confined between parallel negatively charged glass walls, the potential had a significant attraction component. They further confirmed that the attraction range increased with increasing of the particles diameter (18). Kepler and Fraden (19) repeated a series of similar experiments as Grier, they measured the relationship between the PS beads (with a diameter of d=1.27 um) separation and the pair potential. Their results showed a shallow potential minimum of approximately 0.2 k_bT at a sphere separation of 1.4d, which remained constant up to a sphere separation of 1.8d. After fitting the potential minimum position and depth for Hamaker constant and Debye screening length predicted by DLVO theory, they found the fitted Hamaker constants were always several orders of magnitude larger than theoretical calculations, in this way, they ruled out the probability that van der Waals accounted for the attraction potential.

4.3 Results

In our experiments, an alternating electric field was applied on the colloidal suspension for controlling colloidal self-assembly and for measuring the inter-particle potential under this particular condition,

Before measurements, several PS particles were fixed on the glass substrate serving as reference beads using the method in chapter 3, other particles were uniformly dispersed in the suspension. Upon application of AEF, those free particles would be transported from the disperse media to the glass substrate

by EHD flows, with the particle gathering degree tuned by changing the frequency. Liu *et al.* had proved that electric field frequency *f* determined the transduction efficiency of the particles from medium to electrode surface, resulting in the surface area/volume fraction being frequency dependent. With a high field strength and relatively low frequency, an attraction force would drive the PS beads to assemble into a nucleus or even 2D crystal structures. Liu *et al.* made a hypothesis it is the local EHD flow that accounted for the attractive interaction among colloidal spheres (81). Their studies mainly focused on nucleation or phase transition process, both of which were actually dynamic processes. For example, in a typical nucleation process, the competing effect between attraction and repulsion among inter-particles would result in some of the nuclei kept growing whereas some nuclei shrank. Thus, to analyze the interactions between colloidal spheres, creating an equilibrium state for the colloidal suspension would be prerequisite.

4.3.1 Equilibrium state

The equilibrium state refers to the state where the nuclei size remained nearly constant during the whole experiment time, meanwhile the beads on the nuclei boundary kept exchanging with the beads from solution. As the equilibrium state has associated with many parameters, such as the beads concentration, ionic strength of the solution, AEF frequency, AEF strength *etc*, it is natural to believe that all of these parameters would affect the inter-particle interactions.

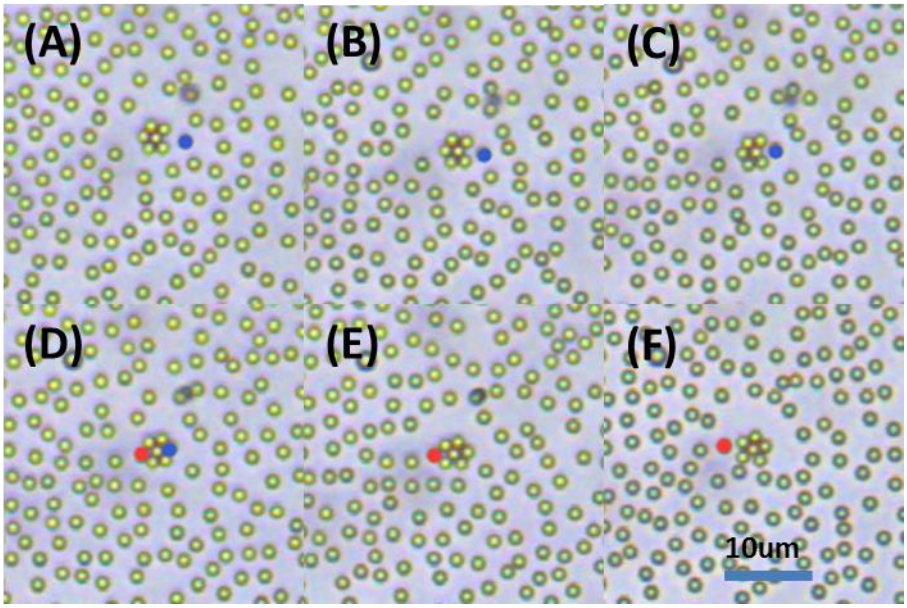

Figure 4.1: Example of equilibrium state with AEF of 120 Hz and 2.5 x 10^4 V/m. With a time interval of t=0.5s. (A) 0t; (B) 1t; (C) 2t; (D) 3t; (E) 4t; (F) 5t. Blue and red dot indicates a bead incorporating and leaving into the cluster, respectively.

After trial, we succeeded to obtain an equilibrium state by providing an alternating electric field with proper frequency and field strength ($f=120$ *Hz* and $E_0=2.5 \times 10^4$ *V/m*). As can be seen from Fig 4.1, a stationary reference 1.3μm bead was fixed at the center of the image (in reality, this bead was fixed near the edge of the experiment cell). Around the reference bead there was a loosely packed beads cluster composed of five beads. When a new bead from the solution (indicated as blue dot) approached closer and eventually incorporated into the cluster, another old bead (indicated as red dot) would be repelled from the cluster, leaving the cluster beads number remained constant.

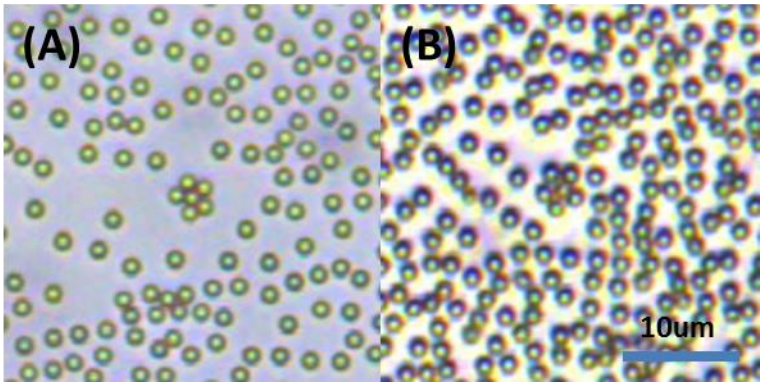

Figure 4.2: Microscopy images showing Req varies with beads concentration, where same AEF of *120 Hz* and *2.5 x 10^4 V/m* is applied. (A) Original beads concentration *Φ=0.004%*; (B) Original beads concentration *Φ=0.01%.*

The rest of the colloidal suspension (excluding the reference bead and surrounding cluster) was also in equilibrium state. This can be further confirmed by the fact that the center-to-center distance R_{eq} between the neighboring particles were nearly constant (in Fig.4.1, R_{eq}*~2d, d* is the diameter of the particles). The value of R_{eq} was related to many factors. For example, higher sphere concentration would significantly decrease the R_{eq} (as shown in Figure 4.2). Our further investigation of R_{eq} as a function of the sphere concentration elucidated that there exist a critical concentration, beyond which condensed suspension would never reach an equilibrium state. Instead, the colloidal particles would rapidly aggregate, regardless of the adjustment of the other parameters (data not shown).

Except for the sphere concentration, electric field strength and frequency are also the main factors that determine R_{eq}. The dependency of the equilibrium distance on frequency and field strength is non-linear and the mechanism is complicated. This has already been reported and verified by Zhang and his colleagues (82), which results are presented in fig. 4.3.

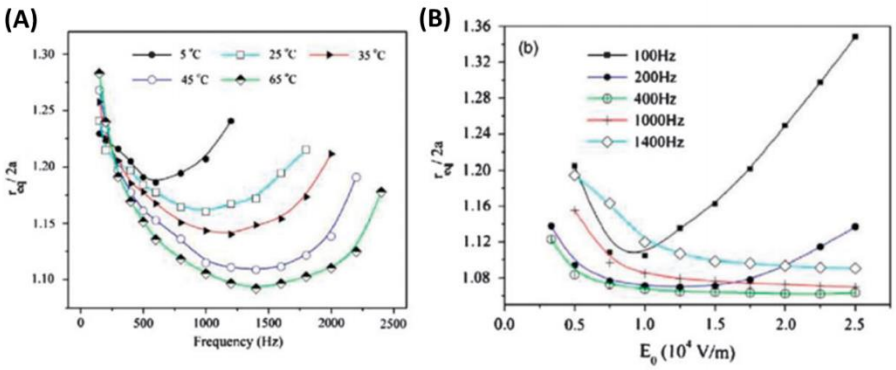

Figure 4.3: (A) Frequency dependence of the equilibrium distance with different temperature at same field strength $E_0=1.5 \times 10^4$ *V/m*, where a is the bead radius. (B) $R_{eq}/2a$ as a function of the field strength E_0 at different frequencies with a temperature of 25 ℃. (This figure is adapted with permission from ref.(83))

From their study, it is worth attention that temperature can also change the R_{eq}. However, as all of our experiments were carried out in condition where the temperature was fixed at 25 ℃, the temperature influence would be neglected during our analysis process.

4.3.2 Influence of EHD flow Asymmetry

The experiment method and analysis process were described in chapter 2. The PS beads, with a diameter *d=1.3 um* or *2 um* and mass density $\rho=1.05\ g/cm^3$, are negatively charged with a ζ-potential of -54 mV in the *0.05 mM* sodium chloride ionic solution. The colloidal suspension, with an initial volume fraction of *Φ~0.004%*, is sandwiched and sealed between two parallel conductive ITO glasses. Upon AEF application, a continuous electric field induced flow transported the beads closer to the glass substrate. This fluid flow gave rise to a condensed density on the electrode surface and hence allowed the colloidal spheres to reach an equilibrium state. Properties of this equilibrium

state were determined by field strength and frequency of the given AEF. After the equilibrium state had lasted for 30 minutes, a digital camera video recording the positions of each particle (both the stationary and moving particles) was taken for further analysis. The sphere center's location can be measured from the videos snapshot images frame by frame, thus the radial distribution function was obtained.

We calculated the radial distribution function around the same stationary bead in fig. 4.1, which was fixed near the edge of the experiment cell. The result is shown in Fig. 4.4.

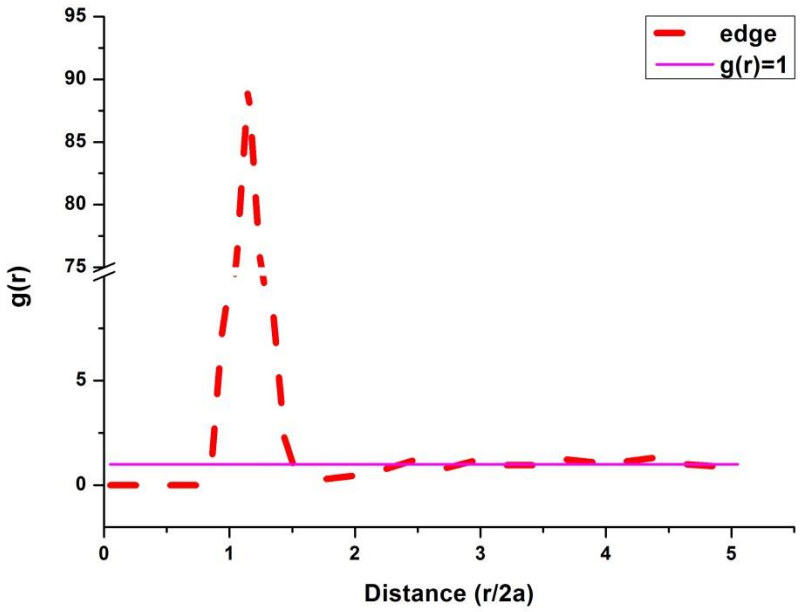

Figure 4.4: The g(r) as a function of normalized sphere separation around a stationary sphere near the edge of the experiment cell. $E_0=2.5 \times 10^4$ *V/m* and *f=120 Hz*. a is the radius of sphere. The dashed lines of g(r)=1 and U=0 were drawn for visual guidance

We clearly observed only one high peak in g(r) curve, this is consistent with the fact that only one layer of nearest beads was around the reference bead as

shown in fig.4.1. After the first peak, g(r) decreased rapidly as the distance increased. A shallow minimum of g(r) at the separation $R \approx 4a$ was developed. This shallow minimum proved the existence of repulsive force which repelled beads approaching closer. Finally the g(r) curve would oscillate around a guidance line of g(r)=1 when the beads separation exceeding $R \approx 6a$, indicating the interactions outside this range became negligible.

The interaction potential is a sum of attractive potential and repulsive potential. Based on the experiment data, we confirmed the existence of an attractive force between like-charge spheres, though the mechanism still remained unknown. Kepler and Fraden (19) believed van der Waals (VDW) force accounted for this attractive force. However, VDW attraction should be neglected because the measured value of this attraction is orders of magnitude larger than the theoretical VDW attraction. Other researchers hypothesized this attraction arose from the electrohydrodynamic (EHD) flow (72). A general accepted mechanism for EHD flow is presented below: Small ions in electrolyte solution build up an electric double layer adjacent to the electrode surfaces. This electric double layer is disrupted by the presence of charged colloidal particles, leading to spatially varying free charges. A lateral electric field is induced by the charged colloidal caused distortion of the applied field. The EHD flow is set up by the interaction between this lateral electric field and free charges. Although the EHD flow-produced convective loops would carry the particles toward electrode surface, the possibility that Stokes force caused by the EHD flow served as the only driven attractive force for particle assembly has been minimized. It is worth to be mentioned that due to the

existence of the cell spacer walls, the EHD flow-produced loops near the cell edge would differ significantly. Our experimental observation suggested that the flow velocity in the center of the cell was relatively smaller than that near the edge.

As the EHD flow played an important role in triggering the colloidal assembly and this flow differed in different cell areas, we measured the RDF around a fixed bead located in different cell areas, respectively. Fig.4.5 plotted g(r) curves around a bead at the center and in the edge, respectively. We surprisingly found that the two curve's characteristic features differed in many aspects. For the bead located in the center, on one hand the height decreased. Meanwhile, position of the first peak (PFP) shifted to larger separation, both indicating the beads were loosely packed in the center. From the EHD velocity the Stokes force can be determined,

$$F_s = 6\pi\eta a u(f) \tag{4.1}$$

Where η is the viscosity of the solution, a is the radius of the moving particle and $u(f)$ is the tangential EHD velocity along the electrode surface which is a function of the field frequency. The EHD velocity near the edge was higher than that at the center, thus the induced Stokes force would also be larger. The larger Stokes force, which was regarded as the external force rather than the real inter-particle interaction, would pack the cluster of beads closer. As for the disappearance of the repulsion component, it indicated that EHD flow may have influence on the spheres interaction. This behavior so far has not been well understood.

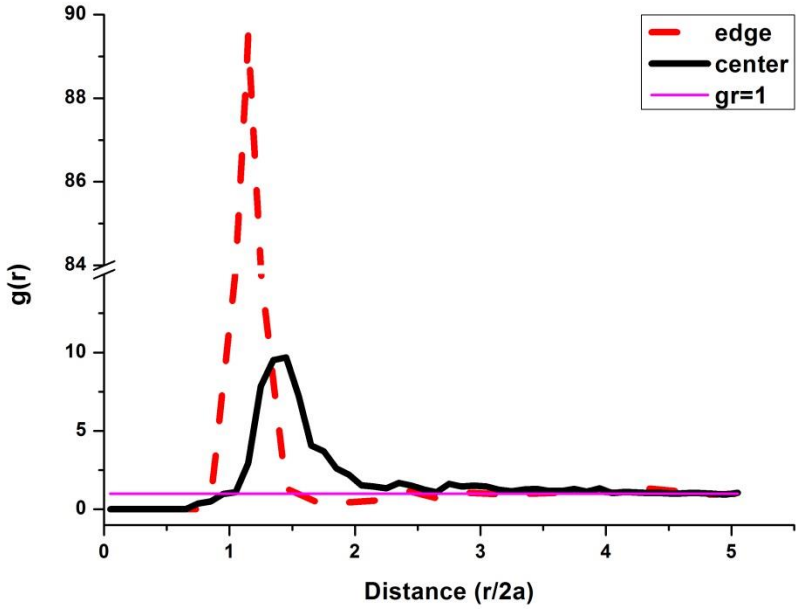

Figure 4.5: The radial distribution function of 1.3um PS beads located at different cell areas. The black and blue curve represents the bead in the center and at the edge, respectively. E_0=2.5 x 10^4 V/m and f=120 Hz.

To study the effective interaction pair potential between spheres and to rule out the effect of the EHD flow, measurements in the following were all carried out in the same small area (200x150 um^2) where the EHD flow influence should be uniform.

4.3.3 Influence of particle density on effective pair interaction potential

Several experiments have been reported in previous literatures (16, 18, 19), where the interaction potential between a pair of spheres in an extremely diluted colloidal suspension was measured. The new aspect of my project, in contrast, is that we measured the g(r) and interaction potential in a much concentrated colloidal suspension.

The direct inversion method from g(r) to potential u(r) following Boltzmann distribution

$$g(r) = e^{-\beta u(r)} \tag{4.2}$$

is based on an assumption that the pairwise interaction is the only parameter that determines the beads' position. For a sufficient diluted suspension, this relationship between g(r) and u(r) has proven accurate. However, as for concentrated suspension, except for the stationary reference bead, other neighboring spheres would also associate with each other. In this situation, the calculated potential through direct g(r) inversion should take the many-body correlation into consideration.

When no electrical field was applied, the PS particles were randomly distributed in colloidal suspension. The sphere density in different layers of the experiment cell was the same, which was determined by the initial volume fraction of colloidal suspension added into the cell. Upon application of electrical field, the field induced flow would transport the colloidal spheres from solution toward the glass surface, leading to a sphere density gradient along the vertical directions. Since we only measured the interaction potential between those beads on the glass substrate, the sphere density in the following sections would only refer to the local density on the surface.

The local sphere density on the electrode surface n^* is defined by $n^* = n \times \pi a^2$, where $n=N/S$ is the average concentration of particles observed in one frame of area $S=\pi x(10a)^2$, a is the radius of the sphere and N is the counted number of particles in area S per frame. In order to get good statistics for g(r), several

stochastic frames during the whole experiment process were analyzed. In Fig.4.6 the radial distribution functions of three samples with different local sphere density n^* were shown. We observed in this figure that the height of the first peak of g(r) increased as n^* was increasing, with PFP remained nearly constant. From the figure some apparently unphysical results of g(r) > 0 for separation $r/2a < 1$ were shown. These unphysical errors may arouse from the thermal drift of the sample stage during the long measurement time and should be suppressed by applying a clamp on the stage. Another possible explanation was that the degree of freedom for the moving beads was not strictly confined in two dimension, the errors may be denoted by some ill-focused spheres.

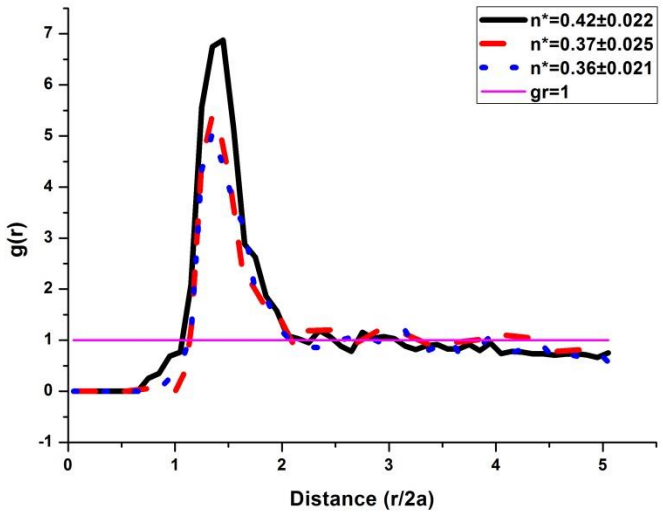

Figure 4.6: The sphere density dependence of g(r). The black, red and blue curve represents a regime of concentrations where $n^*=0.42\pm0.022$, $n^*=0.37\pm0.025$ and $n^*=0.36\pm0.021$, respectively. $E_0=2.5 \times 10^4$ *V/m* and $f=120$ *Hz*.

After years of intensive discussion, no widely accepted agreement had been reached about the many-body effect on inter-particle interactions. Kepler and Fraden (19) firstly compared the radial distribution function g(r) for two different cells with the same low ionic strength but with different sphere

densities. They found that even for an order of magnitude difference in the sphere density, the height of g(r) and the PFP remained essentially the same. Their computer simulations further corroborate the suggestion that the g(r) peak is not the result of many-body correlations, but rather arises exclusively from the real attractive potential. In other words, within that density range, the many-body effect can be neglected.

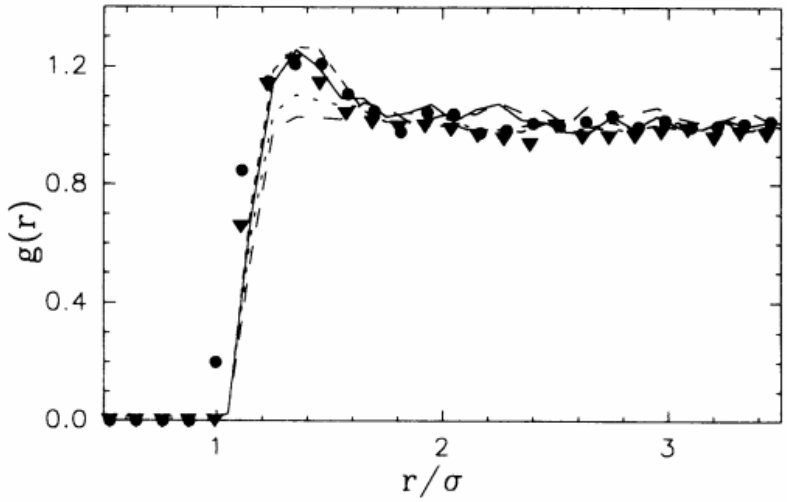

Figure 4.7: Experimental and simulation results for g(r) with different spheres densities obtained by Kepler and Fraden: (solid circle) 5.8 x 10^{-3} and (triangle) 52 x 10^{-3} um^{-2}; (solid line) 5.8 x 10^{-3} and (dashed line) 52 x 10^{-3} um^{-2}. (This figure is adapted from ref. (19))

However, Tinoco *et al.* (20) repeated a series of similar experiments in a much concentrated regime and found that density dependence of the g(r) became physically important if only the spheres density is beyond some critical values.

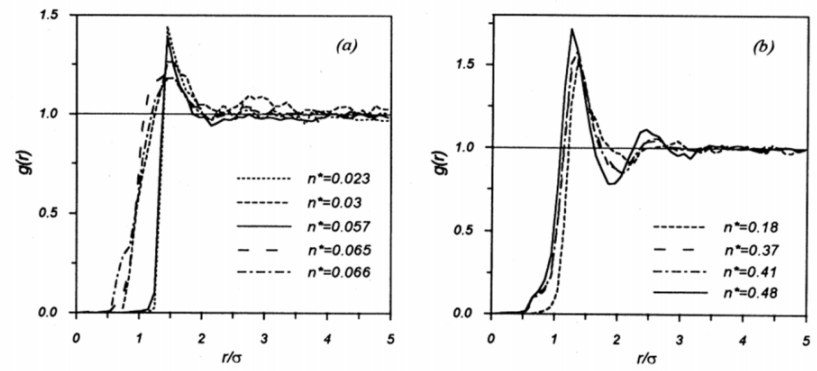

Figure 4.8: g(r) of colloidal suspensions obtained by Tinoco *et al*. (a) g(r) in the dilute regime; (b) g(r) in the concentrated regime but colloidal suspension is still in liquid phase. (This figure is adapted from ref. (20))

Although Tinoco brought out opposite conclusions against Kepler and Fraden, they still reached a highly consistent conclusion that the many-body correlation should not account for the attractive force. The most likely many body effect may be a static structure of the colloidal clusters.

For our two-dimensional system, as the radial distribution function g(r) has been calculated, the effective pair potential u(r) can be converted using the Ornstein-Zernike relation together with an appropriate closure relation (20).

$$h(r) = c(r) + n^* \int d^2 r' c(r') h(|r - r'|), \tag{4.3}$$

In Eq.(4.3), *h(r) = g(r) -1* is the total correlation function and c(r) is the direct correlation function. Although this equation could not relate g(r) to pair potential u(r) on each point, u(r) might still be inverted from the experimental g(r) values. On taking Fourier-Bessel transform on both sides of Eq.(4.3), we obtain an algebraic relation between *C(k)* and *H(k):*

$$C(k) = \frac{H(k)}{1 + n^* H(k)}, \tag{4.4}$$

Then the "experimental" direct correlation function c(r) can be calculated by transformation *C(k)* back to the real space. The effective pair potential u(r) could now be obtained using a closure relation of the mean spherical approximation (MSA). The MSA is defined in terms of the pair distribution function and direct correlation function by:

$$\begin{aligned} g(r) &= 0, r < 2a \\ c(r) &= -\beta u(r), r > 2a \end{aligned} \tag{4.5}$$

Previously Tinoco *et al.* (20) had already proved that for dilute systems, both Eq. (4.2) and Eq. (4.3) would lead to essentially the same pair potentials. As for higher concentrations, although Eq. (4.2) is no longer valid, the pair potential u(r) obtained by OZ equation together with the MSA closure relation still shared the main physical characteristics of the actual effective inter-particle interactions. The most concentrated samples in Tinoco's systems was $n^* = 0.48$, in other words, within that wide range of concentrations, the MSA results were in good quantitative agreements with the effective pair potentials.

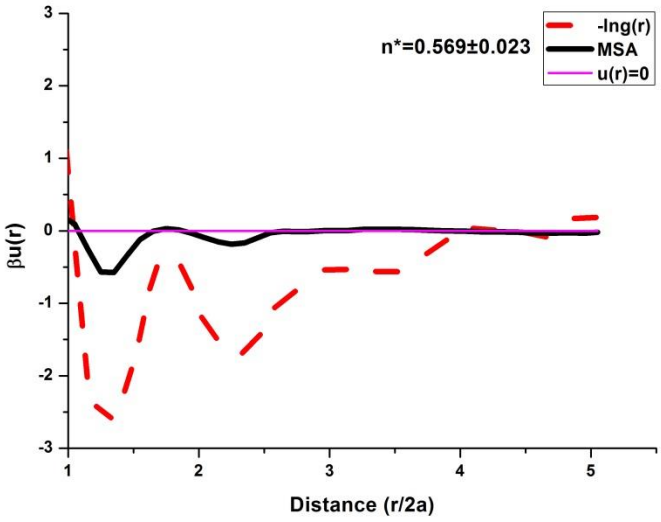

Figure 4.9: Comparison of the results obtained from the OZ equation together with the closer relation MSA and the results from Boltzmann Distribution inversion, for the most concentrated sample.

In Fig.4.9, we show results for $\beta u(r)$, corresponding to the most concentrated samples studied in our work ($n^* = 0.569$). We can see that for this even higher concentration (compared with 0.48), in spite of some quantitative differences between the results based on Eq.(4.2) and Eq.(4.3), the qualitatively similar physical characteristics were still kept. Compared with the Boltzmann Distribution inversion, which is only valid in dilute systems, this effective pair

potential derived method based on Ornstein-Zernike equation exhibited better accuracy in the whole range of concentrations considered in our work. In the following analysis, only the MSA pair potential u(r) results would be presented and discussed.

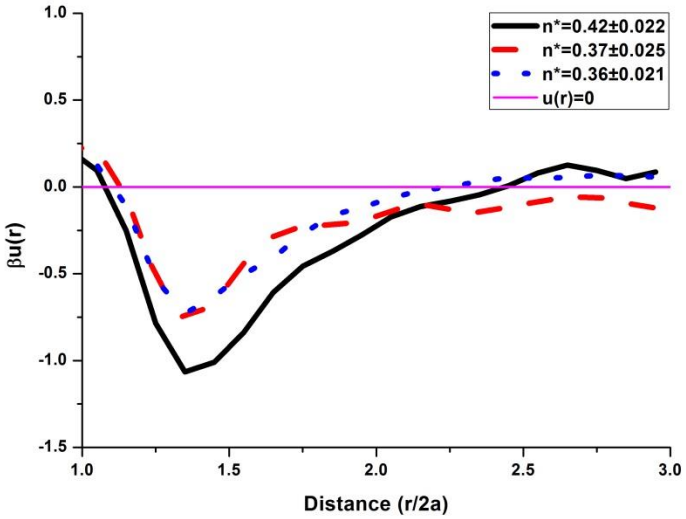

Figure 4.10: The sphere density dependence of MSA method obtained pair potential u(r). The black, red and blue curve represents a regime of concentrations where $n^*=0.42\pm0.022$, $n^*=0.37\pm0.025$ and $n^*=0.36\pm0.021$, respectively. $E_0=2.5$ x 10^4 *V/m* and *f=120 Hz*.

Following the FB transform procedure, we calculated the MSA method based pair potential u(r) for the beads in Fig.4.6, which results were shown in Fig.4.10. As can be seen, sphere density would influence the pair potential between particles, in a tendency that higher density accompany with larger attractions.

4.3.4 Influence of sphere diameter on effective pair interaction potential

As the colloidal particles carried negative charges on its surface, the most likely repulsive potential would be electrostatic repulsion. Electrostatic repulsion is proportional to the surface charges. Based on assumption that surface charge density is the same for PS spheres, the sphere diameter would influence the overall charges, thus change the interactions.

To study the sphere diameter dependence of the inter-particle interactions, we did a series of experiments on PS particles with different diameters (1um, 1.3 um, 2 um and 3 um, respectively). The 1 um beads moved too fast to be tracked by our digital camera. The 3 um beads in electrolyte solution were very steady, to acquire statistically sufficient data would take a relatively long time. Thus the ideal beads were 1.3 um and 2 um.

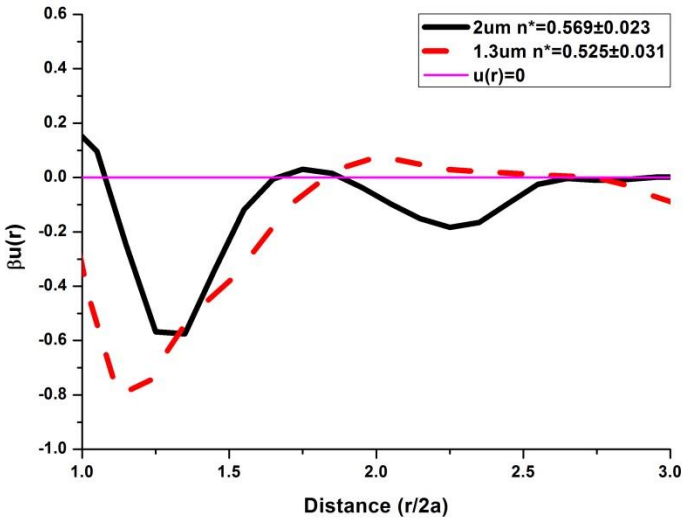

Figure 4.11: The sphere diameter dependence on pair potential as a function of normalized sphere separation. The black and blue curve represents the bead with a diameter of 2 um and 1.3 um, respectively. E_0=2.5 x 10^4 V/m and f=60 Hz.

In Fig.4.11 we compared the pair potential around beads with different diameters. These two curves share a similar characteristic feature: a well-defined first minimum peak, despite of not with the same height. The increased depth of the first minimum peak of u(r) showed that the 1.3 um bead had stronger ability to attract beads. The normalized PFP shifted toward higher values as the diameter increased, also suggesting a larger repulsive force was between the 2 um beads.

According to classical DLVO theory, in Debye–Hückel approximation, the repulsive potential takes the form of a screened Coulomb potential (also called as Yukawa potential),

$$u(r) = \frac{Z_{eff}^2 e^2}{\varepsilon\varepsilon_0 (1+\kappa a)^2} \frac{\exp[-\kappa(r-2a)]}{r} \tag{4.6}$$

Where $Z_{eff}e$ is the effective charge on the colloidal particle that can be related to the ζ potential by

$$Z_{eff} e = 4\pi\varepsilon_0 \varepsilon a(1+\kappa a)\zeta \tag{4.7}$$

κ is the inverse of the Debye screening length. It is obvious that the effective particle's charge for 2um is larger than that of 1.3 um, this can qualitatively explain why the repulsion for 2um bead is larger than 1.3 um.

An effective range of interaction potential can be defined as the separation at which the pair potential is equal to 1/e of the maximum value. Attractive component of the potential between like-charge spheres were both clearly observed for different size spheres. In addition, this attraction's effective range was measured to be as large as 1.5d. Compared with the repulsive potential,

whose effective range was 0.03d (not accurate, just approximation), we can conclude that the attraction between like-charge spheres is long-range. Although the effective range was measured from the sum of the attractive and repulsive which may had large variations with the pure individual component, the conclusion that the repulsion is short-range while attraction is long-range is still convincing.

4.3.5 Influence of cluster dimension on effective pair interaction potential

In section 4.3.4, we have concluded that the spheres with larger diameter had larger repulsive interactions. To further test such diameter influence, we did similar experiments except that the stationary bead was replaced by a sphere cluster.

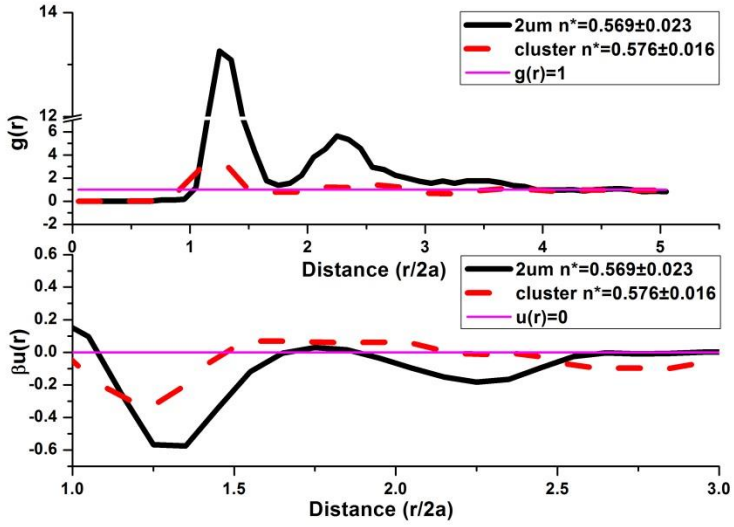

Figure 4.12: The dimension dependence of g(r) and effective pair potential u(r). The black and red curve represents a 2 um sphere and a sphere cluster, respectively. E_0=2.5 x 10^4 V/m and f=60Hz.

In Fig.4.12, we compared the g(r) and effective pair potential u(r) between double-layered cluster and 2 um diameter bead. The characteristic features for the cluster curve had displayed greatly different compared with that for single bead, although on condition of nearly the same density. If we regarded the cluster as an "effective" sphere with large diameter, then the development of the very shallow minimum peak in g(r) curve further convinced the previous conclusion that the repulsive force was proportional to the sphere diameters. In addition, the effective range for the attractive potential had increased from 1.06d to 1.62d for the single bead and clusters, respectively. Though the width and height of the first peak both shrank for the cluster, the larger effective attraction force range still revealed that the pair attraction is also increasing, similar like repulsion, the increasing of repulsive potential overwhelmed that for attraction.

4.3.6 Influence of AEF frequency on effective pair interaction potential.

Alternating electric field was applied on colloidal suspension and triggered the self-assembly process. To understand the physics mechanism, numerous experimental and theoretical works had been carried out by several groups.

As the average equilibrium separation R_{eq} depends on the balance of attractive and repulsive force, studying R_{eq} would be a useful tool to understand the properties of the forces. *Liu et al.* counted on the electrostatic repulsion and EHD induced Stokes force for the dominant balance force (81). Though the role of electrostatic repulsion is widely accepted because the colloidal particles are highly charged in suspension, thus electrostatic repulsion will prevent

aggregation. The form of the attractive force, which could be divided into a variety of other force such as van der Waals attraction, dipole-dipole interactions *etc*, is still under debate. The van der Waals attraction should be neglected for being short-range and non-sufficient. As for the dipole-dipole interactions, it varies as r^{-4} and scales as

$$f_{dip-dip} \approx 3\pi\varepsilon_0\varepsilon a^6 E_0^2 / r^4 \tag{4.8}$$

Researchers fit the electrostatic repulsion with the attractions above at the experimentally obtained equilibrium separation, and found that the calculated dipole-dipole interaction is at least an order of magnitude smaller (81). In contrast, the calculated values for the EHD flow-induced Stokes force agreed closely with the experimental data within some frequency range. However, EHD force failed to explain the de-aggregation phenomenon when frequency exceeded a cut-off value. After balancing the electrostatic repulsion with the sum of stokes force and the dipole-dipole interaction, the fitting curve still doesn't make big difference. The differences between the fitting and experimental data revealed that there should be at least another attractive force which can give some additional support to resist the repulsions. We are not to deny the importance of the EHD flow induced attractive force during the self-assembly process. On the contrary, we highly evaluated the EHD flow-induced attractions. They serve as an external force to overcome the electrostatic repulsions and thus decrease the particle-particle separation. Then only within a short separation, the inter-particle interaction would be an additional force to strengthen the colloidal aggregation. Consequently, the role of the long-range attraction should be stressed.

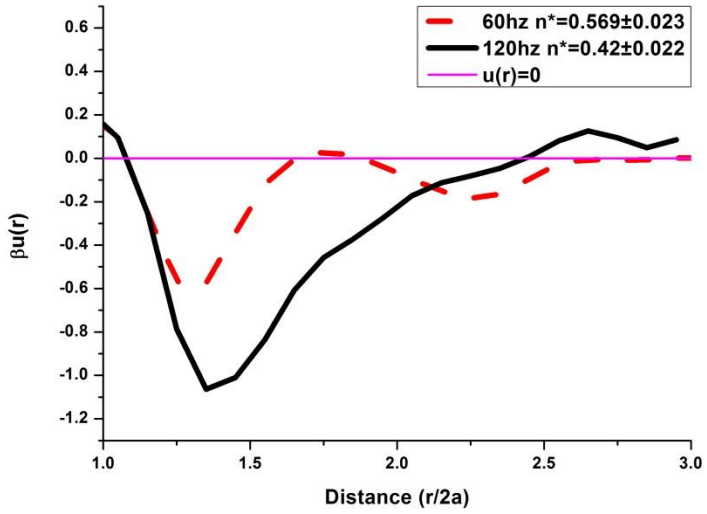

Figure 4.13: The frequency dependence of effective pair potential u(r). The black and red curve represents AEF frequency *f=120 Hz* and *f=60 Hz*, respectively. E_0=*2.5* x 10^4 *V/m*.

It is verified in our experiments that the AEF frequency had great impact on the inter-particles potential. We applied electric field with different frequency on a small area (200 x 150 micrometers^2) in the cells with other parameters (including the initial volume fraction for PS spheres) the same, then we measured the radial distribution function and the inverted pair potential u(r) was as shown in Fig.4.13. The curves representing *f=60 Hz* and *f=120 Hz* displayed totally different features. It is interesting that we found the local beads density had increased from 0.42 to 0.569 when we decrease the frequency. As discussed in section 4.3.3, upon electric field application, the EHD flow would bring floating beads from solution approaching to the surface, hence increasing the local surface sphere density. This sphere enrichment on the electrode surface is consistent with the studies of Zhang and Liu (52), where they have proved that the changes in frequency will not change the static structure of the 2D colloidal crystal, but such change in frequency would lead

to changes of the transport of the particles to the electrode surface and in the area/volume fraction of the colloidal particles.

We hypothesized that the AEF frequency can influence the interaction potential, not in a direct way but by changing the surface sphere density and the redistribution of the counter-ions, especially when the local sphere density exceeding the critical value.

4.3.7 Influence of AEF field strength on effective pair interaction potential

It is shown that field frequency may influence the effective interaction potential, maybe not through a direct way but by greatly increasing the local sphere density and distorting the counter-ions distribution. As both the EHD flow velocity and the dipole-dipole interactions are functions of the electric field strength, in this section, we are going to study the effective pair potential under different field strength based on same AEF frequency.

It is difficult to obtain ideal equilibrium state for colloidal suspension with AEF frequency fixed at $f=120Hz$. So far we have successfully studied the pair potential under electric field strength at $E_0=2.5 \times 10^4$ V/m, $E_0=4 \times 10^4$ V/m and $E_0=5 \times 10^4$ V/m (no aggregation was observed for AEF strength smaller than 2×10^4 V/m, while AEF strength> 5×10^4 V/m would burn the ITO glass cell). We compared the averaged g(r) and pair potential u(r) curve with different field strength but nearly same local sphere density. The results are shown in Fig. 4.14.

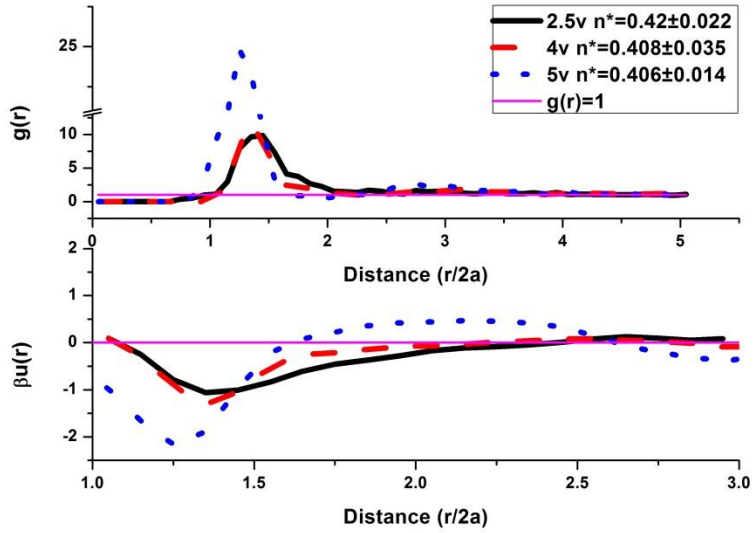

Figure 4.14: The AEF field strength dependence of g(r) and effective pair potential u(r). The black, red and blue curve represents AEF field strength E_0=2.5 x 10^4 V/m, E_0=4 x 10^4 V/m and E_0=5 x 10^4 V/m, respectively. Frequency is fixed, f=120 Hz.

In all series of experiments, the initial volume fraction for PS spheres is the same, which is Φ=0.004%. Previously we observed a significant increase in the surface sphere density when we decrease the AEF frequency from 120 Hz to 60 Hz. However, when changing the field strength, from E_0=2.5 x 10^4 V/m to E_0=5x 10^4 V/m, the surface sphere density remained nearly the same. Based on essentially the same sphere density, density influence can be omitted. The differences in the g(r) and effective potential u(r) revealed that the inter-particle interaction has been altered when changing the field strength.

For the E_0=5 x 10^4 V/m curve, we clearly found that the first peak has a larger width and height, its position was smaller. Moreover, a secondary peak was also developed. All of these phenomena indicated that the attractive potential increased with increasing the field strength. In addition, the energy barrier in

interaction potential shown in $E_0=5$ x 10^4 V/m revealed that the repulsive potential is also increasing with increasing the strength.

4.4 Discussion & Conclusion

There are several analogies between the charge-stabilized colloidal suspension system in our experiment and a fluid metal. Colloidal suspensions are composed of large and highly charged particles, *i.e.* macroions (colloids) which are suspended in a structureless medium and surrounded by a screening atmosphere of microions (counterions). Fluid metal, on the other hand, essentially consists of highly charged metal core ions plus the screening charge electrons cloud in which the metal ions are embedded. Accordingly, similar theoretical concepts should be applied in both the theory of metals and that of the colloidal suspensions. Considering the interaction in fluid metal is associating with the ions, it inspired us that the interactions in colloidal systems may also be results of the ions interactions. Here, we proposed a mechanism to explain the origin of that anomalous long-range attraction observed in our work. Nonlinearity maybe an explanation because of the apparently breakdown of linear superposition (pairwise colloidal sphere repel but groups cohere). As the colloidal spheres dispersed in electrolyte ionic solutions, a more reasonable mechanism may be the fluctuation in the counterions distribution (in our case, counterions are the sodium simple-ions). The counterions distribution around an isolated pair of spheres mediates pure repulsive interactions. Confining walls (in our system, AEF will push the colloidal spheres close to the surface of the electrode glass, which serves as an confining wall), neighboring spheres and alternating electric field, however, redistribute the counterions so as to

mediate the long-range attractions. In our proposed mechanism, the repulsive interactions between spheres are mainly the screened Coulomb repulsion,

$$u_{rep}(r) = \frac{\varepsilon_0 \varepsilon (4\pi a \zeta)^2 \varepsilon_0 \varepsilon \exp[-\kappa(r-2a)]}{r} \tag{4.9}$$

As for the attractive interaction between spheres, we regarded it to be the interaction between PS beads and the redistributed counterions (which is embedded into the gaps among neighbor spheres). This attraction adopted the form of coulomb interaction,

$$u_{att}(r) = \frac{(4\pi\varepsilon_0\varepsilon)^2 a(1+\kappa a)\zeta Q(E, f, \phi)}{r - r'(E, f, \phi)} \tag{4.10}$$

Where a is the radius of the colloidal particles, ζ is the zeta potential which can be measured directly. $Q(E,f,\Phi)$ and $r'(E,f,\Phi)$ is the effective charge of the counterions and the effective separation between the counterions and the reference sphere (in maximum approximation, the redistributed counterions are regarded as a point charge), both of Q_{eff} and r'_{eff} is a function of the field strength, field frequency and the sphere density. In this way, the effect of such parameters can be taken into consideration. Based on this assumption, we calculated the net potential which is the sum of the screened Coulomb repulsive and counterions attractive potential, and found that the simulation result agrees well with our experimental data as shown in Figure 4.15.

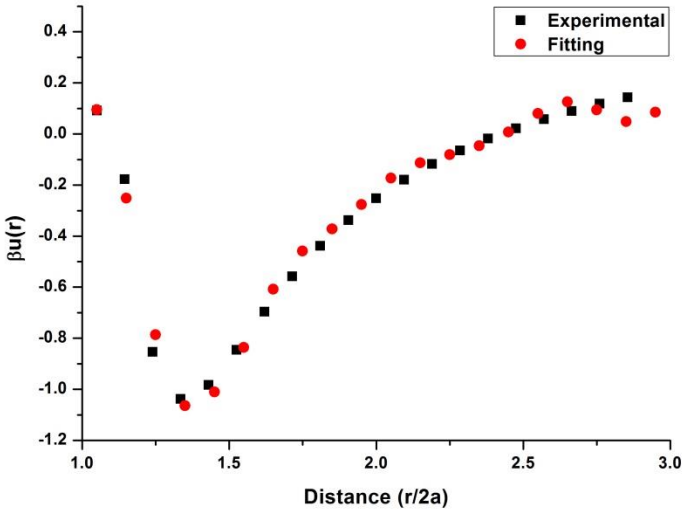

Figure 4.15: Effective interaction potential between colloidal spheres under AEF. Experimental data agrees well with the prediction based on the counterion mechanism.

Till now this mechanism is still far from quantitative expression, but knowing the ingredients necessary for the like-charge colloidal attractions to occur and convincing the parameters responsible for the like-charge colloidal attractions property is a big step towards understanding their origin and predicting their ramifications. Our method based on the two-dimensional version of the OZ equation provides an alternative general procedure that allows for the determination of the effective pair potential. Our experimental system of studying the interaction under AEF also offers insights into how particular systems behave under particular external field, in the future we can extend this method to other systems such as DEF, magnetic field *etc.*

So far, we qualitatively studied the interactions between PS spheres under AEF. The inter-particle interactions are sum of the attractive force and repulsion force. (1). It has been proved that the attractive force is a long-range force

(with an effective force range varies from 1d to 3d) and ruled out the probability of its origin as van der Waals force and dipole-dipole interactions. The inter-particle interactions under AEF can be changed by several parameters, such as the sphere diameter, dimension, sphere density, AEF field strength and frequency. (2). Larger diameter and dimension would increase the repulsion and attraction simultaneously, the increase of repulsion dominated attraction. (3). Sphere density can greatly change the static structures of the sphere clusters, thus changing the measured radial distribution g(r). It would also have impact on the inter-particles pair interaction: the concentrated regimes exhibit larger repulsion and attraction at the same time. Compared with g(r), pair potential is less sensitive to the sphere density. In other words, the many body effect on pair potential is only significant when local density exceeds some critical value. (4). The AEF frequency can adjust the pair potential in an indirect way, maybe it is realized through changing the surface sphere density and through re-distribution of the counter-ions to interfere the sphere's electric double layers. (5). In addition, the AEF field strength can also affect the interaction potential, in a manner of larger field strength increase the repulsion and attraction, and the increase of repulsive overwhelm the attraction.

CHAPTER 5

A mechanosensing mechanism centered on α-catenin in cell-cell adhesion

5.1 Introduction

5.1.1 Cellular Mechanics

In advanced organisms, it still remain unknown how specialized cells of 10-40 um in diameter assemble and organize into tissues with specific biological functions, nor do we know how cells recognize their spatial positions within such multicellular systems. Extracellular matrices and the neighbouring cells constitute the main physical signals that individual cell can sense. On the basis of extensive analyses, such physical signals are force and geometry signals at a nano-to-micrometer level. Therefore, the mechanical properties of the cell as well as the cell's ability to interpret and respond to signals play pivotal roles in the establishment and maintenance of tissue shape and the proper biological functions.

Cellular mechanics involves three main steps, mechanosensing, mechanotransduction and mechanoresponse: force-induced changes in protein conformation and geometry-dependent interactions (mechanosensing) are locally transduced into biochemical signals that activate various mechanosen-

sitive signaling pathways (mechanotransduction) that might interact to produce controlled functional responses (mechanoresponse). In general, cellular mechanics can be divided into two parts. First is the mechanical response of the cell's force-bearing structures, the other is a biochemical signaling response, which is associated with most force-induced phenotypic changes.

Cell-cell, cell-matrix and flow forces are all sensed in different contexts during the mechanosensing process. The forces that are developed by the cells themselves on matrix or cellular contacts are also important. In order to transduce the mechanical cues into cellular signals (mainly biological signals) and thus directing the cellular response, there seems to have mechanisms, maybe at molecular level, for cells to evaluate the right amount of the force and make corresponding adjustments. The molecules, which exhibit such ability, are referred as the mechnosensing proteins. After years of intensive experiments, a large family of mechanosensing proteins has been identified in cells with diverse mechanisms.

The transduction of local mechanostimuli into biochemical signals occurs through several signaling pathways: Ion channels, tyrosine phosphorylation, receptors-ligand bonds (catch bond) *etc.* have all been found during the force transduction process (110-112). The downstream signals can then involve complex signaling pathways to produce corresponding responses.

5.1.2 Mechanosensing process

It has been reported that upon a range of mechanical forces, a diverse set of structural motifs could change conformation and potentially serve mechanosensory functions. These include the opening of ion channels, receptor-ligand bond formation, and the force-induced exposure of cryptic peptide sequences.

Open ion channels. Ion channels are present in the membrane of nearly all cells and many intracellular organelles. They are named as ion channels because the rate of ion transport through this channel is very high. Generally speaking, ion channels are not sensitive to mechanostimuli. However, there are some particular ion channels, in which their one opening responds to stress in the lipid bilayer, whereas the other physically connects to cytoskeleton and/or the extracellular matrix to transmit force to the ion channel. Such ion channels are mechanosensitive and can serve as the mechanosensory.

Receptor-ligand bond formation. The link between intracellular cytoskeleton and the extracellular matrix is realized by protein networks. This physical connection is mediated by weak non-covalent bonds and the weakest part will fail first if the protein networks are under tension. For normal slip bonds, as force tilts the energy landscape, the bond lifetimes are progressively shortened. In fact, non-covalent bonds will fail under any level of tensile stress if held for sufficient time periods. Thus, lifetime under tension can be a useful tool to evaluate the strength of the bond. Receptor-ligand bond (or catch bond), is also a type of non-covalent bond whose bond lifetime increases with tensile

force applied on it. At present, only two types of receptor-ligand complex has been confirmed to be able to switch from the short-lived to long-lived state in presence of external force. These are FimH (113, 114), P- and potentially L-selectins (115-117). It is still under debate whether other adhesion proteins, such as integrins or proteins that anchor the cytoskeleton to integrins, can form these catch bonds under the influence of force, or if they simply rely on the formation of multiple linked bonds.

Force-induced exposure of cryptic peptide sequences. Most proteins consist of tandem-repeated sequences. In single molecular levels, the applied force helps proteins to overcome energy barriers, coming with the breakage of several force-bearing hydrogen bonds that used to maintain the original structures. In protein levels, stretching of the protein will induce the protein to change to a partially unfolding conformation, which will expose the cryptic peptide sequences that are otherwise hidden in its folded conformation.

All these could be the mechanism for mechanosensing and early mechanotransduction. Another mechanism, which is similar as the force-induced exposure of cryptic peptide sequence, is that force-induced stretching of a protein may unfurl binding sites for other proteins. This mechanism has been postulated for a long time but never been demonstrated experimentally. Until recently, del Rio *et al.* showed that mechanical stretching of a single cytoplasmic protein can activate binding of other molecules (118). They used single molecular assays to investigate the effect of force on the interaction between talin and vinculin and found that force caused stretching of talin

would expose cryptic binding sites for vinculin. The most significant difference between this mechanism and the previous is that it firstly proved that the mechanosensing process may not be performed at individual protein levels. Instead, a group of functional proteins may collaborate to govern the complex mechanosensing process. Such force-induced protein stretching and binding may be a more general mechanism for mechanosensing and transduction process.

Except for talin, there are many other multidomain mechanosensing proteins which may also play important roles. Among them, a-catenin, enriched in cadherin-based adherens junctions, is an ideal candidate. Similar as talin, structural data revealed that a-catenin also buried a binding site for vinculin but such binding was inhibited due to the fact that a-catenin adopted a closed conformation. By analogy, it is hypothesized that a-catenin and vinculin may also act as mechanotransducer in the signaling pathway that converts mechanical load on cadherin adhesions into a cue for junction strengthening.

5.1.3 Review of cadherin-based adherens junctions

In multicellular organisms, different types of specialized cells organize together to form tissues and carry out biological functions. To maintain the tissue structural integrity and proper function, robust and selective cell to cell and cell to environment adhesions are required.

Cell-cell adhesion is the binding place where cell is interacting with the surface of other cells. It could serve different roles such as supporting the structures, transducing the signals, initiating the immune response and recognizing cells. Cell-cell adhesion only is not sufficient for tissues integrity. It also requires the cell-matrix adhesion to function properly. In epithelium tissues, cells are surrounded by a fibrous protein network called extra-cellular matrix (ECM). The ECM can act as the scaffold for the tissues and is involved in a variety of cellular process, thus also very important.

In cells, the cell-cell adhesions can be divided into three main categories, the tight junctions, desmosomes and the cadherin-based adherens junctions (AJs). The tight junctions (also known as zonula junctions) are found in endothelial and epithelial cells which can form a tight seal by serving as the diffusion barrier. Desmosomes (also known as macula adherens) are localized spot-like adhesions randomly distributed on the lateral sides of plasma membranes of stratified squamous epithelial cells which help to resist the shearing forces (89). As for the cadherin-based adherens junction, it is the most well-studied cell-cell adhesions so far which is believed to play the most crucial role in maintaining the specific architecture of tissues and regulating the cell response to external stimulus. Cadherins exert important physiology functions *in vivo*, e.g. interaction between cadherins and other intraculluar proteins can regulate the cell-cell adhesions; during morphogenesis, cadherin-based adhesions can control the cell sorting (90). Because of their important functions, any dysregulation of cadherin function would result in many diseases such as breast cancer(91), tumor progression(92) and neuropsychiatric disorders (93).

The cadherins super-family comprises over 100 types of cadherins and can be classified into five distinct families (summarized in Table 5.1): classical Type I cadherins, classical Type II cadherins, desmosomal cadherins, proto-cadherins and some ungrouped cadherins. As the table shows, though all the cadherins have some similarities in the domain features, individual cadherin sub-family are highly specialized functioned and only can be found in specific tissues or sub-cellular structures.

Subfamilies	Functions	Examples
Classical Type I	Form adherens junctions	E-cadherin, N-cadherin
Classical Type II	Maintain specialized tissues	Cadherin 7, cadherin 8
Desmosomal	Form desmosomes	Desmoglein, Desmocol-lin
Proto-cadherins	Develop neuron	Pcdhα, Pcdhβ
Ungrouped cadherins	Remain to known	CDH9, CDH10

Table 5.1: Subfamily of Cadherins

Among them, classical Type I and Type II cadherins are the most well studied cadherins family for both their roles in both of the structural and physiological function in cell-cell adhesions. Classical Type I and Type II cadherins share a similar molecular structure, which consists of three main domains. As shown in fig. 5.1, the cytoplasmic domain (also known as intracellular domain), the transmembrane region and the extracellular domain (EC).

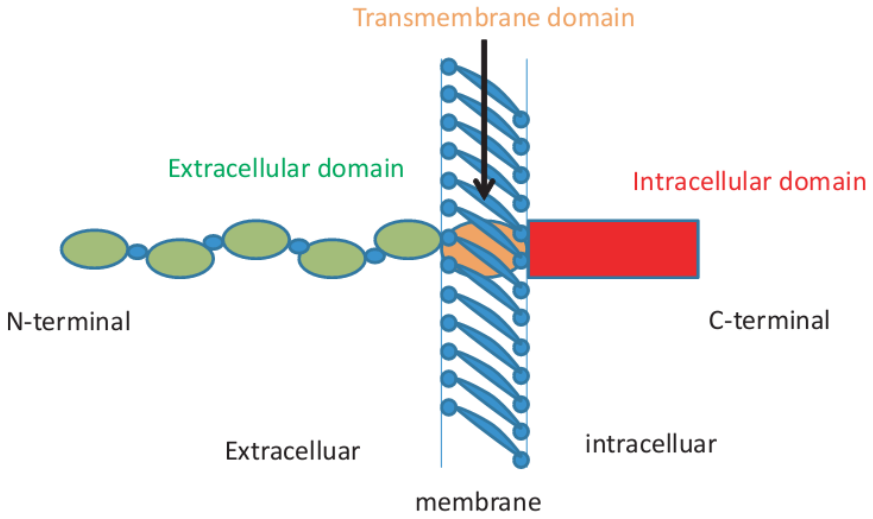

Figure 5.1: Schematic structure of classical cadherins. Classical cadherins consist of three main domains: the extracellular domain, transmembrane region and intracellular domain, which is represented with green, blue and red, respectively.

The extracellular domain comprises five tandem repeats, named extracellular cadherin domains, herein labeled as EC1 to EC5 from N-terminal to C-terminal. Each EC domain consists of nearly 110 amino acids which form seven β-strands and are organized into two β-sheets. Between each EC domains, there are bridges formed by three calcium ions. The extracellular domain plays an important role in AJs because the cadherins can only homophilically interact with proteins of the same type of the extracellular domain. The interaction can happen between two adjacent cells (trans interactions) or two cadherin molecules from the same cell (cis interactions), both of which are verified to be important to stabilize the cell-cell adhesions. The transmembrane domain is the shortest region and consists of only 15 amino acids. The mutant study has confirmed the significance of the transmembrane domain in cadherin-based adherens junctions, the cadherin mutant which changed a certain point on the transmembrane domain would reduce the cadherins self-

assemble and greatly weaken the cadherin-based cell adhesions in cell aggregation experiments.

The intracelluar domain of classical Type I and II cadherins is the most highly conserved domain and contains nearly 150 amino acids. This domain interacts with multiple-protein complex at cadherin-based AJs, as shown in Fig. 5.2.

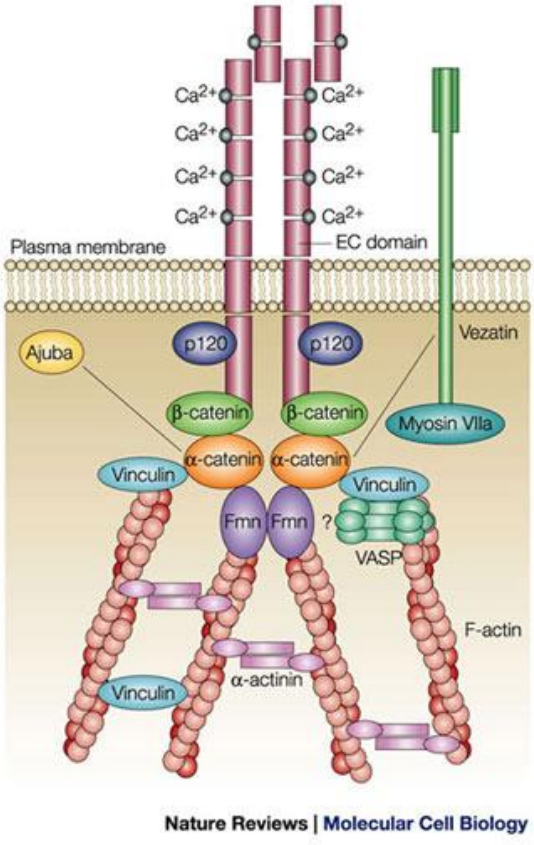

Figure 5.2: Schematic of the multiple protein complex at cadherin-based Adhesion Junctions. (Figure adapted from ref.(94)).

The tail of intracellular domain of cadherins binds directly to β-catenin, which in turn can bind to the N terminals of α-catenin. In addition, p120 binds to juxtamembrane domain of the intracellular domain of cadherin, this binding could modulate the turnover of cadherins in AJs. In the C terminus of α-catenin, there are binding sites for actin. The binding between the complex and

F-actin filaments help to anchor the complex in the AJs. Though earlier studies suggested that the α-catenin serves as a direct linker between the cadherin/β-catenin/α-catenin complex and the F-actin cytoskeleton, recent studies have minimized this possibility and the interaction may be a manner of indirect, direct or both. In the central part of α-catenin, it is found that they can recruit other actin-interacting partner proteins, such as ZO-1 (95, 96), afadin (97), formin-1 (98) and vinculin (94, 95, 99, 100).

5.1.4 Review of mechanosensing related proteins in cell-cell adhesions

As mentioned in last section, α-catenin might serve as a linker that connects the cadherin/β-catenin/α-catenin complex to filamentous actin in a direct, indirect or both ways. In addition, several F-actin binding proteins such as vinculin have been shown potentially bind to α-catenin and localize to cell-cell adhesions. The roles of these proteins in cell-cell adhesions are poorly understood, but they might provide additional support to the complex anchoring on F-actin, especially when the cell-cell contacts are under particular mechanical forces. In this section, two key components of the mechanosensing proteins, vinculin and α-catenin, are reviewed.

Similar as α-catenin, vinculin is also a cytoplasmic protein enriched both in cell-cell and cell-matrix adhesions. Structural data suggests that both vinculin and α-catenin are highly compacted globular proteins comprises of several homologous segments. As fig. 5.3 indicated, vinculin is composed of a series of helical bundles that form five distinct domains, designated D1-D5 (101, 102). D1, D2 and D3 all contain two four-helix bundles, D4 is a single four-

helix bundle, and D5 is a single five-helix bundle. Between D4 and D5, there is a proline-rich linker. As for α-catenin, it shares a great similarity with vinculin, which is consisting of only four domains while the D2 is absent. In particularly, D1 domain (the N terminus) contains the β-catenin binding sites and a-catenin homodimerization sites; as a result, the homodimerization is inhibited when D1 associates with β-catenin. The sequence of α-catenin D3 has not been fully structurally characterized, but it is believed the association with actin-binding partners is happened in D3a. D3b and D4 together are defined as the middle or modulation domain because deletion of this domain will weaken the cell-cell adhesions. The C terminus of vinculin and α-catenin in D5 both contains the binding sites for actin. Besides, α-catenin bears an extra extension which is also required for actin binding.

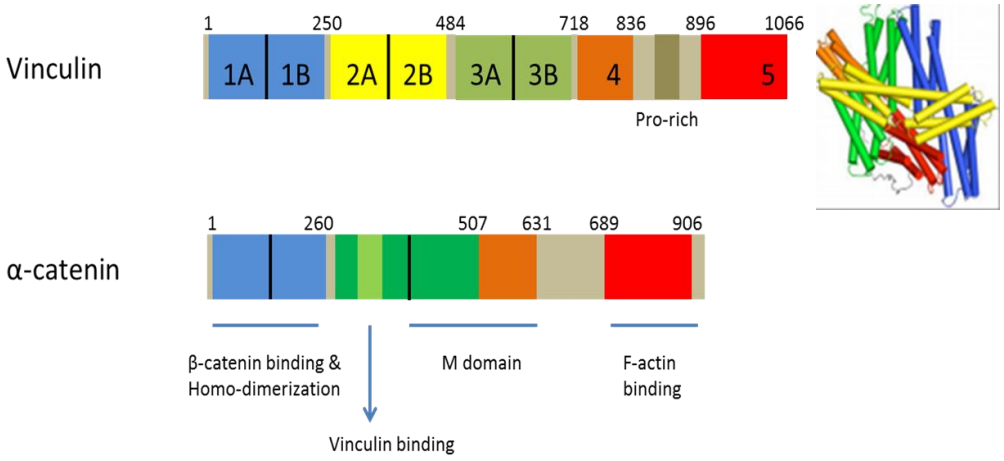

Figure 5.3: Primary structures of α-catenin and vinculin

Though in vinculin D5 (the “tail”) there buries a binding site for actin, vinculin in isolation only presents weak affinity to F-actin. This is due to the fact that vinculin in isolation adopted an auto-inhibited, closed conformation in which the D2 forms a stabilizing bridge which locks the D1 and D3 domains and such formed D1-D4 vinculin “head” would extensively interact with the

actin binding domain D5 (103). The binding between vinculin and F-actin can only be activated by relaxation of the head to tail dissociation. The conformation change from closed to open is force dependent, especially the dragging force by linking one end of vinculin to talin while the other end binding to F-actin simultaneously. This mechanism of force-induced vinculin activation is important for the understanding of the establishment of the mechanical associations between actin cytoskeleton and the adherens junctions.

Considering the D2 is absent in a-catenin, a-catenin can bind F-actin constitutively. Biochemical and structural data suggests that in α-catenin central domain there buried a vinculin binding domain (VBD) (100, 103). Further study indicates that α-catenin also adopt an auto-inhibitory conformation whereby the VBD is associating with the M domain, thus preventing the direct accessibility of the vinculin (104).

It has been hypothesized that α-catenin serves as the mechanosensor and mechanotransducer in signaling pathway which converts the mechanical load on cell-cell adhesions into the strengthening of the cadherin complex/F-actin linkage (105). However, till now there is no direct evidence in support of this hypothesis that the force-dependent unfurling can expose the VBD and can activate the binding of α-catenin to vinculin. To investigate the role of α-catenin in mechanosensing process, we used single molecular technologies to obtain direct experimental evidence to prove that physiological range force can regulate α-catenin conformation and trigger the binding to vinculin. The specific objectives of this research were to:

- study force response of a-catenin, especially the characteristic unfolding
- investigate the critical force that triggers the conformation change to activate the vinculin binding
- verify the location of vinculin binding site by introducing deletion mutants
- investigate the number of vinculin binding sites per a-catenin by counting the binding events

5.2 Methods & Materials

In this section, experimental methods including sample preparation, instrumentation and data analysis method will be introduced. We mainly measured the mechanical unfolding of α-catenin and the force-induced α-catenin binding to vinculin. To investigate the mechanical properties of α-catenin, Atomic Force Microscopy (AFM) and magnetic tweezers have been performed; as for the observation of the interaction between α-catenin and vinculin, it is realized through combination of magnetic tweezer and Total Internal Reflection Fluorescent microscopy (TIRFm).

5.2.1 Protein expression

Protein was obtained quantitatively through cloning the PCR product of the mouse αE-catenin central domain (residues from 275 to 735) into the dicistronic pDW363 vectors, co-expressing the *E-coli* biotin holoenzyme synthetase (Bir A). A 6xHis coding sequence followed by a stop code was added in the C terminus of the protein sequences. The expressed protein with

Biotin-α-catenin-6xHis construct is designated as WT αC. In order to make results more convincing, several α-catenin mutants were also designed and expressed in a similar way. One negative control is the so called Deletion mutant (Dmod), it keeps the entire VBD while most part of the modulation domain has been cut off. The positive control is a 3x WT trimer which contains three repeats of the WT α-catenin. Full length vinculin was abandoned, instead, only the vinculin head Vd (residues 1-258) was expressed for the experiments.

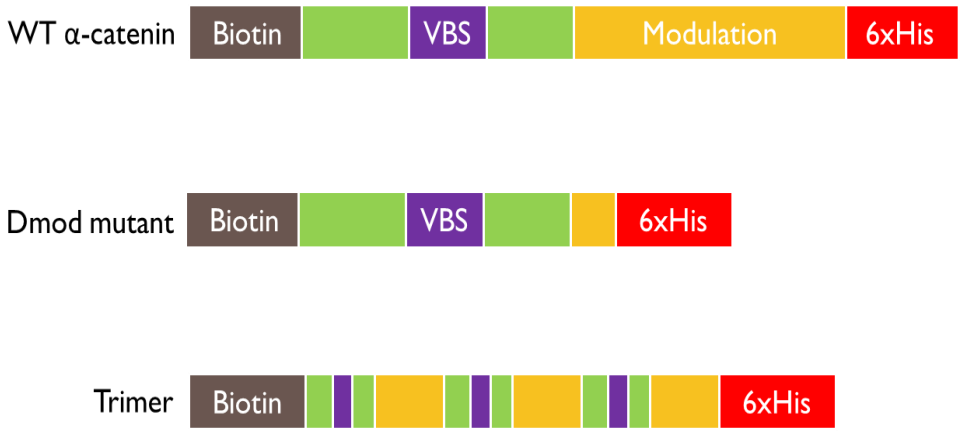

Figure 5.4: Schematic structure of the WT α-catenin and the mutants.

5.2.2 Atomic Force Microscopy

Since its invention in 1986, AFM has been widely used in science fields such as to measure the roughness of a sample surface at a high spatial resolution, to evaluate the interaction between a specific atom and its neighboring atoms, and to distinguish the cancer cells with normal cells based on the stiffness. In our experiments, AFM was chosen to measure the unfolding properties of α-catenin because of its several significant advantages. First, it can provide sub nanometer spatial resolution and pico-newton force resolution. Second, the

sample preparation is relatively easy, we just need to fix the proteins on the substrate and then the non-specific binding between the AFM cantilever tip and the protein would be formed spontaneously. Finally, compared with other single molecular level techniques, the AFM is of very high yielding. AFM can perform thousands of force-extensions measurements quickly under every experimental condition. This feature is very important to acquire a statistically convincing data.

A laser beam incident on the back of a cantilever and then reflected to a detector. When a force between the cantilever tip and the sample is detected, it will lead to a deflection of the cantilever according to Hooke's law. Therefore, by recording the reflected spot position on the detector, the force applied on the sample can be inverted.

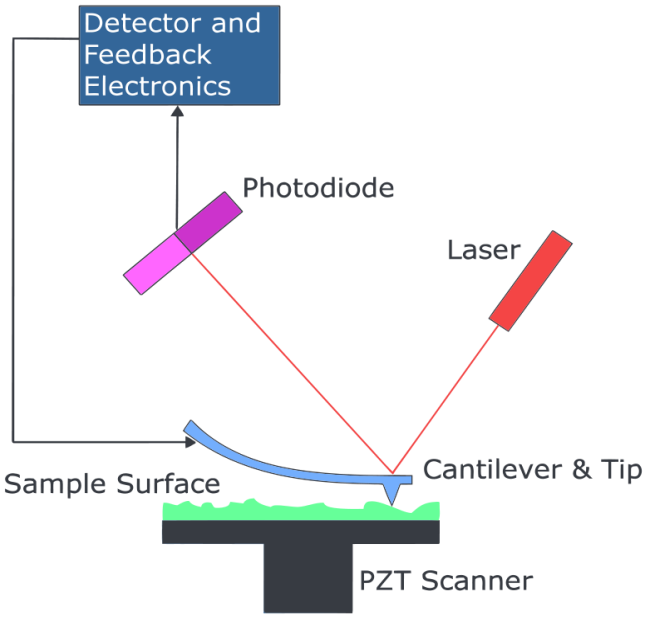

Figure 5.5: Diagram of the Atomic Force Microscopy. The detector is usually a photodiode detector. The position of the sample stage can be precisely controlled by using a PZT scanner.

In AFM, the cantilever can be approximately regarded as a spring with a specific spring constant. For different cantilevers, the spring constant is calibrated before each series of experiments following the standard thermal noise method (106). In our experiments, measured spring constant of the cantilevers varies from 5pN/nm to 20pN/nm.

The α-catenin was previously immobilized on a NTA-Ni^{2+} functionalized coverslip by specific binding. During the experiments, the AFM cantilever was manipulated to approach towards the slides surface to search for proteins, and then the tip would contact the slides with a pushing force of 1pN. Occasionally non-specific binding between the cantilever tip and the α-catenin can be formed. Afterwards the cantilever was withdrawn with a different constant pulling velocity to unfold the linked α-catenin. This cycle of approach-contact-withdrawn was repeated systematically on different areas of the glass surface where α-catenins were randomly distributed. In average, according to our given protein concentration (50ug/ml), 5-10% of all cycles exhibited characteristic force-extension curves associate with the unfolding of α-catenin. We also prepared a control group. Same experiments were done on a glass without any α-catenin on it, less than 1% of all curves had exhibited signals related to protein unfolding.

In AFM stretching experiments, the AFM is usually operated in the constant velocity pulling mode and the force-extension curve is obtained to study the characteristic features for different proteins. A typical protein unfolding force-extension curve is shown in fig. 5.6.

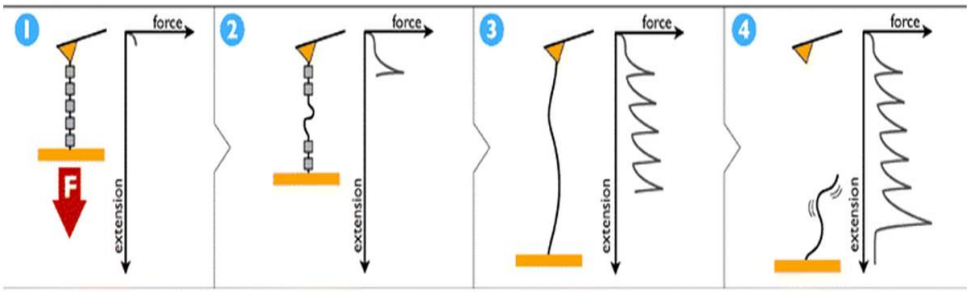

Figure 5.6: Illustration of the unfolding of a multi-domain protein and classical force-extension curve under AFM. (1) The protein is pulled with constant velocity mode. (2) The increasing force unfolds one protein domain and a suddenly drop in the pulling force occurs. (3) Force drops are repeated for each domain unfolding, resulting in a typical saw-tooth patterned force-extension curve. (4) Continued increasing force finally detaches the protein from the tip.

After the force-extension curve obtained by direct measurement, the increase in extension, Δz can be inverted into the increase of the protein contour length, ΔL. The relationship between Δz and ΔL is illustrated in Worm-Like-Chain (WLC) theory (107) and the WLC formula is given by:

$$F = \frac{k_B T}{p}\left[\frac{1}{4}(1-\frac{z}{L})^{-2} - \frac{1}{4} + \frac{z}{L}\right] \tag{5.1}$$

Where F is the protein stretching force, p is the persistence length of a polymer, z is the end-to-end protein extension which was directly measured in the experiments. L, the protein contour length, is the length of the protein molecule in fully stretched state. Generally speaking, p characterizes the local binding stiffness of a flexible polymer and ranges from 0.1 to 1 nm for proteins, in our experiment for α-catenin, the p was set as 0.3 nm.

$$F = \frac{k_B T}{p}\left[\frac{1}{4}(1-\frac{z}{L})^{-2} - \frac{1}{4} + \frac{z}{L}\right]$$

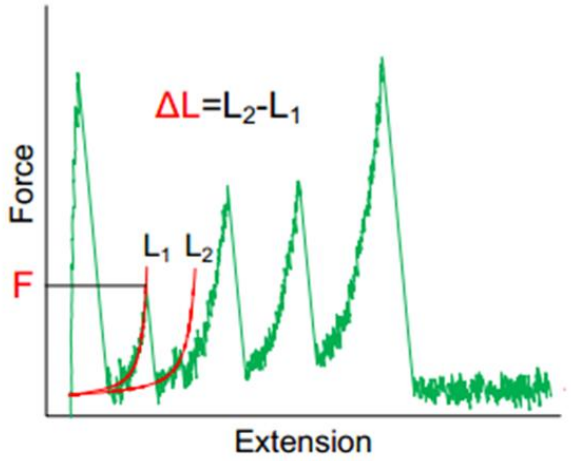

Figure 5.7: WLC fitting of unfolding force-extension curve. The saw-tooth pattern force-extension curves (green) can be fit to WLC curves (red) with adjustable persistence length and contour length. The unfolding contour length change ΔL is the difference between contour length of two adjacent force peaks. The corresponding unfolding force F is the force of the prior peak.

By fitting the WLC formula to two successive saw-tooth patterned force-extension curve peaks, the respective contour lengths, L_1 and L_2, can be fitted. Then the changes in the contour length can be calculated simply by $\Delta L = L_1 - L_2$.

5.2.3 Magnetic tweezers plus TIRFm

Magnetic tweezer is another powerful single molecular level instrument for the manipulation and characterization of biomolecules or polymers. It is also widely used in fields of measuring the tensile strength generated by molecules. Compared with AFM, magnetic tweezer has a primary advantage that it can apply a stable pico-newton level force and maintain it for tens of minutes. On the contrast, AFM can only maintain less than one minute and the force fluctuation is much stronger.

The principle of magnetic tweezer is simple. One end of the target protein was immobilized on the glass surface through specific binding. In our experiment, it was the binding between 6x histag and Ni-NTA. The other end of the protein, which was labeled by biotin, also through specific binding, was linked to a fluorescent magnetic bead with streptavidin on its surface as functional group. In magnetic tweezers, a magnet, either permanent magnet or electrical magnet, was used to apply force on the magnet bead. With a symmetric magnet, the magnitude of force applied on a magnetic bead depends on both the magnet-bead distance and the magnetic contents in the bead. The magnetic contents had a large variation from one bead to others. As a consequence, a large variation in force was induced. In the single molecule manipulation studies of the unfolding of protein, force was calibrated for individual beads based on their thermal fluctuations under force, following a method described in a previous publication (119).

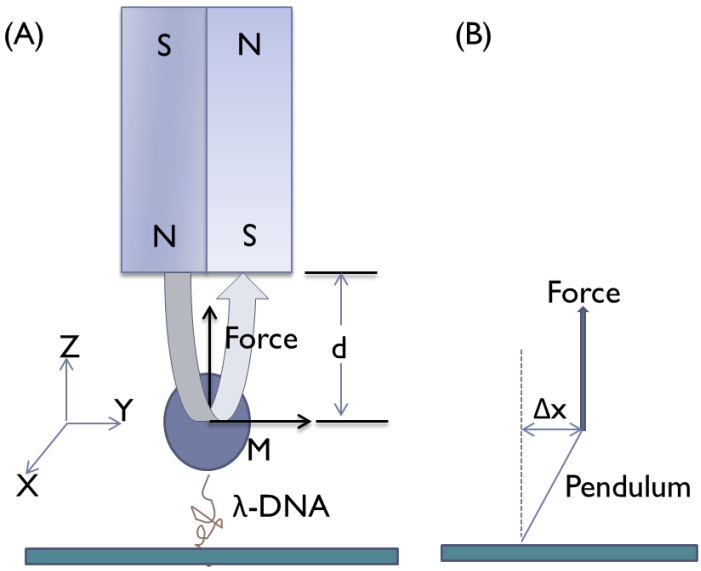

Figure 5.8: (A) Schematic figure of the magnetic tweezers setup (not to scale) and (B) Schematic figure of the effective pendulum.

A 48502 base-pair lambda DNA served as a linker between a magnetic bead and the glass substrate, as shown in fig. 5.8. The fluctuation of the bead on X direction perpendicular to the magnetic field is recorded. Under the magnetic field, the bead/DNA complex can be approximately regarded as a pendulum whose spring constant k is defined as $k=F/L$, where F is the applied force and L is the "effective" length of the spring which equals the sum of the DNA length and the radius of the bead. According to equipartition theorem, the thermal fluctuation on one degree of freedom should have equal energy to $0.5k_bT$.

$$\frac{1}{2}k_bT = \frac{1}{2}k < \Delta x >^2 = \frac{1}{2}\frac{F}{L} < \Delta x >^2 \tag{5.2}$$

$<\Delta x>^2$ is the averaged X-direction fluctuation over time which can be directly measured by recording the position of the bead around a fixed point on the glass. Thus, the stretching force can be obtained by the equation,

$$F = \frac{k_bTL}{< \Delta x >^2} \tag{5.3}$$

It is verified that the magnetic force F and the distance d between the magnet and the bead should follow an exponential equation,

$$\log F = kd + c \tag{5.4}$$

Where k is the coefficients determined by the intrinsic characters of the beads while c is the intercepts which can denote the heterogeneous of different beads. Force calibration results indicate that for our experiment beads (M270 strepav-idin, Dynabeads), the difference is relatively small (<5%).

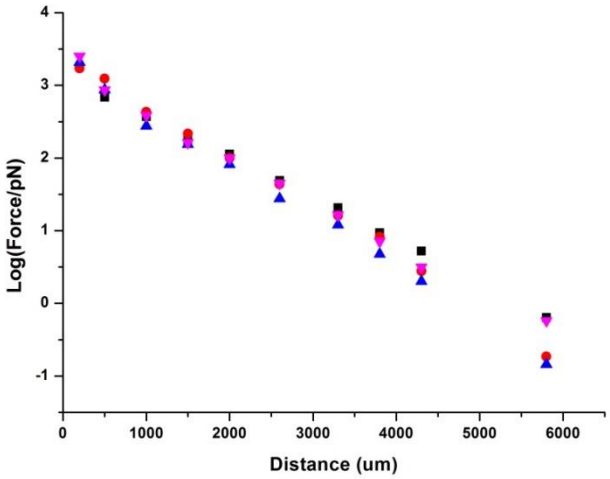

Figure 5.9: Curves of force versus distance in the force calibration. Points with different colors represent the results from different beads. The slopes of the curves are similar while the intercept differs, which can denote the beads heterogeneity.

In magnetic tweezers, in assistance with other coupled techniques, the beads position can be determined. In XY plane, the beads can be directly recorded with a CCD camera. In the Z plane, the beads position failed to obtain directly. However, TIRFm can help solving this problem. The principle for TIRFm is also shown here. When an incident light had an incident angle greater than the critical angle, the total internal reflection would be developed, also creating an evanescent wave adjacent to the interface of the glass and specimen. This evanescent wave was used to activate the fluorescent beads or fluorophores. The evanescent wave had a maximum depth of several hundred of nanometers and its density dropped off exponentially with a decay constant around 1/ (100 nm). Thus by measuring the intensity of the fluorescent bead or fluorophores, the height in the Z direction can be converted, with a spatial resolution along this direction of a few nanometers.

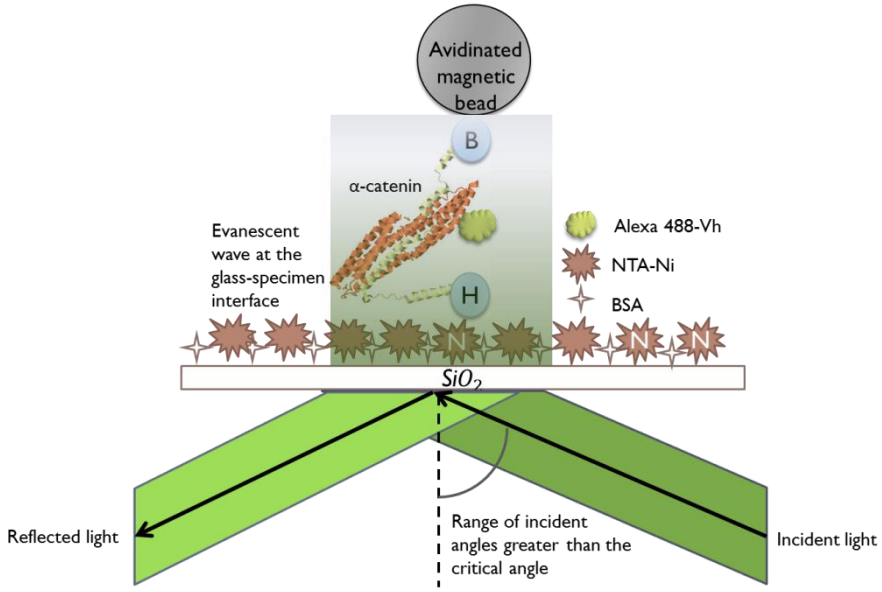

Figure 5.10: Schematic of the experimental setup of magnetic tweezer and the TIRFm system. The green color light is a 488 nm wavelength laser with a total power of nearly 0.2 W and the incident angles can be adjusted. The evanescent wave is shown in gradient change green and is used to excite the fluorescent bead.

As the height detection was realized through the TIRF, before every measurement, calibration of the TIRF depth should be performed at first. As mentioned, the strength of the evanescent wave field decayed exponentially from the interface to the specimen following the equation of:

$$E(z) = E_0 \exp(-\frac{z}{d}) \tag{5.5}$$

Where *E(z)* is the field strength at the height of *z* from the interface, E_0 is the field strength at the interface, *d* is the TIRF depth. When a fluorescent bead entered the region of the evanescent wave, it will be activated and emit fluorescence, with its intensity proportional to the strength of the evanescent field,

$$\frac{I(z_1)}{I(z_2)} = \frac{E(z_1)}{E(z_2)} = \exp(-\frac{z_1 - z_2}{d}) \tag{5.6}$$

Where $I(z_1)$ and $I(z_2)$ are the fluorescence intensity of a bead at the height of z_1 and z_2, respectively. According to this equation, the height position change of the bead can be converted from the measured intensity difference at different height.

$$\Delta z = z_1 - z_2 = -d \times \ln \frac{I(z_1)}{I(z_2)} \tag{5.7}$$

The main purpose of the TIRF calibration is to determine the TIRF depth *d*. This value was determined by measuring and fitting the intensity-distance curve. In fact, due to the mechanical drift of our homemade system, the TIRF calibration was performed monthly, with a depth ranged from 180 to 220 nm.

5.2.4 Criterion of deciding the binding

Generally speaking, the binding between proteins is hard for direct observation. In our experiments, the binding between force-stretched α-catenin and vinculin was observed in an indirect way.

Alexa Fluor 488 dye is a bright, green-fluorescent dye with excitation ideally suited to the 488 nm lasers. It can be attached to proteins through some specific bindings. In our experiments, labelling and purification of the vinculin head Vd with Alexa Fluor 488 dye were realized by a commercial microscale protein labelling kit (A30006) following the manufacture's protocol. After the α-catenin was immobilized in the magnetic tweezer chamber, a solution containing the Alexa 488 dye labelled Vd was added into it. An incubation time of one hour which was sufficient for the interaction between the α-catenin and vinculin was waited in two different manners, (a) no force applied

on the beads; (b) an average 20pN force was applied on the beads (20pN force is large enough to trigger the protein partial unfolding). When incubation was over, the unbound Vd was flushed away with a 1ml of 1 X PBS. The washing speed was controlled by a syringe pump, ensuring the flow dragging force not exceed 1pN.

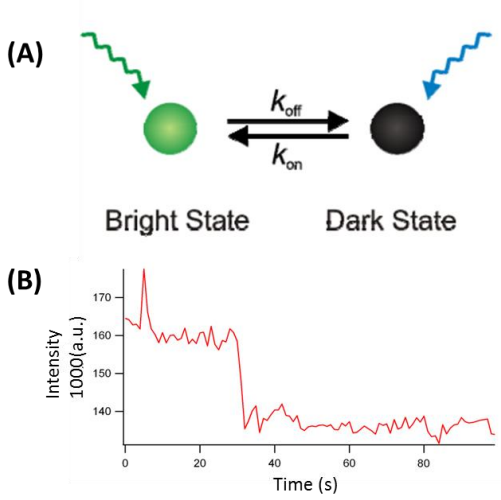

Figure 5.11: (A) Fluorophores can be activated by a specific wavelength laser and emit fluorescence, however, after a long exposure to high power laser, the fluorophores would photo-bleach. (B) Intensity versus time of an example of Alexa 488 fluorophore measured during the experiment, the abruptly decrease in intensity indicates the photo-bleach of the fluorophore. Once bleached, the fluorescence would disappear forever.

The criterion of deciding a binding between α-catenin and vinculin is to count the photobleaching events. The Alexa 488 dye, under exposure to 488 nm laser with a relatively large power or the exposure time is long enough, will had a suddenly decrease in the fluorescent intensity, this phenomenon is the so-called photobleaching. Generally speaking, photobleaching is a non-reversible process. Once happened, the dark state of such fluorophore can never be switched on. If the Alexa 488 labelled Vd was associating with the α-catenin, then it will be exposed to the evanescent wave and thus emit fluorescence. We recorded the fluorescence over time to measure whether there is

any abruptly decrease in its intensity. Each photobleaching event represents a binding between the α-catenin and vinculin. In this way, the binding events between α-catenin and vinculin can be measured. Moreover, we can quantitatively determine the number of the binding in each α-catenin.

5.3 Results

5.3.1 Characteristic unfolding of α-catenin

In our experiments, both AFM and magnetic tweezers are used to unfold α-catenin and the results indicated that the characteristic unfolding shares some similarities.

In AFM experiments, the constant velocity mode was used with the velocity ranging from 100 to 3600 nm/s. For each velocity, 40 to 80 valid force-extension curves can be obtained. The data in Fig. 5.12 suggested that α-catenin is a relatively "rigid" protein, whose unfolding peak mainly located at a large force of f=60 pN. When the constant velocity was low (v=100 nm/s), only one unfolding of α-catenin was induced by the external force, with a contour length increase of 10 nm. As the pulling velocity increased, we can observe more characteristic unfolding with the contour length increase such as ΔL~10, 20 and 40 nm. Moreover, the peak of the contour length increase shifted from 10nm to larger values, this phenomenon was very obvious for higher velocity experiments. All these data indicated that the unfolding of α-catenin was not a one step process. In contrast, the α-catenin was a multiple-domain protein whose bonds breaking should not happen simultaneously. As

the contour length increases were regularly spaced with a difference of ΔL~10 nm, we can assume that the minimum partial unfolding step of α-catenin was about 10 nm.

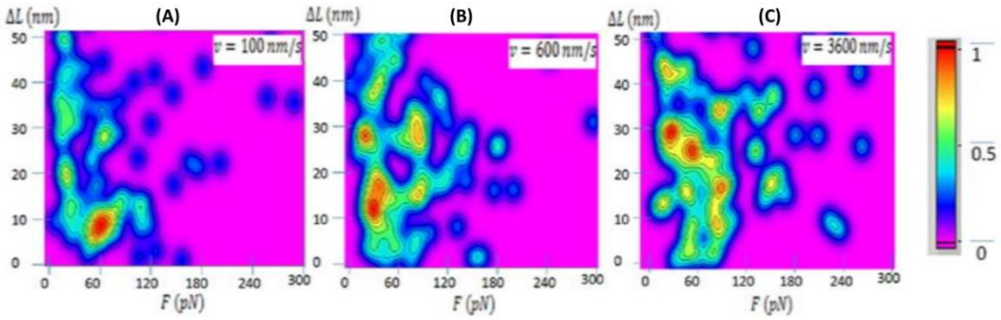

Figure 5.12: 3D images indicating the frequency of the unfolding events at different external force f and with different contour length change *ΔL*. (A), (B) and (C) represents the result of all experiment data with a constant velocity of *v=100 nm/s*, *v=600 nm/s* and *v=3600 nm/s*, respectively. The color denotes the normalized frequency of the events, where the more red color represents a higher frequency. (A) Only one red peak at *ΔL~10* nm is observed. (B) There are two major red peak located at *ΔL~10* and *ΔL~30 nm*.(C) There are three red peak located at *ΔL~10, 30 and 40*, respectively.

This assumption is further verified after we took all the ΔL values of all experiments into one histogram to compare their frequencies. As fig. 5.13 showed, only one single peak of ΔL~10 nm was observed, with a large half width of near 40 nm.

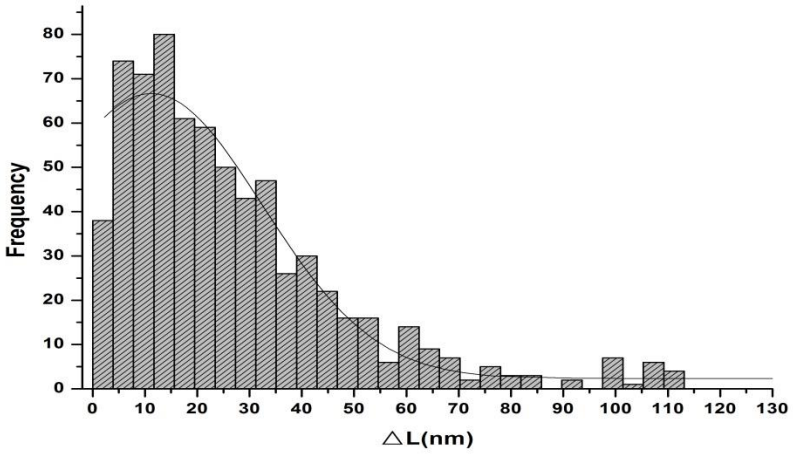

Figure 5.13: AFM data of the distribution of contour length changes. All experiment data (600 curves, 1100 data points) are plotted.

As for the magnetic tweezer experiments, where the magnet position was precisely controlled by a MP285 micro manipulator, thus, a constant loading force mode was applied to unfold the proteins. Considering that the magnet was not strong enough, the maximum force created during the whole experiments was less than 30 pN, which is smaller than AFM. In our experiments, the α-catenin was stretched at different constant force ranging from 0-10 pN. Besides, as magnetic tweezer is a low-yielding technique, we had obtained less results of magnetic tweezer compared with AFM. Totally, we obtained 50 effective curves indicating the unfolding of a-catenin, with 4 to 6 unfolding events per curve.

In fig.5.14, we also plot all contour length increase in one histogram to study the distribution of the contour length increase. Similar as AFM, the contour length change is also converted from the extensions. The result of magnetic tweezer is highly consistent with the results of AFM. Only a single peak located at $\Delta L \sim 10\ nm$ can be found, with a half width of 20 *nm*.

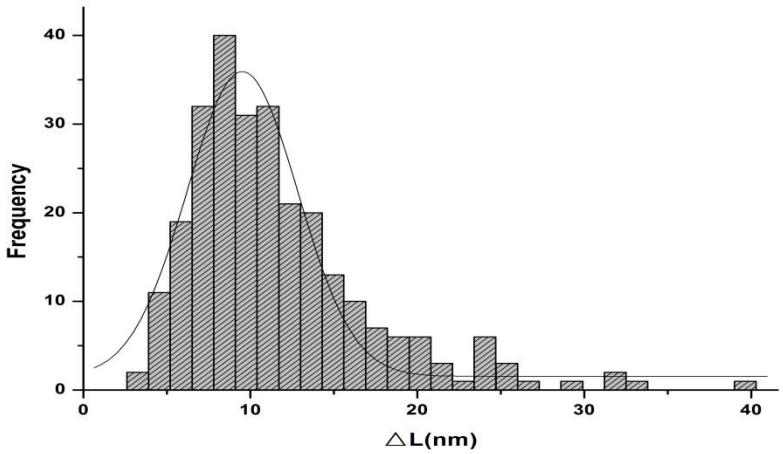

Figure 5.14: Magnetic tweezer data of the distribution of contour length changes. 50 curves are plotted. Each curve contains an average of *4-6* unfolding events.

The partial unfolding of α-catenin was measured by AFM and magnetic tweezer, their results are consistent. (1).A characteristic unfolding with step size of nearly 10 nanometers is observed by both methods; (2).Degree of the partial unfolding is determined by the value of external force, larger external force can stretch α-catenin to longer extensions; (3) 10pN force is large enough to trigger the characteristic 10 nm unfolding, other characteristic unfolding requires larger force. As each unfolding is associated with an opening of a α-helix bundle, our results indicate that the different bundles in a-catenin differ in their stiffness. The softest bundle will open under 10pN force;

5.3.2 Force triggers the binding between α-catenin and vinculin

The result that α-catenin can be partially unfolded under nearly 10pN force revealed a fact that the conformation of α-catenin can be changed. To test the hypothesis the force induced α-catenin conformation change can expose the cryptic binding sites for vinculin, we studied the binding between α-catenin/α-

catenin mutants and the Alexa 488 labelled vinculin head (488-Vh), in presence and absence of force, respectively. To do so, we recorded the TIRF fluorescence images at 488nm for one minute using an Olympus IX71 microscope coupled with a 1.45 numerical aperture, x 100 Objective. Images were further analyzed using an in-house Igor program. We measured the total intensity over time of auto-fluorescent beads which had linked with a single α-catenin. The criterion for deciding whether the bead bound to a single αC was to observe the random motion of the bead around a single point close to the surface. If there was no protein attached, the bead would quickly disappear away from the ROI or just ill-focused. If the bead was attached with more than one tether or unknown tethers, the bead would either undergo an extra rotation or the random motion would be apparently different. Though the fluorescent beads in our experiment had intrinsic decay in the fluorescence intensity, such decay can be neglected by normalization. As the right panel (A) showed, the normalized fluorescence intensity remained nearly constant during the whole experiments time. In (B), an abruptly intensity decrease was observed, which indicated there was one 488-Vh bound to the stretched αC. In (C), three regularly spaced photobleaching steps were observed, with a nearly same intensity drop of 6000 a.u. , which indicated there were three 488-Vh bound to the stretched protein.

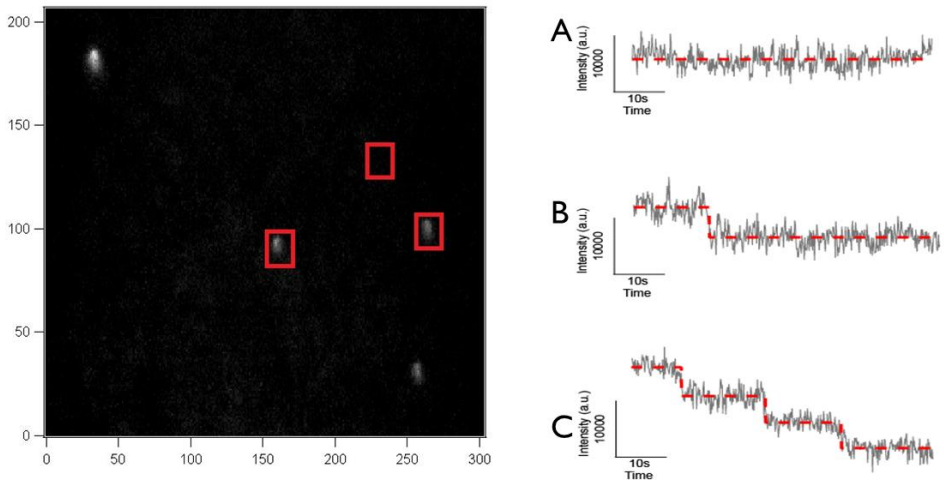

Figure 5.15: Left panel: Example of a TIRF image of a working field showing the auto-fluorescent beads attached on the glass surface. The equally sized red squares represent the Region of Interest (ROI) which will be analyzed to measure the intensity change over time. Right panel (A), (B) and (C): Three representative curve of intensity over time of the normalized fluorescence intensity with zero, one and three photobleaching events, respectively. Dashed lines are drawn for visual guidance.

WT α-catenin:

In the beginning, the interaction between WT α-catenin and vinculin was studied in two different ways, one way is that there was no force applied on the WT αC, the other way is an average 20 pN force was applied. The reason why we set the average force as 20 pN is due to two reasons. One is that it is already verified that 10 pN force is sufficient to trigger the WT αC unfolding so we do not need higher forces. Another reason is that the calculated value of 20 pN is only accurate for the force exerted on the bead right below the magnet. However, the real force exerted on other beads away from the center would be smaller. In other words, the 20 pN is an average force.

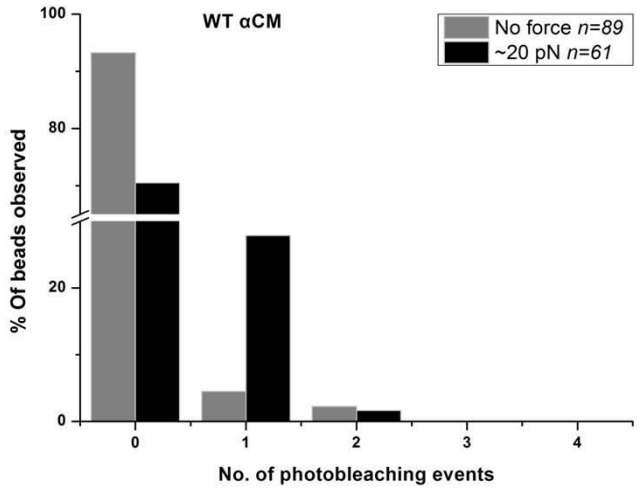

Figure 5.16: Histograms of the percentage of beads with different numbers of photobleaching events observed for WT α-catenin

We counted the numbers of photobleaching events to verify the binding between WT αC and 488-Vh. The probability of photobleaching events was very low when no force applied on the WT α-catenin. As the force increased from zero to 20 pN, the probability for one photobleaching event increased nearly an order of magnitude greater, from 3% to 29%. Significantly, most tethers showed only one photobleaching event at 20 pN force compared with that at 0 pN force. This result is consistent with previous reports suggesting there is only one vinculin-binding α-helix per α-catenin central domain (99).

Dmod α-catenin:

We performed similar experiments with α-catenin mutants as the control experiments. The Dmod mutant kept the whole VBD while most part of the modulation domain had been cut off. Compared with the result for WT α-catenin, the probability for the number of photobleaching events did not show significant differences in

presence or absence of force. For this mutant, even in lack of force stretching, 25% of the tethers were still able to bind to vinculin, which was nearly the same as 20 pN force applied on them. This indicated that Dmod α-catenin was not sensitive to external force. In other word, it is the modulation domain that acting as the mechanosensor, it can sense and then react to the external force, maybe in a manner of changing its conformation: when there is no force or little force, the modulation domain prevented the binding between WT α-catenin and vinculin by adopting a closed conformation to block the VBD. However, the external force can unfurl the cryptic VBD and thus the binding between α-catenin and vinculin can be activated.

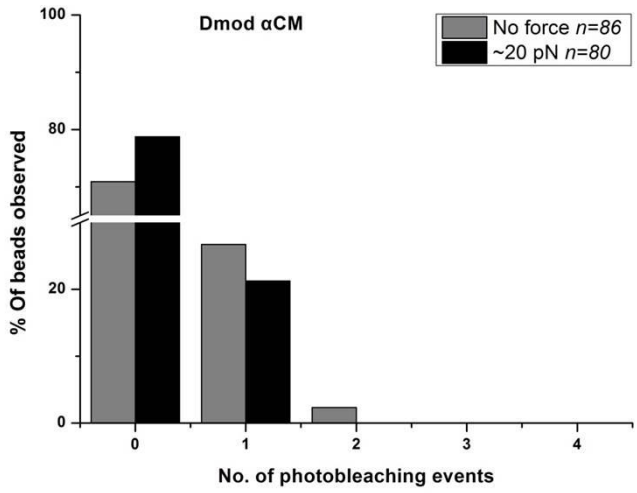

Figure 5.17: Histograms of the percentage of beads with different numbers of photobleaching events observed for Dmod α-catenin.

Trimer α-catenin:

As for the positive control, trimer α-catenin which contains three repeats of the WT α-catenin was also tested to verify the number of vinculin binding domain.

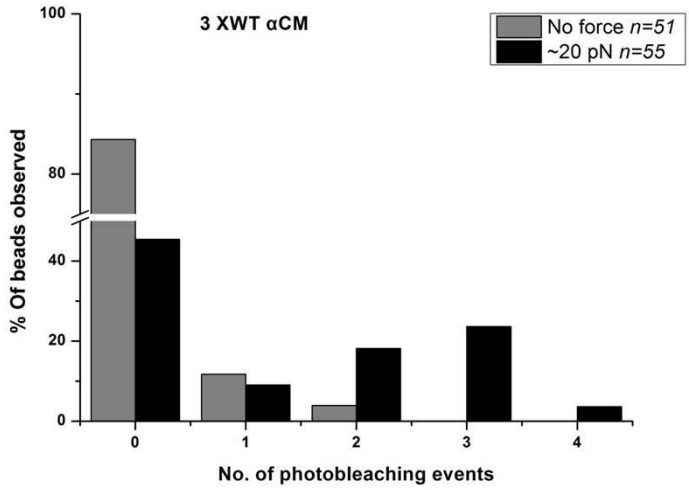

Figure 5.18: Histograms of the percentage of beads with different numbers of photobleaching events observed for trimer α-catenin.

With highly consistency, this artificial trimer α-catenin showed that it contained three potential vinculin-binding sites. Besides, we also observed an increase of the photobleaching events when forces were increased from 0 to 20 pN, with the most probable number of photobleaching events reaching three at 20 pN.

To be stressed, for the rare cases where we observed more than one photobleaching event on WT α-catenin and Dmod α-catenin, or more than three photobleaching events on trimer α-catenin, were likely due to low probability of double or even multiple coupling of the Alexa 488 dyes on some vinculin head molecules. In all experiments, the majority of the tethers showed no photobleaching events and this could be due to several reasons. One is that not all the tethers were our targeted a-catenin. Though we used specific binding assays to link the a-catenin to magnetic beads, the beads were still captured by other proteins (most likely BSA, which had been used for blocking and were

very sticky in the experiments environment) which definitely could not bind to vinculin. Another possible reason is that the binding time for vinculin and catenin were set as one hour. For such a long time period, the disassociation probability should not be ignored.

5.4 Discussion & Conclusion

In chapter 5, we report on the mechanical response of α-catenin and the force-induced binding to vinculin, characterized at the single molecule level, within a physiological relevant force.

Characteristic unfolding of α-catenin has been revealed in AFM and magnetic tweezer experiments. It is verified that when the α-catenin sense the external force, it can be partially unfolded. The minimal unfolding step size is nearly 10 nanometers and such unfolding can be triggered by force not exceeding 10 pN. Taking the binding experiments into consideration, it is most likely that this unfolding is the open of the α-helix bundle located at the modulation domain. In addition, it has been convinced that it is the modulation domain which inhibits the binding between catenin and vinculin. However, force-induced a-catenin unfolding can unfurl the binding site, thus, the binding between α-catenin and vinculin can be activated in a force-dependent manner.

To conclude, a mechanosensing mechanism centered on a-catenin in cell-cell adhesion is presented in our study. When there is no force (or very little force) acting on the cell-cell adhesion, the a-catenin is in its folded conformation. In this baseline condition, there is only one F-actin binding to the C terminus of

a-catenin, in an unknown way, to give some minimal support to the structural integrity. If an adjacent cell tugs too hard on the cell-cell adhesion (in particularly, through cadherin-cadherin binding on one end, and actin-myosin pulling on the other end), the baseline F-actin force will not be sufficient to sustain this additional force and is prone to breaking. The a-catenin senses this mechanical load and then transduces it into biochemical signals, which triggers the conformation switch from closed to open and expose the cryptic binding sites for vinculin. The ability of binding vinculin is thus activated. Meanwhile, the vinculin head binding to a-catenin in turn activate the vinculin tail binding to F-actin. In this way, more F-actin filaments are recruited to this forced site and allow the cell-cell adhesion to respond to the large force.

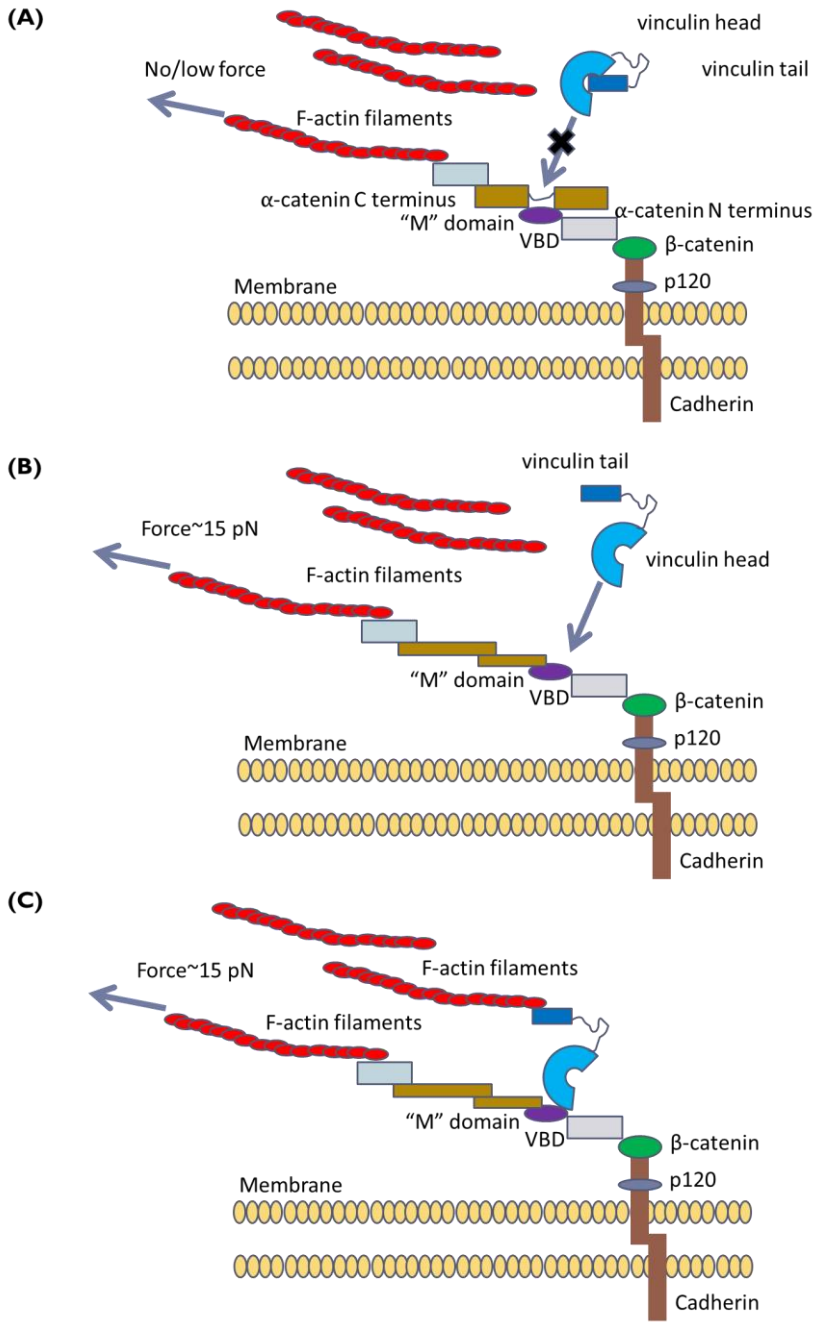

Figure 5.19: Schematic of a mechanosensing mechanism in cell-cell adhesion. (A). When there is no force or low force applied on a-catenin, it adopts a closed conformation to prevent the accessibility for vinculin to a-catenin. (B). When dragging force from adjacent cadherin or F-actin filaments is large enough, a-catenin fails to maintain its original auto-inhibited conformation. The exposure of the vinculin binding site activates the binding between a-catenin and vinculin. (C). Vinculin binding to a-catenin also changes the closed conformation for vinculin, making the vinculin tail bound to F-actin possible. In this way, more F-actin filaments are recruited to the forced site and allow the cells to respond to the additional force.

This mechanosensing and transduction process centered on a-catenin/vinculin revealed a similar mechanism as the talin/vinculin. Further studies will be needed to determine whether the pathway of a-catenin recruiting vinculin is unique or α-catenin in its open conformation can cooperate with many other actin binding partners to help to regulate the strength of the linkage between the cytoskeletons and the cadherin complex at cell-cell adhesions. Together with previous studies of the force-dependent binding of vinculin to talin, which happened at the intergrin-mediated cell-matrix adhesion, this tension-dependent unfurling of mechanosensitive proteins (there are diversity of mechanosensitive proteins) and recruitment of binding adaptor proteins maybe a more general mechanism for mechanosensing and mechanotransduction at a variety of adhesion sites (not only cell-cell adhesion and cell-matrix adhesion).

In addition, the single molecule manipulation method used in our experiment may shed light to further studies of other force-dependent protein-protein interactions, which may have important implication in many biological processes.

CHAPTER 6

Conclusions

This thesis is divided into two main parts, one is the study of the interactions between like-charge colloidal particles under alternating electric field, the other is to prove a mechanosensing mechanism centered on a-catenin in cell-cell adhesions.

In chapter 3 we used an alternating electric field to manipulate the behavior of colloidal spheres and found a novel and steady method for patterned colloidal assembly based on AEF. This method displayed great advantages than traditional assays and should be a general method which would also be available for other colloids.

In chapter 4, we observed an anomalous long-range attraction between like-charge colloidal spheres under AEF and further determined the effective force range to be as long as 1d to 3d. We compared the experimental results with theoretical prediction and ruled out the probability that this attraction arouse from van der Waals, dipole-dipole interaction or EHD flow induced Stokes force. By studying the pair potential on condition of different associating parameters, we found that the attraction was proportional to electric field, electric frequency and sphere diameters. Many-body effect in our system would contribute to pair potential, but such correlation would not be significant unless the density exceeding a critical value. In addition, we convinced

the confinement and external field are needed to yield attractions between spheres. Finally we proposed a mechanism illustrating the origin of this attraction. It is most likely that the attraction is the result of the redistribution of the counterions in the sphere electric double layer. We compared the simulation results based on this mechanism and found it agreed well with the experimental data. This mechanism gives insight to a full understanding about the like-charge interactions.

In chapter 5, we used single molecule technologies to study the mechanosensing mechanism centered on a-catenin. We studied the characteristic unfolding of a-catenin and measured the binding to vinculin in presence and absence of force. We confirmed the hypothesis that a-catenin changes its conformation upon application of force and modulate its binding affinity to vinculin by unfurling its cryptic vinculin binding sites. We discussed the biological importance of this finding and proposed that this mechanism may be a general mechanism which remains to prove in the future. In addition, the single molecule manipulation we used in this chapter may open up possibilities to study other protein-protein interactions in general.

References

1. Asakura S, Oosawa F. INTERACTION BETWEEN PARTICLES SUSPENDED IN SOLUTIONS OF MACROMOLECULES. Journal of Polymer Science. 1958;33(126):183-92.

2. Guastall.J. SHAW,DJ - INTRODUCTION TO COLLOID AND SURFACE CHEMISTRY. Bull Soc Chim Fr. 1967(9):3574-8.

3. Derjaguin B, Landau L. THEORY OF THE STABILITY OF STRONGLY CHARGED LYOPHOBIC SOLS AND OF THE ADHESION OF STRONGLY CHARGED-PARTICLES IN SOLUTIONS OF ELECTROLYTES. Prog Surf Sci. 1993;43(1-4):30-59.

4. Verwey EJW, Overbeek JTG. Theory of the stability of lyophobic colloids: Courier Corporation; 1999.

5. Borwankar AU, Dinin AK, Laber JR, Twu A, Wilson BK, Maynard JA, et al. Tunable equilibrium nanocluster dispersions at high protein concentrations. Soft Matter. 2013;9(6):1766-71.

6. Gee ML, Israelachvili JN. Interactions of surfactant monolayers across hydrocarbon liquids. J Chem Soc, Faraday Trans. 1990;86(24):4049-58.

7. Israelachvili JN. Intermolecular and surface forces: revised third edition: Academic press; 2011.

8. Li Y, Tao N, Pan J, Garcia A, Lindsay S. Direct measurement of interaction forces between colloidal particles using the scanning force microscope. Langmuir. 1993;9(3):637-41.

9. Ito K, Yoshida H, Ise N. Void structure in colloidal dispersions. Science-AAAS-Weekly Paper Edition-including Guide to Scientific Information. 1994;263(5143):66-7.

10. Dosho S, Ise N, Ito K, Iwai S, Kitano H, Matsuoka H, et al. Recent study of polymer latex dispersions. Langmuir. 1993;9(2):394-411.

11. Tata B, Rajalakshmi M, Arora AK. Vapor-liquid condensation in charged colloidal suspensions. Physical review letters. 1992;69(26):3778.

12. Derjaguin B. Theory of the stability of strongly charged lyophobic sols and the adhesion of strongly charged particles in solutions of electrolytes. Acta Physicochim USSR. 1941;14:633-62.

13. Bowen WR, Sharif AO. Long-range electrostatic attraction between like-charge spheres in a charged pore. Nature. 1998;393(6686):663-5.

14. Crocker JC, Grier DG. Methods of digital video microscopy for colloidal studies. Journal of colloid and interface science. 1996;179(1):298-

310.

15. Grier DG. Optical tweezers in colloid and interface science. Current opinion in colloid & interface science. 1997;2(3):264-70.

16. Larsen AE, Grier DG. Like-charge attractions in metastable colloidal crystallites. Nature. 1997;385(6613):230-3.

17. Ise N, Okubo T, Sugimura M, Ito K, Nolte H. Ordered structure in dilute solutions of highly charged polymer lattices as studied by microscopy. I. Interparticle distance as a function of latex concentration. The Journal of chemical physics. 1983;78(1):536-40.

18. Crocker JC, Grier DG. Microscopic measurement of the pair interaction potential of charge-stabilized colloid. Physical review letters. 1994;73(2):352.

19. Kepler GM, Fraden S. Attractive potential between confined colloids at low ionic strength. Physical review letters. 1994;73(2):356.

20. Carbajal-Tinoco MD, Castro-Román F, Arauz-Lara JL. Static properties of confined colloidal suspensions. Physical Review E. 1996;53(4):3745.

21. Crocker JC, Grier DG. When like charges attract: the effects of geometrical confinement on long-range colloidal interactions. Physical review letters. 1996;77(9):1897.

22. Pusey P, Van Megen W. Phase behaviour of concentrated suspensions of nearly hard colloidal spheres. Nature. 1986;320(6060):340-2.

23. Gasser U, Weeks ER, Schofield A, Pusey P, Weitz D. Real-space imaging of nucleation and growth in colloidal crystallization. Science. 2001;292(5515):258-62.

24. Zhang TH, Liu XY. Nucleation: what happens at the initial stage? Angewandte Chemie International Edition. 2009;48(7):1308-12.

25. Zhang TH, Liu XY. How does a transient amorphous precursor template crystallization. Journal of the American Chemical Society. 2007;129(44):13520-6.

26. Gasser U. Crystallization in three-and two-dimensional colloidal suspensions. Journal of Physics: Condensed Matter. 2009;21(20):203101.

27. Hunter GL, Weeks ER. The physics of the colloidal glass transition. Reports on Progress in Physics. 2012;75(6):066501.

28. Zhang Z, Yunker PJ, Habdas P, Yodh A. Cooperative rearrangement regions and dynamical heterogeneities in colloidal glasses with attractive versus repulsive interactions. Physical review letters. 2011;107(20):208303.

29. Pham KN, Puertas AM, Bergenholtz J, Egelhaaf SU, Moussaıd A, Pusey PN, et al. Multiple glassy states in a simple model system. Science. 2002;296(5565):104-6.

30. Peng Y, Wang Z, Alsayed AM, Yodh AG, Han Y. Melting of colloidal crystal films. Physical review letters. 2010;104(20):205703.

31. Zhang K-Q, Liu XY. Two scenarios for colloidal phase transitions. Physical review letters. 2006;96(10):105701.

32. Asher SA, Holtz J, Weissman J, Pan G. Mesoscopically periodic photonic-crystal materials for linear and nonlinear optics and chemical sensing. Mrs Bulletin. 1998;23(10):44-50.

33. Velev OD, Bhatt KH. On-chip micromanipulation and assembly of colloidal particles by electric fields. Soft Matter. 2006;2(9):738-50.

34. Sunkara HB, Jethmalani JM, Ford WT. Composite of colloidal crystals of silica in poly (methyl methacrylate). Chemistry of materials. 1994;6(4):362-4.

35. Joannopoulos J, Villeneuve PR, Fan S. Photonic crystals. Solid State Communications. 1997;102(2):165-73.

36. Xia Y, Gates B, Yin Y, Lu Y. Monodispersed colloidal spheres: old materials with new applications. Advanced Materials. 2000;12(10):693-713.

37. Denkov N, Velev O, Kralchevski P, Ivanov I, Yoshimura H, Nagayama K. Mechanism of formation of two-dimensional crystals from latex particles on substrates. Langmuir. 1992;8(12):3183-90.

38. Yang SM, Jang SG, Choi DG, Kim S, Yu HK. Nanomachining by colloidal lithography. Small. 2006;2(4):458-75.

39. Aizenberg J, Braun PV, Wiltzius P. Patterned colloidal deposition controlled by electrostatic and capillary forces. Physical review letters. 2000;84(13):2997.

40. Fan F, Stebe KJ. Assembly of colloidal particles by evaporation on surfaces with patterned hydrophobicity. Langmuir. 2004;20(8):3062-7.

41. Zheng H, Lee I, Rubner MF, Hammond PT. Two component particle arrays on patterned polyelectrolyte multilayer templates. Advanced Materials. 2002;14(8):569.

42. Koo HY, Yi DK, Yoo SJ, Kim D-Y. A snowman-like array of colloidal dimers for antireflecting surfaces. Advanced Materials. 2004;16(3):274-7.

43. Adamczyk Z, Zembala M, Siwek B, Warszyński P. Structure and ordering in localized adsorption of particles. Journal of colloid and interface science. 1990;140(1):123-37.

44. Xia Y, Yin Y, Lu Y, McLellan J. Template-assisted self-assembly of spherical colloids into complex and controllable structures. Advanced Functional Materials. 2003;13(12):907-18.

45. Li F, Josephson DP, Stein A. Colloidal assembly: the road from particles to colloidal molecules and crystals. Angewandte Chemie International Edition. 2011;50(2):360-88.

46. Yethiraj A. Tunable colloids: control of colloidal phase transitions with tunable interactions. Soft Matter. 2007;3(9):1099-115.

47. Böhmer M. In situ observation of 2-dimensional clustering during electrophoretic deposition. Langmuir. 1996;12(24):5747-50.

48. Trau M, Saville D, Aksay I. Field-induced layering of colloidal crystals. Science. 1996;272(5262):706-9.

49. Juárez JJ, Mathai PP, Liddle JA, Bevan MA. Multiple electrokinetic actuators for feedback control of colloidal crystal size. Lab on a Chip. 2012;12(20):4063-70.

50. Smallenburg F, Vutukuri HR, Imhof A, Van Blaaderen A, Dijkstra M. Self-assembly of colloidal particles into strings in a homogeneous external electric or magnetic field. Journal of Physics: Condensed Matter. 2012;24(46):464113.

51. Yethiraj A, van Blaaderen A. A colloidal model system with an interaction tunable from hard sphere to soft and dipolar. Nature. 2003;421(6922):513-7.

52. Zhang K-Q, Liu XY. In situ observation of colloidal monolayer nucleation driven by an alternating electric field. Nature. 2004;429(6993):739-43.

53. Vutukuri HR, Demirörs AF, Peng B, van Oostrum PD, Imhof A, van Blaaderen A. Colloidal analogues of charged and uncharged polymer chains with tunable stiffness. Angewandte Chemie. 2012;124(45):11411-5.

54. Hu Y, Glass J, Griffith A, Fraden S. Observation and simulation of electrohydrodynamic instabilities in aqueous colloidal suspensions. The Journal of chemical physics. 1994;100(6):4674-82.

55. Isambert H, Ajdari A, Viovy J-L, Prost J. Electrohydrodynamic patterns in charged colloidal solutions. Physical review letters. 1997;78(5):971.

56. Grier DG. Fluid dynamics: vortex rings in a constant electric field. Nature. 2003;424(6946):267-8.

57. Ristenpart W, Aksay I, Saville D. Electrically guided assembly of planar superlattices in binary colloidal suspensions. Physical review letters. 2003;90(12):128303.

58. Yeh S-R, Seul M, Shraiman BI. Assembly of ordered colloidal aggregrates by electric-field-induced fluid flow. 1997.

59. Prieve DC. Measurement of colloidal forces with TIRM. Advances in Colloid and Interface Science. 1999;82(1):93-125.

60. Calderon FL, Stora T, Monval OM, Poulin P, Bibette J. Direct measurement of colloidal forces. Physical review letters. 1994;72(18):2959.

61. Li D, Lam CN, Biswal SL. Measuring short-range repulsive forces by imaging directed magnetic-particle assembly title. Soft Matter. 2010;6(2):239-42.

62. Sainis SK, Germain V, Dufresne ER. Statistics of particle trajectories at short time intervals reveal fN-scale colloidal forces. Physical review letters. 2007;99(1):018303.

63. Kegler K, Salomo M, Kremer F. Forces of interaction between DNA-grafted colloids: an optical tweezer measurement. Physical review letters. 2007;98(5):058304.

64. Roberts GS, Wood TA, Frith WJ, Bartlett P. Direct measurement of the effective charge in nonpolar suspensions by optical tracking of single particles. The Journal of chemical physics. 2007;126(19):194503.

65. El Masri D, van Oostrum P, Smallenburg F, Vissers T, Imhof A, Dijkstra M, et al. Measuring colloidal forces from particle position deviations inside an optical trap. Soft Matter. 2011;7(7):3462-6.

66. Mittal M, Lele PP, Kaler EW, Furst EM. Polarization and interactions of colloidal particles in ac electric fields. The Journal of chemical physics. 2008;129(6):064513.

67. Ducker WA, Senden TJ, Pashley RM. Direct measurement of colloidal forces using an atomic force microscope. 1991.

68. Trau M, Saville D, Aksay I. Assembly of colloidal crystals at electrode interfaces. Langmuir. 1997;13(24):6375-81.

69. Solomentsev Y, Böhmer M, Anderson JL. Particle clustering and pattern formation during electrophoretic deposition: a hydrodynamic model. Langmuir. 1997;13(23):6058-68.

70. Sides PJ. Electrohydrodynamic particle aggregation on an electrode driven by an alternating electric field normal to it. Langmuir. 2001;17(19):5791-800.

71. Ristenpart W, Aksay I, Saville D. Electrohydrodynamic flow around a colloidal particle near an electrode with an oscillating potential. Journal of Fluid Mechanics. 2007;575:83-109.

72. Ristenpart W, Aksay I, Saville D. Assembly of colloidal aggregates by

electrohydrodynamic flow: Kinetic experiments and scaling analysis. Physical Review E. 2004;69(2):021405.

73. Greenwood R, Kendall K. Selection of suitable dispersants for aqueous suspensions of zirconia and titania powders using acoustophoresis. Journal of the European Ceramic Society. 1999;19(4):479-88.

74. O'Brien RW, Midmore BR, Lamb A, Hunter RJ. Electroacoustic studies of moderately concentrated colloidal suspensions. 1990.

75. Grier DG, Murray CA. The microscopic dynamics of freezing in supercooled colloidal fluids. The Journal of chemical physics. 1994;100(12):9088-95.

76. Bongers J, Manteufel H, Versmold H, Vondermaßen K. Microscopic measurements of correlation functions in colloid dispersions. The Journal of chemical physics. 1998;108(23):9937-45.

77. Xie R, Liu X-Y. Controllable epitaxial crystallization and reversible oriented patterning of two-dimensional colloidal crystals. Journal of the American Chemical Society. 2009;131(13):4976-82.

78. Gates B, Yin Y, Xia Y. A solution-phase approach to the synthesis of uniform nanowires of crystalline selenium with lateral dimensions in the range of 10-30 nm. Journal of the American Chemical Society. 2000;122(50):12582-3.

79. Kumacheva E, Garstecki P, Wu H, Whitesides GM. Two-dimensional colloid crystals obtained by coupling of flow and confinement. Physical review letters. 2003;91(12):128301.

80. Nadal F, Argoul F, Kestener P, Pouligny B, Ybert C, Ajdari A. Electrically induced flows in the vicinity of a dielectric stripe on a conducting plane. The European Physical Journal E. 2002;9(4):387-99.

81. Liu Y, Liu X-Y, Narayanan J. Kinetics and equilibrium distribution of colloidal assembly under an alternating electric field and correlation to degree of perfection of colloidal crystals. The Journal of Physical Chemistry C. 2007;111(2):995-8.

82. Zhang TH, Liu XY. Experimental modelling of single-particle dynamic processes in crystallization by controlled colloidal assembly. Chemical Society Reviews. 2014;43(7):2324-47.

83. Diao YY, Liu XY. Controlled colloidal assembly: Experimental modeling of general crystallization and biomimicking of structural color. Advanced Functional Materials. 2012;22(7):1354-75.

84. Kostic A, Lynch CD, Sheetz MP. Differential matrix rigidity response in breast cancer cell lines correlates with the tissue tropism. PLoS One. 2009;4(7):e6361.

85. Sawada Y, Tamada M, Dubin-Thaler BJ, Cherniavskaya O, Sakai R, Tanaka S, et al. Force sensing by mechanical extension of the Src family kinase substrate p130Cas. Cell. 2006;127(5):1015-26.

86. Dupont S, Morsut L, Aragona M, Enzo E, Giulitti S, Cordenonsi M, et al. Role of YAP/TAZ in mechanotransduction. Nature. 2011;474(7350):179-83.

87. Colombelli J, Besser A, Kress H, Reynaud EG, Girard P, Caussinus E, et al. Mechanosensing in actin stress fibers revealed by a close correlation between force and protein localization. Journal of cell science. 2009;122(10):1665-79.

88. Vogel V, Sheetz M. Local force and geometry sensing regulate cell functions. Nature reviews molecular cell biology. 2006;7(4):265-75.

89. Brasch J, Harrison OJ, Honig B, Shapiro L. Thinking outside the cell: how cadherins drive adhesion. Trends in cell biology. 2012;22(6):299-310.

90. Takeichi M. Morphogenetic roles of classic cadherins. Current opinion in cell biology. 1995;7(5):619-27.

91. Cowin P, Rowlands TM, Hatsell SJ. Cadherins and catenins in breast cancer. Current opinion in cell biology. 2005;17(5):499-508.

92. Jeanes A, Gottardi C, Yap A. Cadherins and cancer: how does cadherin dysfunction promote tumor progression&quest. Oncogene. 2008;27(55):6920-9.

93. El-Amraoui A, Petit C. Cadherins as targets for genetic diseases. Cold Spring Harbor perspectives in biology. 2010;2(1):a003095.

94. Kobielak A, Fuchs E. α-catenin: at the junction of intercellular adhesion and actin dynamics. Nature reviews Molecular cell biology. 2004;5(8):614-25.

95. Imamura Y, Itoh M, Maeno Y, Tsukita S, Nagafuchi A. Functional domains of α-catenin required for the strong state of cadherin-based cell adhesion. The Journal of cell biology. 1999;144(6):1311-22.

96. Itoh M, Nagafuchi A, Moroi S, Tsukita S. Involvement of ZO-1 in cadherin-based cell adhesion through its direct binding to α catenin and actin filaments. The Journal of cell biology. 1997;138(1):181-92.

97. Pokutta S, Drees F, Takai Y, Nelson WJ, Weis WI. Biochemical and structural definition of the l-afadin-and actin-binding sites of α-catenin. Journal of Biological Chemistry. 2002;277(21):18868-74.

98. Kobielak A, Pasolli HA, Fuchs E. Mammalian formin-1 participates in adherens junctions and polymerization of linear actin cables. Nature cell biology. 2004;6(1):21-30.

99. Weiss EE, Kroemker M, Rüdiger A-H, Jockusch BM, Rüdiger M. Vinculin is part of the cadherin–catenin junctional complex: complex formation between α-catenin and vinculin. The Journal of cell biology. 1998;141(3):755-64.

100. Peng X, Maiers JL, Choudhury D, Craig SW, DeMali KA. α-Catenin uses a novel mechanism to activate vinculin. Journal of Biological Chemistry. 2012;287(10):7728-37.

101. Bakolitsa C, Cohen DM, Bankston LA, Bobkov AA, Cadwell GW, Jennings L, et al. Structural basis for vinculin activation at sites of cell adhesion. Nature. 2004;430(6999):583-6.

102. Borgon RA, Vonrhein C, Bricogne G, Bois PR, Izard T. Crystal structure of human vinculin. Structure. 2004;12(7):1189-97.

103. Choi H-J, Pokutta S, Cadwell GW, Bobkov AA, Bankston LA, Liddington RC, et al. αE-catenin is an autoinhibited molecule that coactivates vinculin. Proceedings of the National Academy of Sciences. 2012;109(22):8576-81.

104. Rangarajan ES, Izard T. The cytoskeletal protein α-catenin unfurls upon binding to vinculin. Journal of Biological Chemistry. 2012;287(22):18492-9.

105. Yonemura S, Wada Y, Watanabe T, Nagafuchi A, Shibata M. α-Catenin as a tension transducer that induces adherens junction development. Nature cell biology. 2010;12(6):533-42.

106. Hutter JL, Bechhoefer J. Calibration of atomic‐force microscope tips. Review of Scientific Instruments. 1993;64(7):1868-73.

107. Marko JF, Siggia ED. Stretching dna. Macromolecules. 1995;28(26):8759-70.

109. Liu Y, Narayanan J, Liu X-Y. Colloidal phase transition driven by alternating electric field. The Journal of chemical physics. 2006;124(12):124906.

111. Katsumi A, Naoe T, Matsushita T, Kaibuchi K, Schwartz MA. Integrin activation and matrix binding mediate cellular responses to mechanical stretch. Journal of Biological Chemistry. 2005;280(17):16546-9.

112. Munevar S, Wang Y-l, Dembo M. Regulation of mechanical interactions between fibroblasts and the substratum by stretch-activated Ca2+ entry. Journal of cell science. 2004;117(1):85-92.

113. Thomas WE, Nilsson LM, Forero M, Sokurenko EV, Vogel V. Shear‐dependent ‘stick‐and‐roll’ adhesion of type 1 fimbriated Escherichia coli. Molecular microbiology. 2004;53(5):1545-57.

114. Thomas WE, Trintchina E, Forero M, Vogel V, Sokurenko EV. Bacterial adhesion to target cells enhanced by shear force. Cell. 2002;109(7):913-23.

115. Evans E, Leung A, Heinrich V, Zhu C. Mechanical switching and coupling between two dissociation pathways in a P-selectin adhesion bond. Proceedings of the National Academy of Sciences of the United States of America. 2004;101(31):11281-6.

116. Marshall BT, Long M, Piper JW, Yago T, McEver RP, Zhu C. Direct observation of catch bonds involving cell-adhesion molecules. Nature. 2003;423(6936):190-3.

117. Yago T, Wu J, Wey CD, Klopocki AG, Zhu C, McEver RP. Catch bonds govern adhesion through L-selectin at threshold shear. The Journal of cell biology. 2004;166(6):913-23.

118. del Rio A, Perez-Jimenez R, Liu R, Roca-Cusachs P, Fernandez JM, Sheetz MP. Stretching single talin rod molecules activates vinculin binding. Science. 2009;323(5914):638-41.

119. Chen H, Fu H, Zhu X, Cong P, Nakamura F, Yan J. Improved high-force magnetic tweezers for stretching and refolding of proteins and short DNA. Biophysical journal. 2011;100(2):517-23.

120. Fitzgerald R. Hydrodynamics may explain like-charge colloidal attraction. Physics Today. 2001;54(2):18-20.

121. Morthomas J, Würger A. Hydrodynamic attraction of immobile particles due to interfacial forces. Physical Review E. 2010;81(5):051405